

© Copyright by Ming Zhang, 2003

THERMAL PROPERTIES OF INDIUM NANOPARTICLES AND GOLD SILICIDE
FORMATION BY SCANNING NANOCALORIMETRY

BY

MING ZHANG

B. Engr., Tsinghua University, 1996

M. Engr., Tsinghua University, 1998

DISSERTATION

Submitted in partial fulfillment of the requirements
for the degree of Doctor of Philosophy in Materials Science and Engineering
in the Graduate College of the
University of Illinois at Urbana-Champaign, 2003

Urbana, Illinois

THERMAL PROPERTIES OF INDIUM NANOPARTICLES AND GOLD SILICIDE FORMATION BY SCANNING NANOCALORIMETRY

Ming Zhang

Department of Material Science and Engineering
University of Illinois at Urbana-Champaign, 2003

Leslie H. Allen, Adviser

ABSTRACT

This thesis is an experimental work on the thermal properties of indium nanoparticles and the interaction characteristics between gold and silicon using nanocalorimetry technique.

The melting behaviors of indium thin films have been investigated. The films consist of ensembles of nanoparticles whose melting temperatures are size-dependent. We experimentally determine the relationship between a nanoparticle's radius and its melting point by combining the caloric results with nanoparticle size distributions from TEM. The results show a linear melting point depression. Moreover, we found the discrete nature of nanoparticles during the early stage of thin film growth — the measured heat capacity values show several maxima at certain temperatures which suggest preferred states exist among supported nanoparticles. These maxima are related to each other by increments of one monolayer of indium atoms which can be extended from the magic numbers observed previously in cluster beams.

For the first time, the nanocalorimetry is utilized to characterize thin film growth in real-time. The technique generates 3-dimensional heat capacity data as a function of temperature and thickness that show the continuous change during deposition. The measurement interval is $\sim 4 \times 10^{-3}$ nm in thickness, increment of the heat capacity is ~ 30 pJ/K, and the temperature resolution is better than 0.5K.

The silicide study focuses on phase formation in Au-Si thin films. The unique finding is to determine the melting temperature of metastable phase using calorimetry, which is ~ 60 °C below the eutectic melting point (363 °C). The heat of fusion (26.4 kJ/mol) of the metastable phase has also been obtained. The metastable phase is analyzed to be an orthorhombic structure ($a=0.92$, $b=0.72$, $c=1.35$ nm) by double tilting experiment with stereographic projection method (ex-situ TEM). The composition is proposed to be Au_3Si from EDAX. The real-time experiment shows the melting point depression of eutectic and competitive growth between eutectic and Au_3Si phase. The composition of the film (i.e., gold-rich or silicon-rich) determines the formed phase. Rapid cooling experiments reveal that eutectic is supercooled down to much lower temperatures (~ 135 °C) than the Au_3Si phase (~ 275 °C).

Dedicated to my family

ACKNOWLEDGEMENTS

I thank Professor Les Allen. He is my advisor who leads me to the nanocalorimetry. Thanks are due to his patient allowing me to fail and to learn. His encouragement during the work is important. I thank Professors Joe Greene, David Cahill and Joe Lyding for serving on my thesis committee and open discussions.

I have been benefited from valuable experiences co-working with Dr. Mikhail Yu Efremov. Dr. Francois Schiettekatte contributed image analyses and thermodynamic models as well as the “magic number” analyses on indium nanoparticles; Dr. Jianguo Wen provided critical support in microscopy analyses on gold silicide studies. I worked with Mr. Doug Jeffers in making the nanocalorimeter sample stages and modifying the UHV chamber at the MBE Facility to realize the silicide experiment. I have been lucky to work with Dr. Eric Olson on similar problems using the nanocalorimetry technique.

The nanocalorimeter sensor is fabricated at the Cornell Nano-Scale Science & Technology Facility, supported by the NSF under Grant ECS-9731293, at Cornell University, Ithaca, New York. Mr. Phil Infante is our host staff. He has provided technique support and brought in important suggestions.

I thank the Center for Microanalysis of Materials at Materials Research Laboratory, University of Illinois, which is partially supported by the U.S. Department of Energy under grant DEFG02-91-ER45439 for the use of facilities. Dr. Ray Twesten and Mr. Mike Marshall trained me on TEM. They also tested my self-design/machined sample holder, allowing direct TEM analyses. Dr. Nancy Finnegan helped me on contamination analysis using AES. Dr. Ivan Petrov trained me on RBS. I thank for their help.

TABLE OF CONTENTS

| | |
|--|----|
| LIST OF FIGURES | x |
| CHAPTER 1 INTRODUCTION | 1 |
| 1.1 Small materials | 1 |
| 1.2 Silicides | 2 |
| 1.3 Challenges | 4 |
| 1.4 References | 6 |
| CHAPTER 2 NANOCALORIMETRY | 8 |
| 2.1 Introduction | 8 |
| 2.2 Basic principle and operation of nanocalorimetry | 9 |
| 2.3 MEMS sensor fabrication | 13 |
| 2.4 TEM nanocalorimeter | 19 |
| 2.5 Several problems and discussion | 23 |
| 2.6 References | 26 |
| 2.7 Figures | 27 |
| CHAPTER 3 SIZE-DEPENDENT NANO-STRUCTURE MELTING | 32 |
| 3.1 Introduction | 32 |
| 3.2 Melting models | 34 |
| 3.3 Experimental procedure | 36 |
| 3.4 Result and discussion | 39 |
| 3.4.1 Effects of the melting point depression on TDSC measurements | 39 |
| 3.4.2 Size-dependent effects | 42 |
| 3.4.2.1 Size dependence of the melting point | 42 |
| 3.4.2.2 Size dependence of the latent heat of fusion | 46 |

| | | |
|--|--------------------------------------|----|
| 3.5 | Conclusion | 49 |
| 3.6 | References | 49 |
| 3.7 | Tables and Figures | 52 |
| CHAPTER 4 DISCRETE MELTING OF NANO-STRUCTURE ENSEMBLES | | 62 |
| 4.1 | Introduction | 62 |
| 4.2 | Experimental procedure | 64 |
| 4.3 | Result and discussion | 65 |
| 4.4 | Conclusion | 69 |
| 4.5 | References | 69 |
| 4.6 | Figures | 72 |
| CHAPTER 5 REAL-TIME NANOCALORIMETRY | | 75 |
| 5.1 | Introduction | 75 |
| 5.2 | Fast heat capacity calculation | 77 |
| 5.3 | Experimental procedure | 80 |
| 5.4 | Result and discussion | 81 |
| 5.5 | Conclusion | 84 |
| 5.6 | References | 84 |
| 5.7 | Figures | 86 |
| CHAPTER 6 GOLD SILICIDE FORMATION | | 90 |
| 6.1 | Introduction | 91 |
| 6.2 | Experimental procedure | 93 |
| 6.2.1 | Evaporation system | 93 |
| 6.2.2 | Nanocalorimetry measurement | 95 |
| 6.2.3 | TEM analysis | 96 |
| 6.2.4 | Sample alignment | 96 |

| | | |
|--------|--|-----|
| 6.3 | Result and discussion | 97 |
| 6.3.1 | As-deposited sample | 97 |
| 6.3.2 | Low temperature annealed Au/Si sample | 98 |
| 6.3.3 | The caloric result on deposited silicon layer | 99 |
| 6.3.4 | In-situ real-time observation of phase formation | 100 |
| 6.3.5 | Identifying the metastable phase | 103 |
| 6.3.6 | Stoichiometry | 108 |
| 6.3.7 | Epitaxial relation | 109 |
| 6.3.8 | Growth model | 110 |
| 6.3.9 | Cooling experiment | 111 |
| 6.3.10 | Models on phase formation | 112 |
| 6.3.11 | Thermodynamic properties | 114 |
| 6.4 | Conclusion | 115 |
| 6.5 | References | 116 |
| 6.6 | Figures | 118 |
| | CHAPTER 7 SUMMARY AND FUTURE WORK | 135 |
| | VITA | 138 |

LIST OF FIGURES

| Figure | | Page |
|--------|--|------|
| 2-1 | The planar and cross-sectional configurations of a nanocalorimeter sensor developed during this work. The sensor consists a 35~50 nm thick amorphous silicon nitride membrane supported on a silicon frame, and a 50 nm thick patterned metal layer. | 27 |
| 2-2 | The principle circuitry of the differential scanning nanocalorimetry: two identical sensors are used — the sample sensor contains the interested material, and a reference sensor with no sample. DC current pulses through the sensors are precisely synchronized. Five electrical measurements are taken simultaneously: currents through sample and reference I_S and I_R ; voltages across sample and reference V_S and V_R ; and the differential signal ΔV , which reflects the difference between the two sensors due to the presence of the sample. | 27 |
| 2-3 | An illustration of the nanocalorimeter sensor fabrication: the process can be summarized as follows: (1) to use PR as a mask to etch silicon nitride; (2) to used nitride as a mask to remove silicon; (3) to pattern metal layer on the membrane. | 28 |
| 2-4 | Example of a high-resolution TEM image of annealed gold nano particles on a TEM nanocalorimeter sensor. | 29 |
| 2-5 | Masks for TEM nanocalorimeter sensor fabrication. The top one is for opening the nitride windows; the bottom one is for the metallization. | 30 |
| 2-6 | An example of a nanocalorimeter sensor loaded in a JOEL 2010 TEM single tilt stage. The tip holder is made of aluminum. The nanocalorimeter sensor slides into the holder and is clipped by a spring finger made from beryllium copper. | 31 |
| 3-1 | Plan-view and cross-sectional representations of the Thin-film calorimeters used for this study. The current pulse is driven between paddles 1 and 4, and the voltage is measured across the central part of the calorimeter using paddles 2 and 3. Differential measurements are achieved by using a second calorimeter on which no sample is deposited. | 53 |

| | | |
|-----|---|----|
| 3-2 | Normalized calorimetric curves [i.e., $C_p(T)/\text{mass}$] obtained for the 1.3 nm, 2.3 nm, 3.2 nm 5.6 nm and 11.0 nm indium depositions. The inset shows the progression of the peak temperature and the Full Width at Half Maximum (FWHM) of the melting peak with deposited thickness. | 54 |
| 3-3 | TEM images and associated particle size distributions of the (a) 1.3 nm and (b) 5.6 nm samples of Figure 3-2. The particle size distributions (in [particles/nm ²]/nm) are multiplied by the volume of the particles ($4\pi r^3/3$) so the vertical axis have no dimensions. | 55 |
| 3-4 | Raw data of the heat of fusion (integral of the melting peak) as a function of the deposited thickness for all the experiments. The solid line represents the expected value if all the deposited indium was melting with the bulk heat of fusion. | 56 |
| 3-5 | TEM images, particle size distribution and associated calorimetric data for the 0.1 nm, 0.2 nm, 0.3 nm, 0.4 nm indium depositions. The radius R_L corresponding to the lower limit temperature T_L is indicated. | 57 |
| 3-6 | Schematic representation of the procedure used to determine the relationship between the melting temperature T_m and the particles radius r . (a) the normalized particle size distribution, which has the same area under the curve than the melting peak in (b) which is the corresponding calorimetric curve. The temperature T_m at which the particles with a radius r melt is such that the area under the right part of both curves is equal. | 58 |
| 3-7 | Result of the calculation schematically described in Figure 3-6 as a function the reciprocal radius. (a) Result for each experiment; (b) Average of the results in (a) (symbol \circ). This average result is compared with different melting models (lines). | 59 |
| 3-8 | Heat of fusion as a function of the reciprocal radius deduced from the melting peak and the estimated melting mass of each experiment (see Section 3.4.2.2 for the details of the calculation). The horizontal solid lines indicate the radius range to which the calculation applies in each case. The dashed line is a linear regression through the data. The dotted line represents the theoretical size-dependence deduced from the thermal chemical cycle of Figure 3-9. | 60 |
| 3-9 | The thermochemical cycle, used to estimate of size dependence of the latent heat of fusion $H_m(r)$ using the Hess' Law. $S_p(r)$ and $N_p(r)$ denote the area of particles and the number of particles that can be made from 1 g of indium, respectively; see text for other definitions. | 61 |

| | | |
|-----|--|----|
| 4-1 | The schematic diagram of the nanocalorimeter showing two metallic strips, which serve as both heaters (sample and reference) and thermometers. These strips are supported by a thin SiN _x membrane. Indium is deposited on the membrane side of the nanocalorimeter directly above the sample heater. 72 | 72 |
| 4-2 | Ex situ TEM micrographs of the nanoparticles generated in the deposition experiments of the (a) 0.4 nm, (b) 0.6 nm, and (c) 0.8 nm indium films. Corresponding calorimetric curves (d) with vertical dashed lines indicating the position in temperature of each maximum. (e) Radius difference corresponding to the separation between adjacent maxima, as calculated using Equation (4-2). The horizontal dashed lines represent the thickness of a monolayer for the two bulk lattice parameters of indium. 73 | 73 |
| 4-3 | Number of the atoms corresponding to the size of the particles associated with each melting point maxima T_m^i in comparison to the atomic and the electronic magic numbers. 74 | 74 |
| 5-1 | 3D plot of heat capacity vs. temperature vs. thickness during the vapor deposition of indium. The plot is generated using sequential individual scans with a heating rate of 30k K/s taken at 1s intervals. The film is discontinuous and consists of nano indium particles. Three distinct features are in the plot. (A) the liquid region which is used to track the growing of thin film on the sub-angstrom scale; (B) the main melting peak of the film which illustrates size-dependent melting; and (C) the multiple maxima, constant in temperature and related to magic number nanoparticles. 86 | 86 |
| 5-2 | (a) Heat capacity of liquid indium (region A in Figure 5-1). For each scan the heat capacity is approximately constant. However, as deposition proceeds the heat capacity of the film increases, as does the mass of the indium; (b) Temperature averaged heat capacity from (a). The inset shows an expanded region of a small section of the main graph. The spacing between adjacent points is 0.04 Å in thickness and 30 pJ/K in heat capacity, illustrating the ultra-fine detail of the technique. 87 | 87 |
| 5-3 | (a) The increase of melting temperature during film growth. (b) The main melting peak increases continually from 100 to 135 °C as the integrated film thickness increases from 0.5 to 1.3 nm. This shift is due to the increase of average nanoparticle size. This is an example of melting point depression phenomenon. 88 | 88 |

| | | |
|-----|--|-----|
| 5-4 | At the early stages of deposition, some selected nanoparticles are favored over other sizes due to increased thermodynamic stability. As shown in (a) there are multiple maxima in the caloric curve. The maxima temperature correspond to discrete sizes, which is illustrated as schematic inset of nano particles with incremental atom layers. Unlike the melting peak shift, shown in Figure 5-3, the melting points of selected nano particles are relatively constant. This is seen in (b) where the value of the first maxima in (a) remains at 60.0 ± 0.2 °C. The ability to observe this high degree of stability is due the reduction of systematic errors by the use of real-time measurements. | 89 |
| 6-1 | The illustration of the custom optimized UHV chamber. (a) The system uses thermal method to evaporate silicon and gold. The vertical distance between the evaporation sources and the sensor stage is ~30 cm. The thickness is controlled by the shutter with a calibrated crystal monitor. (b) The top view as indicated from the arrow in (a) shows the arrangement of evaporation sources and the sample sensor. The configuration minimizes the possible non-overlapping problem due to applying a shadow mask. | 118 |
| 6-2 | Au-Si equilibrium phase diagram (after H. Okamoto and T. B. Massalski, 1987). The dashed line indicates the highest temperature in nanocalorimetry scans. | 119 |
| 6-3 | (a) The TEM bright field image of the as deposited Au(13.7nm)/Si(29.1nm) sample on a 20nm thick silicon nitride membrane. (b) The SAD pattern reveals that the sample consists of ploy crystalline gold and amorphous silicon. The intensity profile of the SAD pattern is shown in (c). | 120 |
| 6-4 | The TEM analyses on the Si(3.7nm)/Au(15.7nm) sample influenced by heating. (a) The bright field image of the sample. The SAD pattern of the sample is compared with the patterns from a standard poly crystalline gold sample (b) and a reacted gold-silicon sample (c). | 121 |
| 6-5 | Using caloric curve to determine the mount of deposited silicon on the sensor. The silicon mass (or thickness) is obtained by correlating the measured heat capacity curve with a calculated one from the specific heat capacity. | 122 |
| 6-6 | The real-time nanocalorimetry results during the gold deposition. The surface has originally been covered with a 3.7 nm thick silicon layer. Totally 5.9 nm gold has been deposited. First ~1nm gold adding to the surface only increases the heat capacity of the sample. Afterwards the evolution of two melting peaks has been observed. The melting peak B is from gold silicon eutectic alloy. The melting peak A is from a metastable phase. Both the eutectic alloy and the metastable phase show melting point depression in the early stage of thin film growth. | 123 |

| | | |
|------|---|-----|
| 6-7 | TEM Analyses of the Si(3.7nm)/Au(4.3nm) sample prepared under similar experimental conditions described in Figure 6-5 where melting peak B dominates. (a) A bright field image of the sample. Silicon is plate like while gold can be large or small particles in between or attached to the silicon. (b) A STEM (z-contrast) image showing the locations of the gold (bright features). (c) A high-resolution image of one gold rich region on the silicon surface showing the gold and silicon lattice images. (d) A bright field image of bulk behaved gold-silicon eutectic. | 124 |
| 6-8 | Continuing experiment initiated in Figure 6-6. Competitive growth between the gold-silicon eutectic alloy (peak B) and the metastable phase (peak A) has been observed in the real-time gold deposition. As more gold deposited on to the surface, the metastable phase dominates. | 125 |
| 6-9 | The TEM images of the repeatedly quenched Si(3.7nm)/Au(15.7nm) sample that corresponds to the metastable phase (melting peak A in Figure 6-6 and 6-8). (a) The low magnification image shows the large area morphology of the sample. (b) The agglomerated sub-micron particles nearby the metal heater are the interested gold-silicon samples. (c) The SAD pattern of the sample reflects a complex crystalline structure. | 126 |
| 6-10 | The double tilting experimental results on the gold-silicon metastable phase. The diffraction patterns are consistent with a B-centered orthorhombic unit cell with $a=0.92$ nm, $b=0.72$ nm, $c=13.5$ nm. The diffraction patterns corresponding to zone axes [100], [011], [101], [011], [111], [201] have been illustrated. | 127 |
| 6-11 | A STEM (z-contrast) image of the Si(3.5nm)/Au(64nm) sample. Since the gold-silicide phase has light silicon atoms, the density is lower than that of the gold. One can clearly see that majority of the gold is in the center and silicide is on the shell or skin like. | 128 |
| 6-12 | The strong epitaxial relation between the gold and the silicide is illustrated. The SAD pattern shows Au[111]//Au ₃ Si[100]. A roughly 4 time relation has been found. | 129 |
| 6-13 | The proposed model for real-time deposition experiment described in Figure 6-6 and 6-8. (1) A layer of silicon film (4nm) is first deposited on the silicon nitride membrane. (2) First several monolayers gold on top of silicon forms a mixed layer. No melting peak has been observed at this stage. (3) The eutectic (melting peak B) and metastable phase Au ₃ Si (melting peak A) form, showing size-dependent melting (beginning) and competitive growth (later). (4) Finally only Au ₃ Si phase presents at gold-rich region. (5) Further depositing gold changes the morphology of the sample. The liquid expels excess gold to the solid gold core before solidification, thus the Au ₃ Si phase is skin or shell like. Epitaxial Au ₃ Si phase on gold can be observed. | 130 |

| | | |
|------|--|-----|
| 6-14 | Heating and cooling experimental results of the metastable phase (melting peak A) sample and the metastable phase (melting peak A) plus eutectic alloy (melting peak B) sample. As one can see that eutectic alloy has much stronger supercooling than that of metastable phase. | 131 |
| 6-15 | Illustrations on the phase formation. Under the experimental conditions (quenching), “gold-rich” samples tend to form Au ₃ Si phase; “silicon-rich” samples tend to form eutectic. The phenomenon can be explained by the difference in nucleation and growth, or the difference in the liquid. Details can be seen in text. | 132 |
| 6-16 | The caloric curves with excess gold showing the metastable phase melting peak. The heat of fusion can be calculated by measuring the area under the melting peak. 26.4 kJ/mol (in terms of Au ₃ Si) is obtained independently. | 133 |
| 6-17 | The caloric curve showing two melting peaks (metastable phase melting and eutectic alloy melting) can be used to estimate the heat of fusion of the eutectic alloy. The amount of silicon in the metastable phase can be calculated using the result from Figure 6-16. | 134 |

CHAPTER 1

INTRODUCTION

This thesis presents a study of a material investigation: the properties of indium nanoparticles and the interaction characteristics between the gold and silicide. The main experimental method — nanocalorimetry — is based on the unique ultra thin membrane sensor device and is discussed in Chapter 2. Chapter 3 describes the experiments on thermal properties of indium nanoparticles — the sized dependent melting point and latent heat of fusion depression. Chapter 4 discusses the discrete nature of annealed indium nanoparticles, which is an extension of “magic number” phenomenon. Chapter 5 is on real-time nanocalorimetry and using indium as an example to observe early stage thin film growth. Chapter 6 is the first real-time in-situ investigation on gold silicide formation during the thin film deposition, and the first qualitatively study on (rapid) cooling characteristics of the gold silicide sample. Finally, in Chapter 7, a summary and expectation on nanocalorimetry is briefly presented.

1.1 Small materials

Thermodynamic properties of material at the nanometer scale are current of interest because of the basic science issues and potential applications [1]. However, unlike bulk materials, fundamental understandings on small systems are still far from complete.

The size dependent phenomena are the result of surfaces or interfaces, which is usually negligible when materials are in the bulk form. For instance, in a spherical particle with a diameter of 2nm, about 40% of the atoms are on the surface. When atoms are on the surfaces,

their bonding and energy characteristics are much different from the atoms in the interior. This difference profoundly changes the material behaviors as compared to the bulk material having large dimensions.

Classical thermodynamics treatment generally incorporates the influence of the surface atoms on the whole physical object by introducing a surface term in system free energy [2]. Assuming a spherical crystal contains N atoms and the surface energy (γ) is isotropic, at constant pressure and temperature, the free energy of the system is:

$$G = G^{bulk} + A\gamma \quad (1.1)$$

where G^{bulk} is the Gibbs free energy of the bulk and A is the surface area, respectively. Then, the chemical potential of the whole system can be written as:

$$\mu = \left(\frac{\partial G}{\partial N} \right)_{T,P} = \mu^{bulk} + \frac{3v_0}{r} \gamma \quad (1.2)$$

where v_0 is the atomic volume and r is the radius. For small systems, the surface term ($\frac{3v_0}{r} \gamma$) is not negligible. This contribution will drive the small system away from well-characterized bulk status.

1.2 Silicides

Silicides are fundamental research interests because of the irresistible propelling force from advancing silicon industries. On the other hand, silicides are also very practical engineering problem connected to applications [3].

Au-Si has become a traditional model system for such investigations over fifty years. Gold is a noble metal. It has excellent electrical, thermal conductivity, and oxidation resistant properties [4]. In equilibrium, gold and silicon are almost immiscible to each other. They form

eutectic at 363 °C and the eutectic composition is 18.6 at.% silicon. The application of gold in silicon technology on the device level is quite limited because gold diffuses into silicon and segregates that will shunt transistors or drastically reduces the minority carrier lifetime. However, it does have technological applications in packaging applications due to its low eutectic temperature characteristics. The low eutectic temperature has also been utilized to form Si nanowires from vapor using Au nanodots [5]. There is also exciting research currently on the fabrication of Au nanowires on Si [6].

Metastable silicides have been observed for quite long time and can be obtained by several methods including quenching liquid alloy ($10^3 \sim 10^6$ K/s), ion mixing, vapor deposition or annealing amorphous Au-Si above transition temperatures [7]. Major efforts have been put into interpreting electron and X-ray diffraction data generated from these metastable phases. However, gold silicides are still not clearly understood. Numerous metastable phases have been reported, in several cases even under similar experimental condition [7]. Hultman et. al. [8] suggested that all the reported gold silicide can be related to one single phase. They suggested a cubic crystal with lattice parameter of 2.24 nm and the composition is estimated to be Au_4Si . Although their suggested metastable phase can explain many of diffraction patterns among the different research groups, the fact is that important low index diffraction patterns are not available to clarify the situation.

All these suggest that more careful work should be done on this system. New experimental techniques such as nanocalorimetry are now available to characterize additional properties of the system and hopefully provide more information to understand what is really going on in this model system.

1.3 Challenges

While it is safe to attribute size dependent phenomena to the role of surface or interface, the real situation in experiments for growing and characterizing nano-scale material is not so simple. For example, some constants that have been well characterized for the bulk materials (e.g., surface energy, crystal structure) may not be suitable for small materials; the surface phenomenon may be related with different crystalline orientations, etc. The truth is rather complex when a system scales down to several nanometers where classical behaviors become less dominant and quantum effects show up [1, 9].

From experimental viewpoint, a system dealing with surface effects requires more careful control in sample preparation and characterization. Contamination may compromise the results, or, even cover the truth. I do believe that most of the experimental observations reflect the nature of something, but unfortunately, not all of them are complete enough for people to explore the nature of the nature, since some important parameters may have been ignored or not available for tracking the experiment. The breakthrough in silicon device technology is a good example: it doesn't work until people finally can control the surface and impurity [10].

Small material analyses also challenge modern analytical techniques. That is the reason for the constant need for improvements in this area. For instance, the Charge Coupled Device (CCD) has been equipped in recent Transmission Electron Microscopes (TEM). In an old fashion way, it can be an art even for experienced operators to capture a high quality image because of the difficulty in fine stigma adjustment by human eyes. Nowadays, it is easy and convenient to take a TEM picture with the CCD camera and to control the stigma through a real-time live Fast Fourier Transformation (FFT) analysis. Experimental tools like TEM, AFM (Atomic Force Microscope), and STM (Scanning Tunneling Microscope) also extend our vision

down to atomic level. However, one has to be careful when applying localized observation to the whole picture. Also, one has to be aware that artificial effects may attenuate our observations, for examples, energetic electron beam influence to the nanoparticles that has been recently realized in TEM; and contamination or contamination related decomposition in some samples. For the same reason, one has to understand what an instrument could do and what is the equipment limit. In this sense, studies dealing with surface, interface and ultra thin films can be difficult and usually more costly.

Unlike microscopy, calorimetry, the primary technique for studying material transformations, has experienced “little” improvement because the thermal mass of the calorimeter sensor can not be scaled down correspondingly in order to measure very small amount of heat [11, 12]. The current Differential Scanning Calorimetry (DSC) typically has a sensitivity of $50 \sim 500 \text{ mJ/cm}^2$, which is orders too rough to sense the nanometer sized systems where heat exchange is only in nano Joule range. Although people can construct multilayer structures to investigate the interface phenomena, or embed the small particles in a matrix in a bulk sample (e.g. Au nanoparticles in SiO_2) in order to effectively increase the sample volume. However, most surface and early stage thin film studies can not use such an approach. The situation has to be changed by new inventions.

Nanocalorimetry is a recent technique to scratch the itch [13]. Its working principle is very simple, just like the transient that Tomas Edison turned on his first light bulb one hundred years ago — the Joule heat quickly elevates system temperature (several thousands degree per second) and heating characteristics can reflect the small material change.

The realization of the nanocalorimetry relies on two engineering advances: (1) the MEMS (Micro Electronic Mechanical System) technique allowing fabrication of membrane

sensors, and (2) fast digitizing technique for signal measurement. The membrane sensors consist of only two layers (one silicon nitride layer for support and a patterned metal layer as both micro heater and resistive thermometer) which are less than 100nm thick and thus have extremely low thermal mass. Fast digitizers can record small material changes in a short time period (usually several milliseconds).

The work presented in this thesis uses nanocalorimetry technique to study small materials. During the thesis work, nanocalorimeter sensor, sensor fabrication, calibration, sample stage and electronic system for nanocalorimetry have been improved. More recently, a new ADC system has been employed with much lower noise; and an automated control system has been constantly updated allowing more reproducible measurements.

1.4 References

1. Berry, R.S., *Thermodynamics: Size is everything*. Nature, 1998. **393**: p. 212.
2. Gaskell, D.R., in *Physical Metallurgy*. 1983, Elsevier Science: New York.
3. Mayer, J.A., Lau, S. S., *Electronic Materials Science: For Integrated Circuits in Si and GaAs*. 1990, New York: Macmillan Publishing Co. 476.
4. *CRC Handbook of Chemistry and Physics*. 78 ed. 1997, Boca Raton, N.Y.: CRC Press.
5. Westwater, J., Gosain, D. P., Tomiya, S., Usui, S., Ruda, H., *Growth of silicon nanowires via gold/silane vapor-liquid-solid reaction*. J. Vac. Sci. Technol. B, 1997. **15**(3): p. 554.
6. Robinson, I.K., Bennett, P. A., Himpsel, F. J., *Structure of quantum wires in Au/Si(557)*. Phys. Rev. Lett., 2002. **88**(9): p. 0961041.
7. Okamoto H. and Massalski, T.B., *Phase diagram of Binary Gold Alloys*. 1987: ASM INTERNATIONAL. 266.
8. Hultman, L., Robertsson, A., Hentzell, H. T. G., Engstrom, I., Psaras, P. A., *Crystallization of amorphous silicon during thin-film gold reaction*. Journal of Applied Physics, 1987. **62**(9): p. 3647.
9. Schmidt, M., Kusche, R., von Issendorff, B., Haberland, H., *Irregular variations in the melting point of size-selected atomic clusters*. Nature, 1998. **393**(6682): p. 238-40.

10. Bardeen, J., *The Early Days of the Transistor*. 1979: Urbana, Ill.: University of Illinois at Urbana-Champaign, Dept. of Physics.
11. Hemminger, W., *Grundlagen der Kalorimetrie. English*, ed. Y. Goldman. 1984: Weiheim; Deerfield Beach, FLa. :Verlag Chemie.
12. *Experimental Thermodynamics*, ed. J.P. McCullough, and Scott, D. W. 1968: Butter Worths, London.
13. Lai, S.L., Ramanath, G., Allen, L. H., Infante, P., Ma, Z., *High-speed (10^4 degrees C/s) scanning microcalorimetry with monolayer sensitivity (J/m^2)*. Applied Physics Letters, 1995. **67**(9): p. 1229-31.

CHAPTER 2

NANOCALORIMETRY

2.1 Introduction

Calorimetry is a powerful experimental tool to measure the heat. The measurement allows access to those highly theoretical quantities, like entropy (S) and enthalpy (H), and through these to free energy (G). Based on experimentation with the heat, thermodynamic was established as an all-encompassing theory of the nature.

There have been various idealized theories in calorimetry as well as widespread application and treatment in history [1]. They are usually classified in terms of the operation method, i.e., isothermal, isoperibol, adiabatic, scanning, etc. Commercial calorimeter systems like Perkin Elmer differential scanning calorimeter (DSC) have been available in many research laboratories as a standard experimental tool. The techniques have been continuously updated for several generations in the last twenty years due to the advances in related areas: data acquisition, digital signal processing and electronics. Calorimeters have been successfully used in measuring the enthalpy of reactions and phase transitions.

Surfaces and nano materials are the current research frontier. Thermal properties of small systems become important [2]. Unfortunately, few experimental methods can provide such information. Traditional calorimetry is not sensitive enough in this case because the available sample is of several orders too small (nanograms vs. milligrams). Simply adding more samples doesn't help or becomes impractical because small features might interact if they overlap each other. The inherent limit is due to the thermal mass in

the conventional calorimeter sensor — any extremely small signal will be masked by the noise contribution from the calorimeter apparatus.

Lai and Allen [3] first introduced the nanocalorimetry approach to solve this problem. Based on their work, the following sections in this chapter will concentrate on (1) basic principle and operation of the nanocalorimetry, (2) membrane sensor fabrication, (3) TEM nanocalorimeter, and (4) several problems and discussion.

2.2 Basic principle and operation of nanocalorimetry

A calorimeter is a device that thermally isolates a sample, puts in heat ΔQ , and measures the resulting temperature change ΔT by a thermometer. The elements of the device are (1) sample holder, (2) heater, and (3) thermometer. For an adiabatic calorimeter where there is no heat loss, $\Delta Q/\Delta T$ yields the heat capacity (C_p) of the sample plus the holder, thermometer, and heater (so called addenda). The sample heat capacity is inferred by subtracting $C_{p_{addenda}}$ that can be measured either before or afterwards with no sample present.

$$C_{p_{sample}} = C_{p_{sample+addenda}} - C_{p_{addenda}} \quad (2.1)$$

Practically, any heat capacity measurement has experimental uncertainty,

$$C_{p_{sample+addenda}} = \overline{C_{p_{sample+addenda}}} \pm \Delta C_{p_{sample+addenda}} \quad (2.2a)$$

$$C_{p_{addenda}} = \overline{C_{p_{addenda}}} \pm \Delta C_{p_{addenda}} \quad (2.2b)$$

thus,

$$\overline{C_{p_{sample}}} = \overline{C_{p_{sample+addenda}}} - \overline{C_{p_{addenda}}} \quad (2.3a)$$

$$\Delta C_{p_{sample}} = \Delta C_{p_{sample+addenda}} + \Delta C_{p_{addenda}} \quad (2.3b)$$

When $\overline{Cp} \ll \Delta Cp$, the result becomes untrustable. This is exact the case using traditional calorimetry to study small material systems where the noise is of orders larger than the signal. Simply improvement from electronic system and signal processing does not basically change the situation because this type of experimental uncertainty is often connected with how big the total signal is. Thus, to reduce the thermal mass of a calorimeter sensor becomes the central idea for the invention of nanocalorimeters.

A nanocalorimeter sensor follows the tradition concepts. The whole sensor is fabricated on an ultra thin membrane. $Cp_{addenda}$ is extremely small in this approach. Correspondingly, a much smaller experimental uncertainty is expected. A typical $Cp_{addenda}$ value is $\sim 10^2$ nJ/K and ΔCp approaches to $\sim 10^{-1}$ nJ/K, respectively. This makes the thermal analyses on submonolayer thick materials possible.

Figure 2-1 is an example of the planar and cross-sectional configurations of a typical calorimetric sensor developed during this work. The sensor consists a 35~50 nm thick amorphous silicon nitride membrane supported on a silicon frame. The membrane window size is about 3 mm \times 7 mm. A patterned metal strip is deposited on the front side of the membrane. The strip is usually 50 nm thick and 500 μ m wide. It serves as both a resistive heater and a resistive thermometer for the measurement. Two voltage senses are formed on the membrane as a part of the patterned metallization layer in order to measure voltage across the working part of heater placed on top of the membrane. The metallization patterns include four contact pads on the silicon frame, electrically connected with the metal strip and the senses, which are the terminals for electrical contacts.

The region of the heater situated between the voltage senses and the part of membrane beneath it form a calorimetric cell. Samples can be loaded onto either side of the sensor cell (nitride or metallization side), except for conductive materials, which are able to change the electrical properties of the metal strip, therefore should be placed only on the nitride side of the cell.

The calorimetric scan is initiated by applying a short (milliseconds) dc electrical current (tens of milliamperes) through the metal strip. The calorimetric cell heats up by Joule heating, while the part of the strip placed on the silicon frame remains cold due to the high heat capacity of the silicon frame (in comparison with the nitride membrane). The current I through the sensor and the voltage V across it (typically a few volts) are measured as functions of time t . The resistance of the sensing area of the heater can be

calculated as $R(t) = \frac{V(t)}{I(t)}$ and the electrical power generated in the calorimetric cell is

$P(t) = V(t) \times I(t)$. The $R(t)$ function is used to calculate the temperature $T(t)$ of the sensing part of the metal strip. To do this, the resistance of the nanocalorimeter sensor is calibrated against the temperature in a high vacuum three-zone tube furnace before hand.

To obtain a sensor with a stable electrical response, a two-step annealing procedure is performed before calibration. First, sensors are annealed in vacuum of $\sim 10^{-6}$ Pa at typically 450 °C for 8 h. The temperature of annealing should be increased if calorimetric data above 350 °C to 400 °C are desired. Note higher annealing temperatures can lead to an increase in the electrical resistance of sensors, so compromise has to be made. Second, sensors are “burned-in” under the same vacuum conditions using a dc electrical pulse to heat the sensor to a temperature higher than needed for the actual measurement. Usually several thousand pulses are used to burn in and stabilize

each sensor until the drift characters of the sensor are within the accepted ranges. Calibrated sensors with Al, Ni or Pt metallizations can be kept in air at least for several months without noticeable degradation of their electrical characteristics. Immediately before a calorimetric experiment, the burning-in process is repeated to ensure the quality of the measurement.

Under adiabatic conditions, the heat capacity C_p of a calorimetric cell (bare or with a sample on it) can be calculated by:

$$C_p(t) = \frac{dQ(t)}{dT(t)} = \frac{P(t)dt}{dT(t)} = \frac{V(t) \times I(t)}{dT[R(t)]/dt} \quad (2.4)$$

since all the generated heat is consumed to increase the temperature of the cell. Practically to achieve nearly adiabatic conditions, the heating rate for a sensor should be much faster than the cooling rate. In vacuum better than 10^{-2} Pa, where convection is negligible, the main mechanisms of heat loss are (1) heat conduction through the silicon nitride membrane and the metallization layer, and (2) infrared emission. Typical cooling rates at a temperature range of 100 ~ 300 °C are ~ 10^3 K/s, so heating rates of tens of 10^3 K/s or higher are mandatory for the measurements in near adiabatic mode.

To use the advantages of a differential measurement, two identical sensors are employed in one pair: a sample sensor that can contain the interested material, and a reference sensor, with no added material. DC current pulses through the sensors are precisely synchronized. Five electrical measurements are taken simultaneously in the differential scheme: currents through sample and reference sensors I_S and I_R , respectively; voltages across sample and reference sensors V_S and V_R , respectively; and the differential signal ΔV , which reflects the difference between the two sensors due to the presence of the sample. The principle circuitry in the differential measurement is shown in Figure 2-

2. The sampling rate for these electrical measurements is typically 100 kHz, which corresponds to a temperature resolution of ~ 0.3 K/sample at a heating rate of 30,000 K/sec.

For a nanocalorimetry experiment, heat capacity can be calculated using Equation (2.4). However, special methods in data processing have to be taken in order to suppress the noise, and corrections have to be made for the measurement [4].

2.3 MEMS sensor fabrication

Sensor fabrication is the first important step in nanocalorimetry. The quality of the fabricated sensors not only influences all the later steps in nanocalorimetry operation, but also determines the type of work that can be performed. Therefore, great care has to be taken. One mistake can make all of the other efforts useless.

Usually, the calorimetric sensor is designed to be a small device produced in batches. It can be treated as a one-use, disposable item, depending on the nature of experimental interests. Up to 39 sensors are made in one 3-inch wafer. More than 12 wafers can be processed in one batch. The whole fabrication time is around one week.

Processing facility is essentially important for the work. Besides expensive capital equipment involved, experienced technique support and custom modified accessory parts are often of necessary to insure the yield and quality of the processing. During this work, all the nanocalorimeter sensors are fabricated at Cornell Nanofabrication Facility, the national MEMS developing center at Cornell University. Although fabrication uses standard MEMS techniques and the designed smallest feature is well above the processing limit ($5\mu\text{m}$), patterning on such big size window ($3\text{mm}\times 7\text{mm}$) and so thin

membrane (30~50nm thick) is quite unique in the world. Special details have to be polished.

Schematic cross sections of the wafer at each steps of the fabrication process are presented in Figure 2-3. Details are described as follows:

- (0) The original wafers are (100) oriented silicon. The resistivity is $>1 \Omega\text{-cm}$. Wafers are double side polished because photolithography is to be done on both sides. Wafer thickness is usually about $250 \mu\text{m}$, which will influence required time for wet silicon etching and mechanical strength of the sensor.
- (1) Low stress silicon nitride membranes are coated on both sides of the wafers using an LPCVD process. The nitride layer is under tensile stress ($150\sim 200 \text{ M Pa}$). It is high-density, silicon rich, amorphous membrane with reflection index around 2.2. Membrane is fabricated at $\sim 800 \text{ }^\circ\text{C}$ and post annealed at $500 \text{ }^\circ\text{C}$ for several hours. The thickness of the nitride membrane is about 35 nm in this work. We do not grow nitride by ourselves because it is a very complex process and need special experienced people to work with. Both sides of the wafer are identical, and free of damage. In the following several steps, special care has to be taken to protect the membrane surfaces. Teflon coated tweezers with soft surfaces are used to handle these wafers.
- (2) On the front-side of the wafer (where finally the sensor is), Front Side Coating (FSC) is spin coated to prevent scratching the nitride membrane during backside lithography operations. FSC is a dark blue color photoresist (PR) with primer chemicals and need to be baked. Oven bake is employed at $90 \text{ }^\circ\text{C}$ for 1 hour in

stead of regular soft bake on hotplates to protect the bottom side nitride from scratching.

- (3) On the backside, rectangular areas (for opening windows) are patterned using optical lithography. MicroPrime P-20 primer and Shipley 1813 general-purpose broad band (365 nm ~ 436 nm) positive photoresist are used for spin coating. The obtained photoresist layer is about 1 μ m thick. PR is post baked at 110 °C for 1 min on a hotplate. No vacuum is applied during the bake because the FSC protection layer can be damaged. A 5x g-line (436 nm) stepper (GCA-6300B) is used for pattern transfer.
- (4) After developing, the exposed part of the nitride layer is etched away by reactive ion etching (RIE) using CF₄. The etching rate is about 40~50nm/min and selectivity between nitride and remained photoresist is about 1:1. Any damage to the unexposed PR and FSC, like scratches from handling the wafer, can open the under nitride membrane surface to the RIE. The damage can be further magnified in the following wet etching step. This will not only weaken the wafer for later processing but also make the second pattern transfer more difficult. To solve the problem before hand, wafer patterns are carefully examined. Additional PR is painted to cover all the damaged areas. After RIE, both front and back side coatings are striped out by solvent washing (acetone and 2-propanol, or warm (60 °C) 1165 solvent). Occasionally, there are polymerized PR residues from RIE process. They form spots on the surfaces. These residues have to be thoroughly removed by either oxygen plasma or chemical PR striper. The finished surfaces at the end of this step are mirror like.

- (5) The patterned silicon nitride membranes are the masks for silicon removing in this step. The wafer is etched in a 30~35 wt.% KOH solution at ~80 °C to remove silicon exposed in the previous step. The etching rate under such conditions is about 1 μm/min. KOH has a high selectivity for silicon over silicon nitride. It also etches silicon anisotropically, with a (100):(111) etch ratio of ~400:1 [5]. The resulting structure is a very thin nitride membrane on the front side of wafer, supported by the silicon frame. Wafers must be oriented vertically in the liquid solution, as vigorous bubbling can rupture the membranes. The end of the etching process is marked by the cessation of massive bubbling action.
- (6) After washing in warm (65 °C) and then room temperature (25 °C) water, the wafer is then isotropically etched in a solution of 450 mL HNO₃ : 225 mL H₂O : 3 mL HF for 5 min. This chemical is poly-silicon etchant and is used to remove microscopic residual silicon pyramids with (111)-terminated facets. At the same time, it also attacks silicon nitride at about 0.5 to 1 nm/min. This etch step can be prolonged to thin down nitride membranes. Since wafers have extremely fragile nitride windows in this and subsequent steps, great care is required in the handling of wafers, especially during washing and drying. Only gentle flows of solvents and dry air/nitrogen at small angles to the wafer surface should be used.
- (7) On the front side of the wafer, photoresist is spin coated on top of the nitride membrane. The procedure is similar to that in step 4, but slightly different: photoresist covers all the area that needs to be patterned before spinning. Special care should be taken near the edge and near the broken windows: not to let PR get under to the backside of the wafer. Since the wafer contains large thin membrane

- window arrays, vacuum should not be applied all the time. In stead, a custom-machined chuck is used. The wafer is kept against the inside edges of the chuck during spinning. The wafer has to experience a deceleration stage before stop. The post bake is also similar to that in step 4.
- (8) Patterns are transferred on to the front side of the wafer with nitride membranes. To align the features on both sides, special marks are prepared in step 4. They are now small through holes that can be captured by the stepper camera. Small pieces of removable tape have been used to fix the wafer position after alignment, since stepper moves wafer for exposure and no vacuum is allowed.
- (9) An ammonia diffusion process in a YES LP-III vacuum oven followed flood exposure is used to reverse the tone of the patterned image and to generate an undercut profile for successful lift-off. Wafers are developed and thoroughly washed. Usually, three or more steps of developing followed by quick water washing are suggested to keep the chemical fresh and to limit the dissolved PR concentration. Multiple washing is of necessary to remove the possible residues. The opened surfaces are for metallization. The property of the final metal layers will influence the performance of the calorimeters. Therefore, the finished wafer should be clean and uniform in color with no observable residue especially in the region where it last dries.
- (10) After developing, the metal layer is deposited onto the wafer using thermal or electron beam evaporation. The thickness of the layer is typically ~50 nm. Deposition of a thin (~3 nm) layer of titanium before the main metallization is helpful to promote adhesion to the nitride surface. Lift-off is performed using

acetone as a main solvent. At the end of this process, one has to make sure that all the small features have been lifted off. To ensure high quality sensors, care should be taken to completely remove all photoresist residues and the lifted-off metal pieces. Repeatedly 2-propanol and deionized water wash is highly suggested. Deionized water dissolves 2-propanol helping to remove small pieces attached to the sensors. Surface tension keeps these small pieces on the surface of water that is convenient to separate.

- (11) Individual sensors are cleaved from the wafer manually. Narrow lines etched into the wafer in step 4 help the accuracy of the cleaving. To clean the surface and remove dusts during the wafer cleaving, each nanocalorimeter sensor is washed separately before use in sequential baths of acetone, 2-propanol, deionized water, and 2-propanol.

The nanocalorimetry sensor fabrication is quite a long process. Each step has its own details. The fabrication process can be summarized as follows: 1) to use PR as a mask to etch silicon nitride; 2) to use nitride as a mask to etch silicon; 3) to pattern metal layer.

Before the KOH etching, one has to protect the membrane surface carefully, otherwise, a damaged silicon wafer is more of a challenge and adds more uncertainty to the operation. After KOH etching, how to clean the exposed surface becomes then critical. Residues may degrade the metal layer functions, attenuate calorimetric results, or contaminate the surface where the sample loads.

A nanocalorimeter sensor will experience fabrication, anneal, calibration, calorimetric measurement and several complementary experiments. Good quality sensors

can go through all of these steps with repeatable results, while potential problem sensors can break, or generate quite scattered data that makes the analyses complex.

Sensor fabrication is very important.

2.4 TEM nanocalorimeter

Nanocalorimeter is a powerful tool for characterizing small materials. The obtained information is essentially important, but still only a partial picture to solve the puzzle. More information from other experimental techniques is often of necessary to obtain the whole picture. This is true especially in current nanocalorimetry studies where both the phenomenon and the technique itself need to be further understood.

As a MEMS sensor, nanocalorimeter has advantages to combine with standard modern analytical techniques. For example, nanocalorimetry can provide thermal information of very small systems, while TEM is able to image very small features and do microstructure analyses. Combining these two techniques will dramatically change the situation in current researches. Just like that in bulk material investigations, using calorimetry to study the reactions or phase changes, and through X ray results to get crystalline information, nanocalorimetry plus TEM will enable similar researches on the nanometer scale where few experimental methods are available.

The silicon nitride membrane used in this thesis work is 35~50 nm thick. Such thin film is transparent to the electron beams. The RMS roughness of the membrane is only 0.4 nm. Both silicon and nitrogen are light atoms. Background under the TEM is bright and uniform. It is therefore possible to achieve atomic resolution (see Figure 2-4).

In previous aluminum and tin experiments by Lai and Allen [6, 7], in-situ calorimetric measurements were first carried out. Nanocalorimeter sensors were taken out of the vacuum chamber, and then transfer on to a copper grid before TEM operation. The process is complex and rather difficult to handle. A piece of Kimberly paper was cut to nitride window size and placed on a glass slide. Deionized water was used to wet this paper. A copper grid was added on top. Then the calorimeter sensor was carefully placed on top of the copper grid with the sample area aligned to it. Once the membrane touches the wet surface, it breaks and will be sucked to the wet surface. However, this process is not very controllable. Membranes are often break before it attaching to the copper grid. The broken pieces naturally curl up. Finding an observable area where samples do not overlap becomes difficult. Therefore, in those old experiments, the sample area was usually wider than the nanocalorimeter heater to increase the chance for TEM imaging. This comprise adds 15~20 % of the uncertainty to the measurement because how far away small pieces of the sample to the heater will contribute to the nanocalorimetry is unknown. Moreover, the operation increases the possibility of contamination.

To solve the problem, TEM nanocalorimeters are first introduced during this work [8]. The schematic of the sensor has been shown in previous section (see Figure 2-1). TEM nanocalorimeters have many advantages. (1) The sensor can directly fit into TEM without further preparation, which means less contamination to the sample. (2) It is safe and convenient to handle, thus saves the time and sensors for the experimental load. (3) It provides a flat surface for TEM plane view observation in stead of a possible tilted sample due to curled membranes. (4) The sample is confined within the heater width by a

shadow mask with a special notch for TEM observation that is only ~2% of total sample.

(5) It is totally compatible with old generation nanocalorimeters [9].

Since the dimension of the new nanocalorimeter is physically limited by available space in side of the TEM, the sensor design has to have more considerations.

For a Philips CM12 microscope, the tip of a single tilt stage can be machined to receive a rectangular sample with a maximum width of 5mm. The more recent ones, JOEL 2010 series microscopes, however, are more flexible for samples up to 10mm or wider. The new microscope was not available when I did the design work, but it is good to make our sensor compatible to both of them. The TEM nanocalorimeters used in this work is 4.3 mm wide, while the length of the sensor is 11.2 mm. The membrane window is 2.3 mm by 7.8 mm. The metal strip (heater) is 0.5 mm wide and placed in the center of the window. The distance between the edge of the heater and the silicon frame is 0.9 mm, which is the same as nanocalorimeters used in Lai's work. This value (0.9 mm) probably is too big based on several experimental estimations from the heat-influenced regions. More works on both simulation and experimental observation have to be done in order to improve the situation. Such information, however, is not covered in this work.

The masks used to fabricate TEM nanocalorimeters are shown in Figure 2-5. On the window mask, the main rectangular features are for opening the silicon nitride window. The size of the rectangular should be slightly bigger than the actual nitride window by:

$$d = 2 \times t \times \tan \theta \quad (2.5)$$

where d is the additional length that should be considered due to the anisotropy in silicon etch, t is the wafer thickness (250 μm in this work) and θ is the angle between silicon

(100) and (111) plane (54.73°), respectively. The small square is for aligning patterns on both sides of the wafer.

Quite different from previous nanocalorimetry work. Special features that help wafer cleaving have been made on the mask. These features are critical for obtaining individual TEM nanocalorimeter sensors. The feature on the mask consists of two aligned lines: one is 7mm long and 0.175 mm wide; the other is 5mm long and 0.375 mm wide right on top. Due to the anisotropy characters of silicon wet etch, the 0.375 mm line will just etch through after KOH processing and 0.175 mm line will stop in the half way. The wet etching process removes outside corner faster than regular features, thus the final result is a line with smooth transition regions and sharp ends.

There are three sensors on the mask. They are exposed at the same time during pattern transfer. This is so-called one die in lithography. Totally seventeen dies can be transferred in one 3-inch wafer, but only thirteen dies are used in this work because the four dies on the edges of the wafer will weak the silicon frame, add difficulty in handling the wafer, and increase the chance of failure. The cleaving lines are overlapped between the dies so that thirty-nine identical sensors are arranged in the center of the wafer.

On the metallization mask, marks have been made for the convenience of finding cleaving line positions. Also, there is a special $100 \times 100 \mu\text{m}^2$ square that can be used as alignment mark, or the standard area for diffraction calibration.

Figure 2-6 is an example of a nanocalorimeter sensor loaded in a JOEL 2010 TEM single tilt stage. The tip holder is made of aluminum. The nanocalorimeter sensor slides into the holder and is clipped by a spring finger made from beryllium copper.

2.5 Several problems and discussion

Nanocalorimetry is still a new technique, with a lot of points not well understood yet. Main theory, sensor design, calibration, operation and thermal analyses have been summarized elsewhere [4, 10]. However, there are several interested phenomena that have been observed in recent experiments.

Nanocalorimeter is a unique MEMS sensor that relies on material property, i.e., the patterned metal strip is used as a resistive temperature sensor. The temperature coefficient of resistance (TCR) influences the sensitivity of the measurement. The TCR coefficient of the sensor is usually about 30~80% of the bulk, depending on the metals, batches, adhesion layers and the annealing history. High temperature evaporated metals are worse than low temperature ones. Such results imply that contamination during the metallization may be the main issue in this case. A comparison experiment has been carried out using aluminum as metallization layer in a clean chamber with better base pressure (10^{-8} torr). No adhesive layer was used and the deposition was done at $\sim 2\text{nm/s}$. The TCR of sensor is then very close to the bulk value. Impurities in the metal layer also increase the noise in electrical measurement. To further improve the nanocalorimetry measurement, a better metallization is of necessary.

In all of the nanocalorimetry observations, there are small extraneous signals at specific temperature ranges. This extraneous signal can attenuate the caloric results at nearby temperature. Typically platinum sensors have this effect at $\sim 220\text{ }^\circ\text{C}$; $320\text{ }^\circ\text{C}$ for aluminum and $>500\text{ }^\circ\text{C}$ for gold sensors. It depends more on the metallization rather than the batch of the sensor. A simple explanation is impurity phase transformation since most of the sensor has an adhesion layer and interface of the metallization is complex.

Pure aluminum sensors, however, behave the same as aluminum sensors with the titanium adhesion layer. Moreover, the effect shifts to lower temperature when the sensor is cooled, while the melting temperature should not be sensitive to the initial status of the sensor (indium and tin experiments for examples). Therefore, the phase transition probably is not the reason, or, at least not the main reason for such observations.

On the other hand, soft materials (aluminum and gold) tend to have this influence at higher temperatures than hard materials like platinum. Then, the stress on the membrane sensor becomes more suspicious. It has been known that traditional thin film resistive temperature sensors suffer from poor reproducibility caused by sensitivity to strain that inevitably accompanies sensitivity to temperature. Nanocalorimeters are membrane devices based on thin nitride and patterned metal layers. Both layers can easily deform to release the stress. In such cases, reproducibility is not the problem, which can be proved from regular drift tests. However, it is still reasonable to assume that stress is the cause of this small extraneous effect, since the difference in thermal expansion coefficients is not small and the temperature change is large. If this is true, there probably has no good solution to solve the problem. To compromise, one can select different sensor metallizations for different research interests.

Shunting is another problem occurred during the nanocalorimeter sensor calibration, where sensor resistance is measured using the four-point method at elevated temperatures. However, the resistance between the metal layer and silicon frame is not infinite. Equivalently the sensor and the silicon frame are measured in parallel. Thus the measured resistance is smaller than the true sensor resistance. The influence is not obvious at room temperature, but will shunt the sensor when the silicon becomes

conductive at elevated temperatures. One possible reason is that the metal layer touches the silicon frame edges during the wafer cleaving because metal thin films are usually more ductile than silicon. This explanation is rejected by more accurate cleaving technique introduced in this work, i.e., all the metal patterns are physically isolated from the edge of the sensor. The situation is not improved. Another explanation attributes the shunting effect to the pin-holes through the nitride membrane. Silicon nitride membranes are under dense and have nano-channels. These channels are filled during metallization to form the metal/silicon contact. If this is the case, a thicker insulation layer will finally solve the problem. In fact, an additional insulation layer does help. However, this is not the main reason after tracking information from different sensors. The results become more obvious when using a new calibration stage that can have two sensors in one calibration run. One position is always better than the other one in terms of the resistance between metal and silicon nitride. Moreover, this monitored resistance can change discontinuously during the heating. Therefore, the shunting effect is probably caused by the mechanical damage from loading the contact probes but not the first two hypotheses. A thicker insulation layer performs better for the same type of force. Thus the further improvement should be focused on making either a better contact or a more robust insulation layer.

Understanding a nanocalorimeter is quite a long process. There are many steps in both sensor fabrication and experimental operation. Carefully in each step is essentially important. A good quality sensor is the first step for one to have much cleaner experimental results, and usually less time, labor and cost.

2.6 References

1. Hemminger, W., *Grundlagen der Kalorimetrie. English*, ed. Y. Goldman. 1984: Weiheim; Deerfield Beach, FLa. :Verlag Chemie.
2. Berry, R.S., *Thermodynamics: Size is everything*. Nature, 1998. **393**: p. 212.
3. Lai, S.L., Ramanath, G., Allen, L. H., Infante, P., Ma, Z., *High-speed (10^4 degrees C/s) scanning microcalorimetry with monolayer sensitivity (J/m^2)*. Applied Physics Letters, 1995. **67**(9): p. 1229-31.
4. Efremov, M.Y., Olson, E. A., Zhang, M., Zhang, Lai, S. L., Schiettekatte, F., Z. S., Allen, L. H., *Thin-Film Differential Scanning Nanocalorimetry: Heat Capacity Analysis*. Thermochemica Acta, 2003: p. submitted.
5. Kovacs, G.T.A., *Micromachined Transducers Sourcebook*. 1998, Burr Ridge, IL: WCB/McGraw-Hill. 37.
6. Lai, S.L., Carlsson, J. R. A., Allen, L. H., *Melting point depression of Al clusters generated during the early stages of film growth: nanocalorimetry measurements*. Applied Physics Letters, 1998. **72**(9): p. 1098-100.
7. Lai, S.L., Guo, J. Y., Petrova, V., Ramanath, G., Allen, L. H., *Size-dependent melting properties of small tin particles: nanocalorimetric measurements*. Physical Review Letters, 1996. **77**(1): p. 99-102.
8. Zhang, M., Efremov, M. Yu., Schiettekatte, F., Olson, E. A., Kwan, A. T., Lai, S. L., Wisleder, T., Greene, J. E., Allen, L. H., *Size-dependent melting point depression of nanostructures: Nanocalorimetric measurements*. Physical Review B, 2000. **62**(15): p. 10548-10557.
9. Lai, S.L., Ramanath, A. G., Allen, L. H., Infante, P., *Heat capacity measurements of Sn nanostructures using a thin-film differential scanning calorimeter with 0.2 nJ sensitivity*. Applied Physics Letters, 1997. **70**(1): p. 43-5.
10. Olson, E.A., Efremov, M. Yu., Zhang, M., Zhang, Z. S. Allen, L. H., *The design and operation of a MEMS differential scanning nanocalorimeter for high-speed heat capacity measurements of ultrathin films*. Journal of Microelectromechanical Systems, 2003. **12**(3): p. 355-64.

2.7 Figures

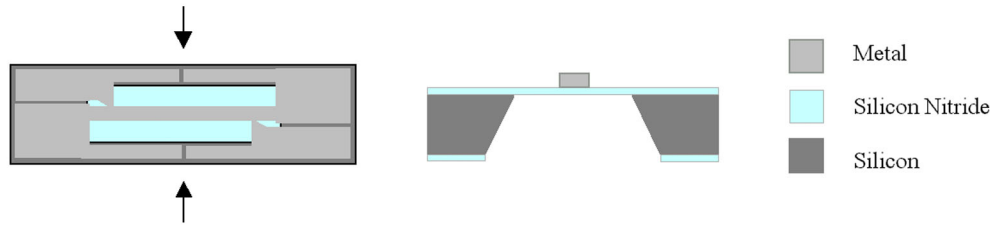


Figure 2-1. Planar and cross-sectional configurations of a nanocalorimeter sensor developed during this work. The sensor consists a 35~50 nm thick amorphous silicon nitride membrane supported on a silicon frame, and a 50 nm thick patterned metal layer.

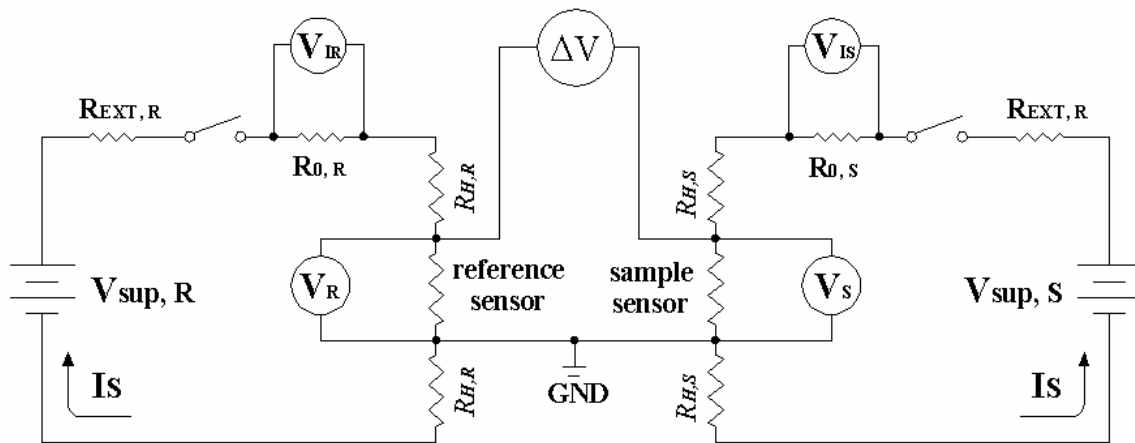


Figure 2-2. The principle circuitry of the differential scanning nanocalorimetry: two identical sensors are used — the sample sensor contains the interested material, and a reference sensor with no sample. DC current pulses through the sensors are precisely synchronized. Five electrical measurements are taken simultaneously: currents through sample and reference I_S and I_R ; voltages across sample and reference V_S and V_R ; and the differential signal ΔV , which reflects the difference between the two sensors due to the presence of the sample.

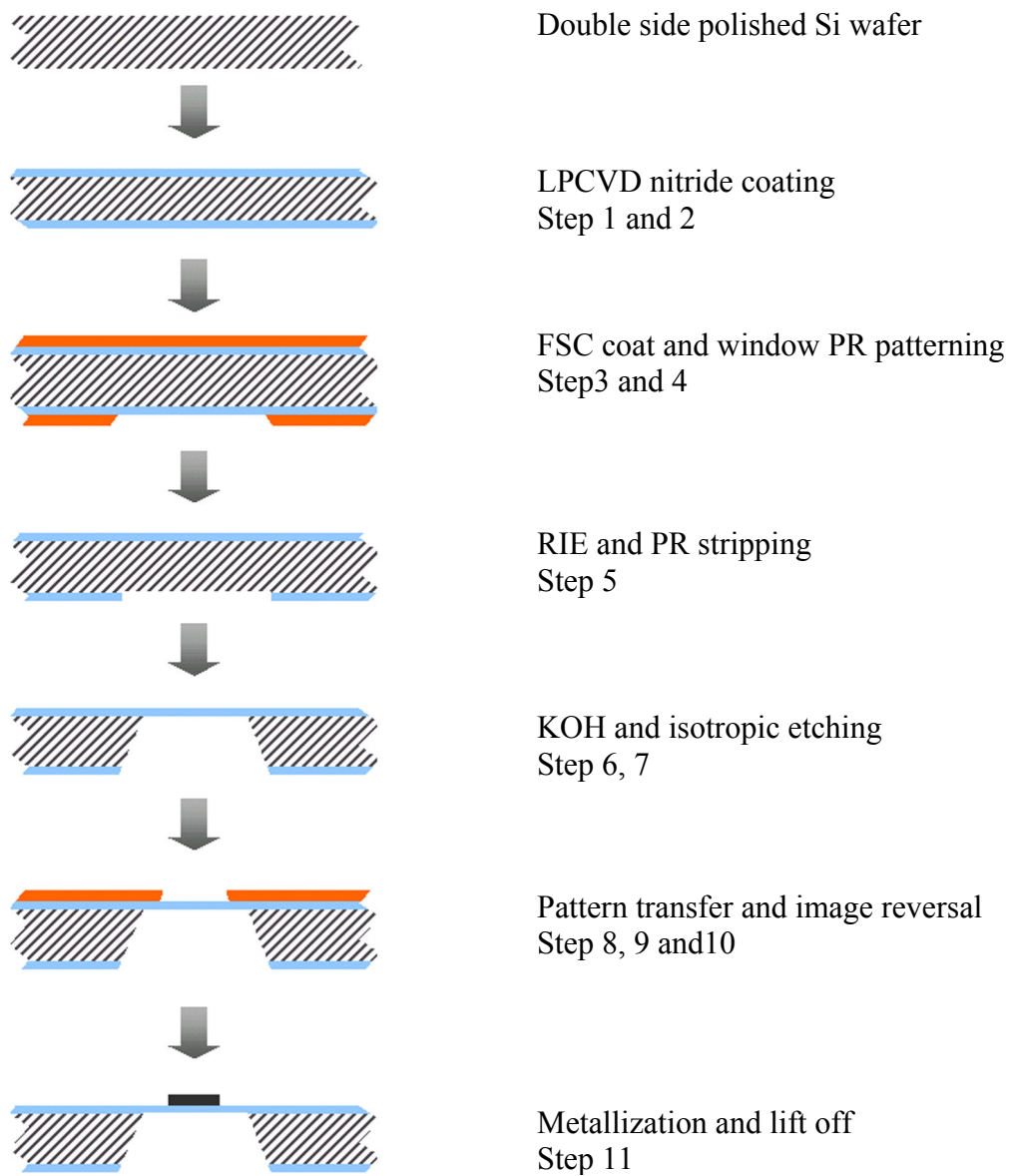


Figure 2-3. An illustration of the nanocalorimeter sensor fabrication: the process can be summarized as follows: (1) to use PR as a mask to etch silicon nitride; (2) to use nitride as a mask to etch silicon; (3) to pattern metal layer on the membrane.

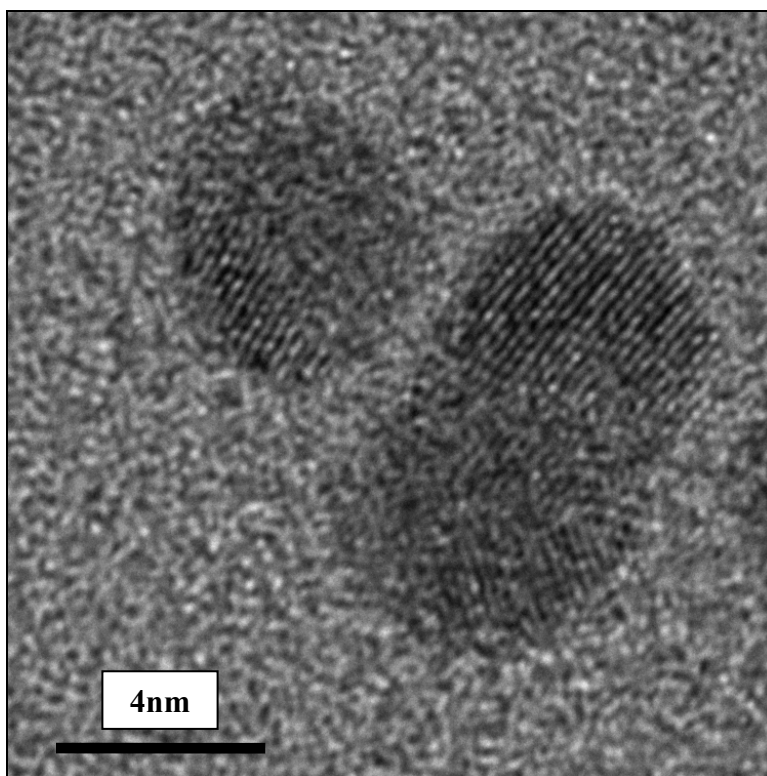


Figure 2-4. Example of a high-resolution TEM image of annealed gold nano particles on a TEM nanocalorimeter sensor.

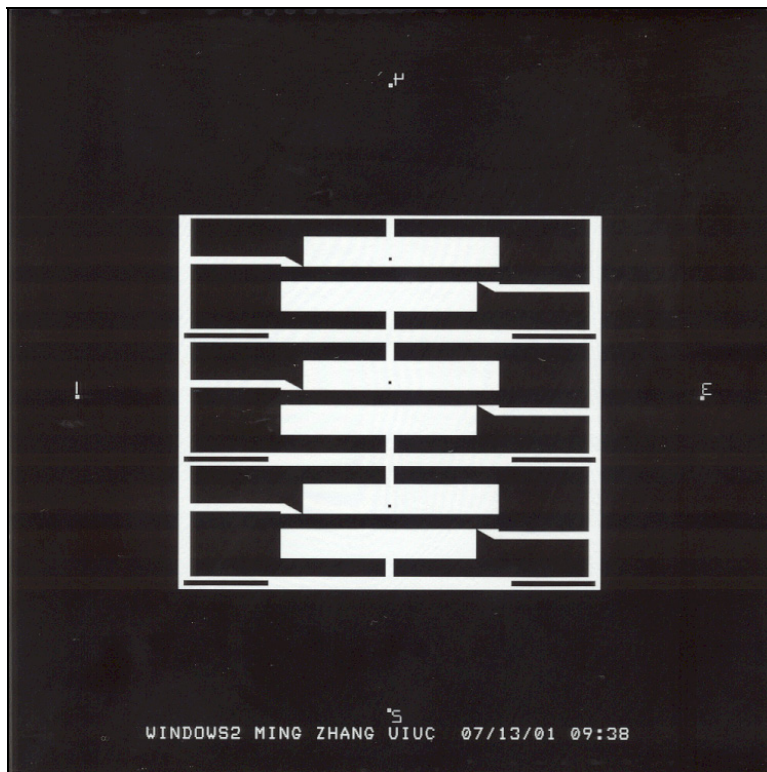
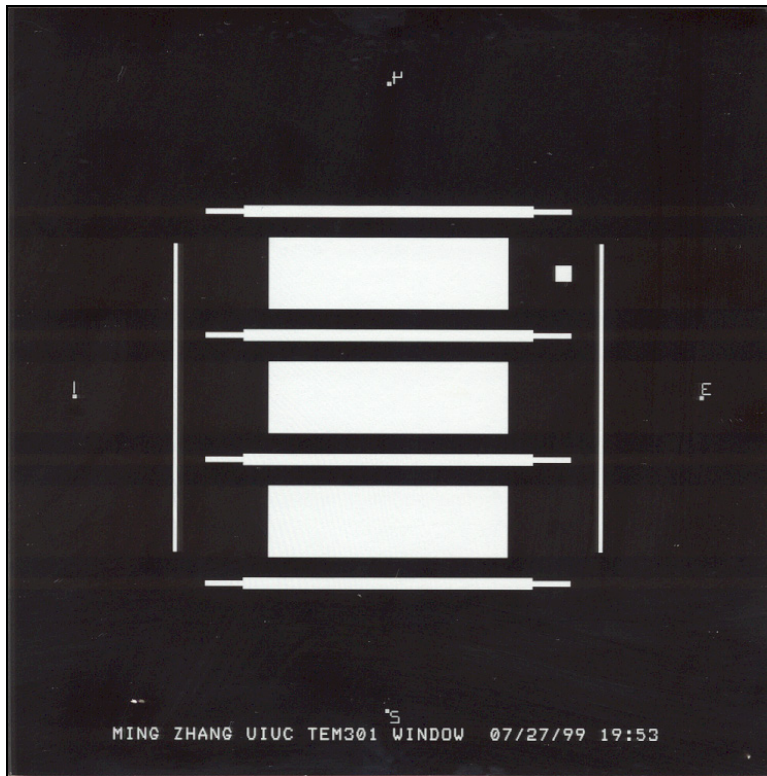


Figure 2-5. Masks for TEM nanocalorimeter sensor fabrication. The top one is for opening the nitride windows; the bottom one is for the metallization.



Figure 2-6. An example of a nanocalorimeter sensor loaded in a JOEL 2010 TEM single tilt stage. The tip holder is made of aluminum. The nanocalorimeter sensor slides into the holder and is clipped by a spring finger made from beryllium copper.

CHAPTER 3

SIZE-DEPENDENT NANO-STRUCTURE MELTING

The melting behavior of 0.1 ~ 10 nm thick discontinuous indium films formed by evaporation on amorphous silicon nitride has been investigated by an ultrasensitive nanocalorimetry technique. The films consist of ensembles of nanostructures for which the size dependence of the melting temperature and latent heat of fusion are determined. The relationship between nanostructure radius and the corresponding melting point and latent heat is deduced solely from experimental results (i.e., with no assumed model) by comparing the calorimetric measurements to the particle size distributions obtained by transmission electron microscopy. It is shown that the melting point of the investigated indium nanostructures decreases as much as 110 K for particles with a radius of 2 nm. The experimental results are discussed in terms of the existing melting point depression models. Excellent agreement with the Homogeneous Melting Model is observed.

3.1 Introduction

The physical properties of materials with reduced dimensions draw considerable attention because of the technological and fundamental importance of the problem [1, 2]. Nowhere is the interest greater in the thermodynamics of materials at small dimensions than in the microelectronics industry, where transistors and metal-interconnects will have tolerances of only several nanometers by the year 2005. One particular phenomenon of interest is the size-dependent melting point depression — small particles have a lower melting point than bulk material [3-5]. This results from the increasingly important role of the surface as the size of the

structure decreases. From an atomistic point of view, as the size of the nanostructures decreases an increased proportion of atoms occupies surface or interfacial sites. These atoms are more loosely bound than bulk atoms, which facilitates the melting of the nanostructure. However, the mechanism by which nanostructures melt is not fully understood. In order to develop a better understanding of the phenomenon more experimental information is warranted, especially with regard to the energy associated with the melting process.

Melting point depression in nanostructures was first observed using transmission electron microscopy (TEM) [3, 6-8]. Using this technique the melting temperature of nanostructures is monitored by the loss of crystalline structure of the nanostructures with increasing temperature. It can also be used, as we do in this work, to measure the size of the nanostructures directly. However, high-energy beam-sample interactions may influence the melting process. Similarly, x-ray diffraction has also been used for melting point depression studies [9, 10]. The difficulty in using this method is the determination of the particle size distribution, especially for the smaller particles.

Calorimetry is another extremely powerful technique for investigations of melting phenomenon. Using calorimetry we directly measure the heat capacity and the latent heat of fusion as a function of the temperature. The technique has undergone major improvements in recent years. Calorimetry adds a unique dimension to melting point studies. In addition to obtaining melting point information we also obtain values for the energy involved in the melting process. There are many types of calorimetric methods. Experiments with metal filled porous substances [11], particles dispersed in oil [12] and particles embedded in a metal matrix [13, 14] used conventional calorimetry, but the melting behavior in such cases must strongly depend on the type of surrounding material, i.e. on the environment of the nanostructures [14, 15]. Also, a

sophisticated technique based on laser irradiation of free metal clusters produces calorimetric data which are not affected by substrate influence [16, 17]. To date, this technique has been applied only for very small single clusters (compatible with mass-spectrometry) [16].

Recently, an ultrasensitive method, Thin-film Differential Scanning Calorimetry (TDSC) [18-21], was developed to measure the thermal processes occurring in samples deposited on a surface. In this article, the TDSC method is used to observe the melting behavior of small indium nanostructured ensembles (indium and its alloys are important materials in the microelectronics area, specifically in flip-chip packaging technology [22]). The limits of the measurement have been pushed to sizes never before reached. We demonstrate that the melting point depression and latent heat of fusion of such nanostructures decreases proportionally to the reciprocal radius r^{-1} for radii down to 2nm.

3.2 Melting models

There are many excellent approaches for theoretical studies of melting phenomenon in small particles, including classical thermodynamic as well as modern simulation methods [5, 23]. For convenience in describing our experimental work, in this chapter we will use the classical thermodynamic description of melting. A theory based on Laplace equation of the surface and Gibbs-Duhem equation [24] predicts a melting temperature depression of the form [9]:

$$\Delta T = T_m^{bulk} - T_m(r) \approx \frac{2T_m^{bulk}}{H_m^{bulk}} \frac{\alpha}{\rho_s r}, \quad (3-1)$$

where T_m^{bulk} , H_m^{bulk} and ρ_s are the bulk melting temperature, the bulk latent heat of fusion, and the solid phase density, respectively. r represents the radius of a spherical particle, and α is a parameter related to the interfacial tension between the solid phase and its environment. Up to

now, three main melting mechanisms have been considered to describe the relation between the melting temperature and the size of particles, resulting in different expressions for α :

- i) The homogeneous melting and growth model (HGM) [6, 25], which considers equilibrium between entirely solid and entirely melted particles and expresses α as:

$$\alpha_{HGM} = \sigma_{sv} - \sigma_{lv} \left(\rho_s / \rho_l \right)^{2/3}, \quad (3-2)$$

- ii) The liquid shell model (LSM) [6, 26, 27], which differs from HGM by assuming the presence of a liquid layer of thickness r_0 in equilibrium at the surface of solid particle; this model sets

$$\alpha_{LSM} = \frac{\sigma_{sl}}{1 - \frac{r_0}{r}} + \sigma_{lv} \left(1 - \frac{\rho_s}{\rho_l} \right), \quad (3-3)$$

- iii) The liquid nucleation and growth model (LNG) [28-31], based on the kinetic consideration that melting starts by the nucleation of liquid layer at the surface and moves into the solid as a slow process with definite activation energy, and for which

$$\sigma_{sl} < \alpha_{LNG} < \frac{3}{2} \left(\sigma_{sv} - \sigma_{lv} \frac{\rho_s}{\rho_l} \right). \quad (3-4)$$

Here σ represents the interfacial tension between solid, liquid and vapor phases (indexes s, l, and v, respectively), and ρ_l is the density of the liquid phase. In addition, it is worth mentioning that Eq. (3-1) is actually a first order expansion. However, the 2nd order term [32] is small in the present case since it represents a correction of +5 K at $r = 2$ nm.

These models are related to the different proposed melting mechanisms of the nanostructures. Verifying the applicability of these models by the experimental data (without presupposing any model in the data analysis) allows us to draw conclusions about the melting mechanism of indium particles.

3.3 Experimental procedure

The TDSC method relies on microfabricated calorimetric sensors. The planar and cross-sectional configurations of the TDSC system are shown in Figure 3-1. These sensors consist of extremely thin (30nm) amorphous silicon nitride membrane ($a\text{-SiN}_x$) supported by a silicon frame. The mass addenda of the sensor being so small, the achieved sensitivity is comparable to the latent heat of fusion of 1/1000 of a monolayer of bulk indium.

On one side of the membrane, a patterned thin (50nm) nickel strip is deposited, which is used simultaneously as a heater and resistive thermometer during the experiments. Differential calorimetry is achieved by using two identical sensors in one setup — a sample sensor (with material deposited on the sensor) and reference sensor (with no material). Before the experiment, the resistivity of both sensors is calibrated against the temperature in a three-zone tube vacuum furnace.

The calorimetric measurement is initiated by applying a synchronized dc electrical pulse to each nickel heater. The temperature of the sensors increases by Joule heating. High heating rates (from 10^4 to 10^6 K/s) allow the measurements to approach adiabatic conditions. The current and voltage through the sensors are measured for power and resistivity (and temperature) calculations.

In the ideal case where we would have two identical sensors with temperatures increasing exactly at the same rate, the power required to melt the sample deposited on the sample calorimeter would simply be

$$P(t) = V_S I_S - V_R I_R \quad (3-5)$$

where V and I denote the voltages and currents through the sample and reference (indexes S and R, respectively) sensors, and t is time. The heat capacity would then be

$$C_p(T) = \frac{P(t)}{dT/dt}. \quad (3-6)$$

where T is the sample temperature at time t . However, several corrections have to be taken into account. First, an independent measurement of V and I for the sample and reference leads to somewhat noisy measurements. A differential measurement of the voltage across the reference and sample sensors improves drastically the signal-to-noise ratio, and is the key element that allows us to reach high sensitivity. Second, the characteristics of the sensors in any couple are not absolutely identical. In order to correct this disparity, the difference in heat capacity between the sample and reference cells is measured as a function of temperature before the experiments. Such relations are used in the final calculations. Corrections also take into account the influence of the deposited sample mass on the heating rate of the sample sensor. Third, the same $C_p(T)$ measurements are carried out at different heating rates, and used for later calculations of heat loss correction (i.e., departure from adiabatic conditions).

For the present experiments, thin indium layers with different thicknesses have been investigated. We selected indium due to its low melting point ($T_m^{bulk} = 156.60$ °C) [33] and low affinity with SiN_x . Moreover, indium has frequently been for investigations of melting phenomena in small particles [6, 7, 11, 13, 14, 30, 34]. The first stages of the deposition result in a discontinued film on the sensor membrane, consisting of nanoparticles of various sizes [35]. Below 100 nm of equivalent indium thickness, the average size of the particles increases almost linearly with the quantity of metal deposited.

For each experiment, both sensors are placed together in a standard evaporator with a base pressure of about 10^{-8} Torr. Before the deposition, the sensors are heated in order to remove

any potential contamination of the surface. A shadow mask is placed in line with the nickel strip as illustrated in Figure 3-1. Pure indium (Alfa Aesar 99.9985%) is then evaporated onto the sample sensor to nominal thicknesses ranging from 0.1 nm to 10 nm. The thickness of the different layers is monitored by an *in situ* quartz microbalance and corroborated afterwards by the mass obtained from the heat capacity measurements. The deposition rate is ranged from 0.02 to 0.04 nm/s.

Beginning within a few seconds following the indium deposition, 100 calorimeter measurement/scans are taken sequentially at 1 second intervals. During each scan the temperature of the nanostructures as well as the calorimeter is raised from ambient temperatures to 300°C. Consequently the nanostructures are annealed during each scan. However, the effect of annealing, which are associated with minor changes in the particle size distribution (TEM) and Cp data, are limited mostly to the first scan and will be the focus of our future work. The calorimetry data presented in this work represents the average of all 100 scans excluding the first ten scans. The scans are identical within the measurement error, and are averaged in order to increase the sensitivity of the system. The TEM and calorimetry data presented here represent the results of fully annealed indium particles.

After the calorimetric measurement, the sample sensor is transferred *ex situ* into a Phillips CM-12 TEM without additional preparation. Bright field micrographs of the sample sensor are taken. The particle-size distributions corresponding to each calorimetric experiment are obtained from digitized images using a combination of distance transformation and blob analysis algorithms [36]. Several thousand particles were measured in each sample in order to achieve sufficient statistics.

Oxidation of indium nanostructures occurs during the transfer of sample from the deposition/calorimetry chamber to the TEM system. Particles with a radius of less than 3 nm are completely oxidized while those nanostructures with a radius larger than 3 nm have an “oxide-shell” of 3-nm thickness [34]. We correct for the increase in particle size due to oxidation by recalculating the particle-size distribution obtained from the TEM micrographs. By taking into account the change in volume (24% in volume or 7% change in radius) due to the oxidation process we reduce the size of each particle in the distribution by the appropriate amount. For example an indium nanoparticle with radius of 3.0 nm will be totally oxidized during the transfer, and will have a final radius of 3.2 nm. From a practical stand point, the oxidation effect has little impact on the over all analysis, since the maximum difference between the radius of a completely oxidized and unoxidized 3.0 nm particle is only 0.2 nm, which is about the level of uncertainty of our TEM and image analysis techniques.

We note that particles smaller than ~1 nm were not distinguishable from the small features in the SiN_x membrane. However, such small particles should not contribute significantly to the melting heat unless they are present in huge proportions. Finally, the relation between the melting point and the particle size is extracted from the correspondence between the calorimetric data and the particle size distributions, as described in section 3.4.2.

3.4 Result and discussion

3.4.1 Effects of the melting point depression on TDSC measurements

Figure 3-2 shows the heat capacity [$C_P(T)$] measurements for indium films with thickness ranging from 1.3 to 11.0 nm. These curves have been normalized, i.e., divided by the film area S and the amount of mass deposited, from 0.4 ng (1.3 nm) to 3.3 ng (11.0 nm). The baseline of all

the curves corresponds to the heat capacity of bulk indium at higher temperatures. This corroborates the amount of indium measured by the quartz microbalance during the deposition. As a result, this shows that the calorimeter can be used to precisely measure small masses of material precisely.

The peak in each $C_p(T)$ measurements represents the heat involved in the melting process as a function of the temperature. Figure 3-2 demonstrates a significant low-temperature shift in melting peak and peak broadening as the film thickness decreases. These effects are reported on the inset of Figure 3-2, which shows the position of the peaks and their Full Width at Half Maximum (FWHM) as a function of the indium film thickness. This is the result of the decreasing size of the particles with decreasing deposited amount of indium.

The TEM micrographs on Figure 3-3 show that the indium film is discontinuous and consists of individual nanometer-size particles. The smaller particles correspond with the thinner film, as clearly shown by the corresponding particle size distributions. The particle distribution histograms, hereafter denoted as $h(r)$, represent the particle surface density as a function of the radius [i.e. (particles/nm²)/nm]. In Figure 3-3 and the subsequent figures, $h(r)$ has been multiplied by the volume of the particles ($4\pi r^3/3$) so it reflects in a more sensible way the participation of the particles to the melting peak, since they should contribute to the heat of melting proportionally to their volume, or mass, at least in a first approximation.

On these histograms it is shown that average size of particles decreases with the film thickness. Since their temperature of melting decreases accordingly, following Eq. (3-1), their contribution to the melting peak is shifted towards lower temperature. The broadening of the peak is the result of the non-linear ($1/r$) relation between the size of the nanostructures and their melting point. The same spread in the particle size distribution corresponds to a much larger

width in the $C_p(T)$ curve for smaller particles than for larger ones. It is thus clear that a relation between the size of the nanostructures and their melting temperature can be extracted from such measurements.

Another important feature of calorimetric techniques is that they simultaneously measure the latent heat of fusion of the melting particles. This is important since the size can also influence this parameter. The proportion of atoms occupying surface sites in a spherical particle will increase proportionally to the reciprocal radius ($1/r$), at least in a first approximation. Such atoms being more loosely bounded, they should require less heat in order to melt, so we also expect the latent heat of fusion to decrease with particle size.

The value of the heat of fusion H_m can be determined from the $C_p(T)$ curves as the area under the melting peak. The melting peak component of the $C_p(T)$ measurements shown in Figure 3-2, as well as those of other experiments, have been integrated over the temperature in order to measure the heat of melting as a function of film thickness. This result is shown in Figure 3-4, in comparison to the expected value if all particles were melting with the bulk latent heat of melting (solid line). While the correspondence is very good for larger thicknesses, it is seen that the heat of melting is significantly offset for the smaller particles. This difference can be due in part to a size-related depression of the latent heat, but also to possible existence of some forms of deposited indium which do not contribute to the melting process under the described experimental conditions. Such forms can include already melted particles, adatoms, liquid layer on the surface of particles, interface layer between particles and membrane, etc.

3.4.2 Size-dependent effects

This section describes how the influence of the size on the melting point and heat are determined for indium nanostructures. The interconnection between the $C_P(T)$ plots, obtained from calorimetry, and particle size distribution $h(r)$, observed by microscopy, is based on the fact that particles with different sizes melt differently. The relationship between those two measurements is based on i) the particle size dependence of the melting temperature and ii) the relation between the size and the latent heat of fusion. These two phenomena are tightly intertwined in the measured signals. Our objective here is to de-couple and reveal these two effects without using any *a priori* insight or model for their size dependence.

Only two general assumptions will be used. First, the melting temperature increases with size (i.e., particles with larger radius melt at higher temperatures). Second, each particle melts instantly (at one certain temperature). These suppositions are very common. The first hypothesis is based on extensive experimental literature on melting small particles on free surfaces. The only exception is for very small clusters [16, 17], which show irregular variations of the melting point. The second assumption is used explicitly in HGM [6] and LSM [6] models and obtained as experimental fact in LNG model considerations [30].

3.4.2.1 Size dependence of the melting point

The main idea of extraction of a model-free correspondence between melting temperature and particle radius from TEM and calorimetric data is straightforward. A direct relationship is established by mapping (i.e., integrating concurrently) the area under the particle-size distributions and the melting peak of the corresponding $C_P(T)$ measurements. This integration procedure will be described below. However, before we enter into the details of this calculation,

it must be established that both the size distribution histograms and melting peak plots are incomplete in the lower part of their abscissa. While the maximum melting temperature, near T_m^{bulk} , is properly measured, as well as the largest particle sizes in each film, the particles with a radius less than about 1 nm cannot be distinguished from the SiN_x membrane features on TEM micrographs. So this part of the histograms is unreliably determined. At the same time, a part of the melting peak, for temperatures below the present working temperature range of calorimeter, cannot be measured. This will obviously affect principally the thinnest films.

In order to find the section of the size distributions that corresponds to the measured part of the melting peak, we therefore need to calculate a particle radius R_L that corresponds to our lower measurable melting temperature T_L . Then, the particle distribution from R_L up to its maximal radius (which is easily can be found from the TEM images) can be mapped with melting peak in the temperature range from T_L up to its maximal temperature. The following procedure has been used to calculate the value of R_L . Although the working temperature range of our TDSC begins at room temperature, the reliable $C_p(T)$ measurements are available only above 40 °C due to transient effects at the beginning of the heating pulse. It is thus convenient to use this temperature as T_L (i.e., $T_L=40$ °C).

The $C_p(T)$ curves and the particle radius distributions of the smallest deposited thicknesses are compared in Figure 3-5. For the 0.4 nm indium deposition, most of the melting peak is visible, and a large fraction of the indium mass is contained in the particles larger than 2 nm in radius. Also, the 0.2 nm experiment reveals barely the half of the melting peak in the $C_p(T)$ data. On the other hand, there is no observable melting peak in the 0.1 nm $C_p(T)$ measurement, for which all particles are smaller than 1.75 nm in radius. After comparing the particle distribution with the heat capacity data for the thinnest films (0.1-0.4 nm) we conclude

that the most reasonable estimation of $R_L = 1.85 \pm 0.1$ nm. Henceforth for all further analysis of melting point determination, only particles with radius larger than R_L will be considered to contribute to the melting heat above T_L .

This being established, the next step is to relate the specific melting point $T_m(r)$ to a specific particle size. This is achieved by *mapping* the integral heat involved during the melting [from the $C_p(T)$ measurements] with the corresponding TEM particle distribution $h(r)$ (for $r > R_L$) for each deposition cycle. This mapping process is shown schematically in Figure 3-6.

The first step is to “normalize” the calorimetry and TEM data so that the heat generated by a specific set of particles is equal to the heat measured by the calorimeter. In doing so we define the average heat of fusion H_m^{TEM} for the specific deposited thickness to be as follows:

$$H_m^{TEM} = \frac{\int_{T_L}^{T_m} (C_p(T) - C_p^0) dT}{S \int_{R_L}^{\infty} \frac{4}{3} \pi r^3 \rho_s h(r) dr}, \quad (3-7)$$

where C_p^0 is the base line under the melting peak in the $C_p(T)$ measurement and corresponds to the heat capacity, ρ_s is the bulk solid phase specific density and S is the area of the indium film. Although it is necessary for us to define the heat of fusion in this way in order to relate the particle size and melting point directly, another method to estimate the dependency of the heat of fusion H_m on particle size will be discussed in section 3.4.2.2.

The calculation of the mapping proceeds as follows. In order to determine the melting temperature $T_m(r)$ for a particle of radius r we integrate the equivalent heat of melting for all particles with radius $r > r'$ [the shaded area under the curve in Figure 3-6(a)] as given by the integral

$$H_m^{TEM} \times S \int_{r'}^{\infty} \frac{4}{3} \pi r^3 \rho_s h(r) dr . \quad (3-8)$$

We then match this amount of heat with that measured with the calorimeter (the shaded area under the curve in Figure 3-6(b) as given by Eq. (3-8). This is done by selecting the appropriate value for the lower limit of the following integral:

$$\int_{T_m(r')}^{T_m^{bulk}} [C_p(T) - C_p^0] dT . \quad (3-9)$$

For a given value of r' there is a unique value of $T_m(r')$ which satisfies the criterion. Obviously, because of the definition of H_m^{TEM} (Eq. 3-7), at $r'=R_L$ we find $T_m(r)=T_L$. This technique is repeated sequentially for the entire range of particle size starting from the largest particle to the minimum size particle with the constraint that $r' > R_L$.

The mapping process is done separately for each deposited thickness, each yielding a unique experimental set of values for $T_m(r)$. The results of the analysis are shown in Figure 3-7(a). Several depositions have been performed with various amounts of material. Since there is some overlap in the particle distributions between the deposited thicknesses we can obtain an average value for $T_m(r)$. Such average $T_m(r)$ relations are calculated and plotted in Figure 3-7(b), and are found to be remarkably linear over a wide range down to nanometer sizes.

Such “classical” behavior is predicted by the HGM model. To illustrate this point, a simple straight-line relation, identified as a thick solid line in Figure 3-7(b), has been fitted to the averaged data. The slope of this relation is -220 ± 10 nm K, which corresponds to $\alpha = 53 \pm 3$ mJ/m² in Eq. (3-1). A theoretical value of α can be calculated for the HGM from Eq. (3-2) using values denoted in Table 3-1. The result, $\alpha_{HGM} = 43 \pm 10$ mJ/m², is in fairly good agreement with the experimental value (also see Table 3-2).

Our results do not exclude the LSM model, but impose a serious limit on the thickness of the liquid shell r_0 . The dashed line on Figure 3-7(b) represents a fit of the LSM to the unaveraged data, giving $r_0 = 0.3$ nm and $\sigma_{sl} = 63$ mJ/m² $\approx \sigma_{sv} - \sigma_{lv}$ as it should be near melting temperature [9]. The maximum acceptable value for r_0 so that the LSM model stays within the experimental uncertainty is $r_0 = 0.5$ nm, which represents the thickness of two atomic monolayers. This is in interesting agreement with the results of Molenbroek *et al.* [37] on bulk <110> indium, who observed a strong relaxation effect in the two first monolayers of this material. Our data also fall in the limit range predicted by the LNG model. Nevertheless, no physical evidence allows us to state if the structures or phenomena from which result the additional parameters in LSM (r_0) and LNG models are actual or not. For this reason, the simplest HGM model, which can be described in terms of some well-known independent characteristics of the material (σ_{sv} , σ_{lv} , ρ_s , and ρ_l), is preferred.

Finally, the slight “S” shape denoted in some of the individual $T(r)$ relations in Figure 3-7(a) could be the result of the widening of the melting peaks by the temperature resolution function of the calorimeters (FWHM~4 K); but some real effects could also be responsible for such features.

3.4.2.2 Size dependence of the latent heat of fusion

Now that the relation between the melting temperature and the size of the particles has been extracted from the C_p measurements, the next step is to look at the relation between the heat of fusion and the radius. The specific heat of fusion H_m is calculated by dividing the heat involved in the melting process by the mass of the sample. In one case, the mass of the sample

can be evaluated from the volume of the particles measured from the TEM micrograph. This type of calculation leads to the value H_m^{TEM} used in section 3.4.2.1.

However, such volume estimate is influenced by several parameters, namely the shape of the particle. TEM only allows a two-dimensional projection measurement of the particles, which may not be complete spheres. In fact, a noticeable departure of about 25% is found between the volume measured by TEM and the expected deposited thickness. For the indium films in the range 0.2-5nm particles can be viewed as incomplete spheres with a volume shape factor $Q = 0.75 \pm 0.1$ (i.e., the actual volume of the particles is about 75% of the what it would be if they were complete spheres with the radius measured by TEM).

On the other hand, the mass can be deduced directly from the baseline in the $C_p(T)$ measurement, using the bulk specific heat capacity. In this case, a self-consistent estimate of the specific heat of fusion can be found,

$$H_m^C = \frac{\int_{T_L}^{T_m^{bulk}} (C_p(T) - C_p^0) dT}{C_p^0 / c_p \cdot F}, \quad (3-10)$$

where F is a correction factor discussed below and C_p^0 / c_p is the mass found from the ratio between the measured baseline heat capacity (C_p^0 in J/K) and the specific heat capacity from the literature (c_p in J/g K) [38]. However, this ratio constitutes a measurement of the total mass. As demonstrated in section 3.4.2.1, the melting peak is incomplete for many experiments, especially for the smaller thicknesses, since the particles smaller than R_L do not contribute to the melting above T_L . For better approximation, only the fraction F of the total mass actually melting has to be taken into account. F can be estimated using the histograms $h(r)$ as the volume fraction of particles with a radius above R_L over the total volume measured by TEM.

However, inasmuch as TEM has limited resolution, and could not detect a large number of very small particles, only an upper limit estimation of F is available. Thus H_m^C constitutes a lower limit estimation of the specific heat of fusion.

The results of the calculation of Eq. (3-10) for each experiment are presented in Figure 3-8. The horizontal lines represent the radius range to which this calculation applies, considering the spread of the particles distribution in each case. While H_m^C value tends very well to the bulk latent heat of fusion for large particles ($1/r \rightarrow 0$), it clearly shows a depression as the particle size decreases.

While we have to keep in mind that this calculation constitutes a lower estimate, from an atomistic point of view, this depression corresponds to the heat necessary to melt approximately the first two atomic monolayers of the particles. In some sense, this would indicate that the atoms of the first outer two monolayers of the indium particles are in a relaxed, liquid-like state and do not contribute to the melting process. This conclusion is similar to that deduced from the maximum acceptable value of r_0 in the LSM discussed in 3.4.2.1.

The latent heat of fusion is expected to be size dependent from theoretical considerations [11]. A more rigorous treatment using Hess's law [39] and illustrated by the thermal chemical cycle of Figure 3-9 allows us to estimate the latent heat of fusion depression from a classical thermodynamics point of view:

$$H_m(r) = H_m^{bulk} - \frac{3}{r} \left(\frac{\sigma_{sv}}{\rho_s} - \frac{\sigma_{lv}}{\rho_l} \right) - \int_{T_m(r)}^{T_m^{bulk}} [c_{P,liquid}(T) - c_{P,solid}(T)] dT \quad (3-11)$$

The size-dependent heat of fusion $H_m(r)$ is represented as a dotted line in Figure 3-8. The model is in fairly good agreement with our data. The difference can be justified in terms of an underestimate of both H_m^C [Eq. 3-10] and σ_{sv} [in Eq. 3-11].

3.5 Conclusion

Using ultrasensitive thin-film differential scanning calorimetry in combination with *ex situ* TEM analysis, the melting point depression of indium nanostructures has been deduced quantitatively down to particle radii of 2 nm. A new, model-free method of calculating the melting temperature — particle radius relation — was described. The melting point shows a linear decrease with curvature ($1/r$) within the experimental uncertainty, which is compatible with the homogeneous melting mechanism. It is also shown that the theoretical considerations of latent heat of fusion depression with increasing curvature are in reasonable agreement with our experimental results.

3.6 References

1. Fendler, J.H., ed. *Nanoparticles and Nanostructured Films: Preparation, Characterization and Applications*. 1998, Wiley-VCH: Weinheim, Germany.
2. Tu, K.-N., Mayer, J. W., Feldman, L. C., *Electronic Thin Film Science for Electrical Engineers and Materials Scientists*. 1992, New York: Macmillian Publishing Co. 428.
3. Takagi, M., *Electron-diffraction study of liquid-solid transition of thin metal films*. Journal of the Physical Society of Japan, 1954. **9**: p. 359.
4. Berry, R.S., *When the melting and freezing points are not the same*. Scientific American, 1990. **263**(2): p. 68-72, 74.
5. Bertsch, G., *Melting in Clusters*. Science, 1997. **277**: p. 1619.
6. Buffat, P., Borel, J. P., *Size effect on the melting temperature of gold particles*. Physical Review A, 1976. **13**(6): p. 2287-98.
7. Coombes, C.J., *The melting of small particles of lead and indium*. Journal of Physics F: Metal Physics, 1972. **2**(3): p. 441-9.
8. Allen, G.L., Bayles, R. A., Gile, W. W., Jesser, W. A., *Small particle melting of pure metals*. Thin Solid Films, 1986. **144**(2): p. 297-308.
9. Peters, K.F., Cohen, J. B., Chung, Yip-Wah, *Melting of Pb nanocrystals*. Physical Review B, 1998. **57**(21): p. 13430-8.

10. Ajayan, P.M., Marks, L. D., *Experimental evidence for quasimelting in small particles*. Physical Review Letters, 1989. **63**(3): p. 279-82.
11. Unruh, K.M., Huber, T. E., Huber, C. A., *Melting and freezing behavior of indium metal in porous glasses*. Physical Review B, 1993. **48**(12): p. 9021-7.
12. Fei, G.T., Zheng, K., Chu, Z. Q., Qin, Y., Zhang, L. D., Liu, L., *Thermal behavior of the indium particles dispersed in oil*. Materials Research Bulletin, 1997. **32**(7): p. 857-62.
13. Saka, H., Nishikawa, Y., Imura, T., *Melting temperature of In particles embedded in an Al matrix*. Philosophical Magazine A-Physics of Condensed Matter Defects & Mechanical Properties, 1988. **57**(6): p. 895-906.
14. Sheng, H.W., Lu, K., Ma, E., *Melting and freezing behavior of embedded nanoparticles in ball-milled Al-10 wt% M (M=In, Sn, Bi, Cd, Pb) mixtures*. Acta Materialia, 1998. **46**(14): p. 5195-205.
15. Jin, Z.H., Sheng, H. W., Lu, K., *Melting of Pb clusters without free surfaces*. Physical Review B, 1999. **60**(1): p. 141-9.
16. Schmidt, M., Kusche, R., Kronmuller, W., von Issendorff, B., Haberland, H., *Experimental determination of the melting point and heat capacity for a free cluster of 139 sodium atoms*. Physical Review Letters, 1997. **79**(1): p. 99-102.
17. Schmidt, M., Kusche, R., von Issendorff, B., Haberland, H., *Irregular variations in the melting point of size-selected atomic clusters*. Nature, 1998. **393**(6682): p. 238-40.
18. Lai, S.L., Guo, J. Y., Petrova, V., Ramanath, G., Allen, L. H., *Size-dependent melting properties of small tin particles: nanocalorimetric measurements*. Physical Review Letters, 1996. **77**(1): p. 99-102.
19. Lai, S.L., Ramanath, G., Allen, L. H., Infante, P., Ma, Z., *High-speed (10^4 degrees C/s) scanning microcalorimetry with monolayer sensitivity (J/m^2)*. Applied Physics Letters, 1995. **67**(9): p. 1229-31.
20. Lai, S.L., Ramanath, A. G., Allen, L. H., Infante, P., *Heat capacity measurements of Sn nanostructures using a thin-film differential scanning calorimeter with 0.2 nJ sensitivity*. Applied Physics Letters, 1997. **70**(1): p. 43-5.
21. Lai, S.L., Carlsson, J. R. A., Allen, L. H., *Melting point depression of Al clusters generated during the early stages of film growth: nanocalorimetry measurements*. Applied Physics Letters, 1998. **72**(9): p. 1098-100.
22. Tien-Yu Tom, L., Lytle, W. H., Hileman, B., *Application of a CFD tool in designing a fountain plating cell for uniform bump plating of semiconductor wafers*. IEEE Transactions on Components Packaging & Manufacturing Technology Part B-Advanced Packaging, 1996. **19**(1): p. 131-7.

23. Cheng, H.-P., Berry, R. S., *Surface melting of clusters and implications for bulk matter*. Physical Review A, 1992. **45**(11): p. 7969-80.
24. Defay, R., Prigogine, I., *Surface tension and adsorption*. 1951, New York: John Wiley and Sons.
25. Pawlow, P., Zeitschrift fur Physikalische Chemie, 1909. **65**: p. 545.
26. Reiss, H., Wilson, I. B., Journal of Colloid Science, 1948. **3**: p. 551.
27. Sakai, H., *Surface-induced melting of small particles*. Surface Science, 1996. **351**(1-3): p. 285-91.
28. Reiss, H., Mirabel, P., Whetten, R. L., *Capillarity theory for the "coexistence" of liquid and solid clusters*. Journal of Physical Chemistry, 1988. **92**(26): p. 7241-7246.
29. Couchman, P.R., Jesser, W. A., *Thermodynamic theory of size dependence of melting temperature in metals*. Nature, 1977. **269**(5628): p. 481-3.
30. Skripov, V.P., Koverda, V. P., Skokov, V. N., *Size effect on melting of small particles*. Physica Status Solidi A, 1981. **66**(1): p. 109-18.
31. Vanfleet, R.R., Mochel, J. M., *Thermodynamics of melting and freezing in small particles*. Surface Science, 1995. **341**(1-2): p. 40-50.
32. Mori, A., Maruyama, M., Furukawa, Y., *Second-order expansion of Gibbs-Thomson equation and melting point depression of ice crystallite*. Journal of the Physical Society of Japan, 1996. **65**(9): p. 2742-4.
33. *CRC Handbook of Chemistry and Physics*. 78 ed. 1997, Boca Raton, N.Y.: CRC Press.
34. Treilleux, M., Fuchs, G., Santos Aires, F., Melinon, P., Hoareau, A., Cabaud, B., *Amorphous-crystalline phase transformation of supported aggregates produced by indium deposition*. Thin Solid Films, 1990. **191**(1): p. 127-33.
35. Knall, J., Sundgren, J. E., Hansson, G. V., Greene, J. E., *Indium overlayers on clean Si(100)2*1: surface structure, nucleation, and growth*. Surface Science, 1986. **166**(2-3): p. 512-38.
36. Dougherty, E.R., ed. *Digital image processing methods*. Optical engineering. Vol. 42. 1994, Marcel Dekker, Inc.: New York, NY.
37. Molenbroek, A.M., G. ter Horst, and J.W.M. Frenken, *Difference in surface melting between indium (110) and (011)*. Surface Science, 1996. **365**(1): p. 103-17.
38. Samsonov, G.V., ed. *Handbook of the Physicochemical Properties of the Elements*. 1968, IFI/Plenum Press: New York.
39. Gaskell, D.R., in *Physical Metallurgy*. 1983, Elsevier Science: New York.

3.7 Tables and Figures

Table 3-1. Characteristics of indium

| Constant | Value | Description | Reference. |
|---------------|--|--|------------|
| T_m^{bulk} | 429.75 K | bulk melting point | [33] |
| H_m^{bulk} | 28.39 J/g | bulk specific heat of fusion | [33] |
| ρ_s | 7.31 g/cm ³ | solid phase density | [34] |
| ρ_l | 7.02 g/cm ³ | liquid phase density | [33] |
| σ_{sv} | 618±10 mJ/m ² | solid-vapor interfacial tension ^a | [37] |
| σ_{lv} | 560 mJ/m ² | liquid-vapor interfacial tension | [37] |
| σ_{sl} | 63 mJ/m ² | solid-liquid interfacial tension | [9, 37] |
| c_p | 0.211856 + 9.1160×10 ⁻⁵ T J/g K, T<T _m 0.27348 J/g K, T>T _m | specific heat capacity | [38] |

^a average between (110) and (011) faces

Table 3-2. Experimental parameters

| Parameter | Value | Description |
|----------------|---------------------|-------------------------------|
| S | 2.3 mm ² | area of the indium film |
| T _L | 40°C | lower-limit temperature |
| R _L | 1.85±0.1 nm | lower limit radius |
| Q | 0.75±0.1 | volume shape factor |
| r ₀ | <0.5 nm | liquid shell thickness in LSM |

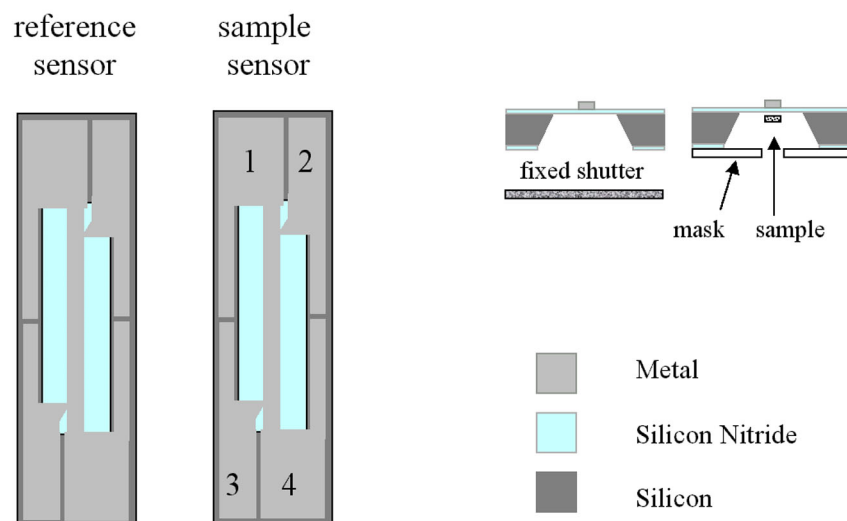


Figure 3-1. Plan-view and cross-sectional representations of the Thin-film calorimeters used for this study. The current pulse is driven between paddles 1 and 4, and the voltage is measured across the central part of the calorimeter using paddles 2 and 3. Differential measurements are achieved by using a second calorimeter on which no sample is deposited.

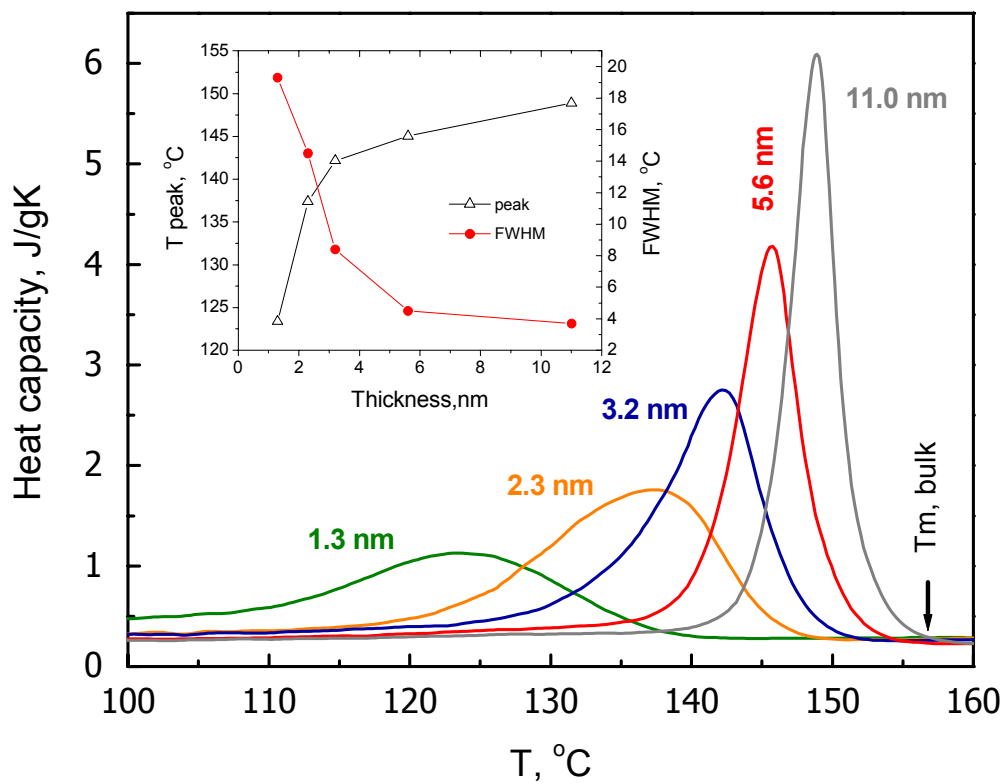


Figure 3-2. Normalized calorimetric curves [i.e., $C_p(T)/\text{mass}$] obtained for the 1.3 nm, 2.3 nm, 3.2 nm 5.6 nm and 11.0 nm indium depositions. The inset shows the progression of the peak temperature and the Full Width at Half Maximum (FWHM) of the melting peak with deposited thickness.

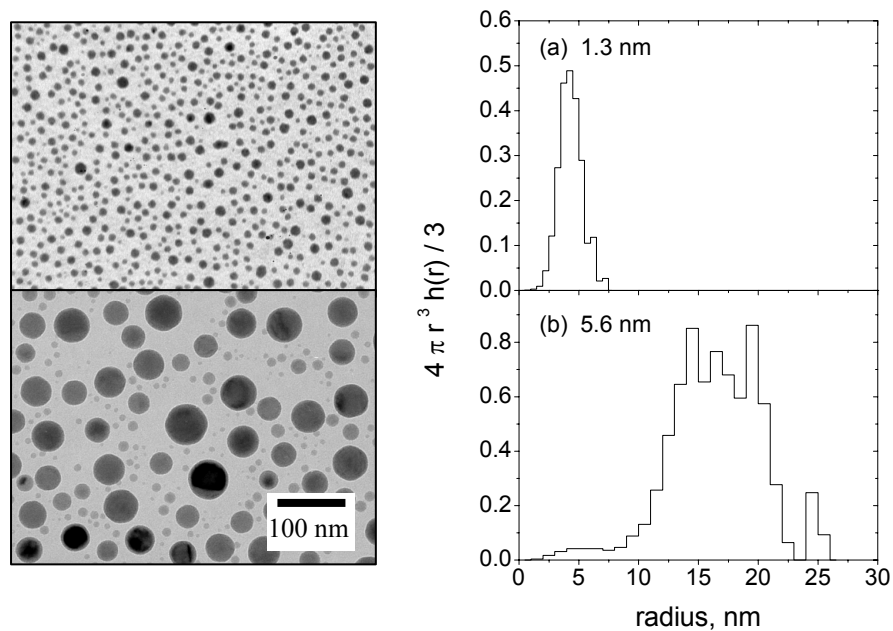


Figure 3-3. TEM images and associated particle size distributions of the (a) 1.3 nm and (b) 5.6 nm samples of Figure 3-2. The particle size distributions (in [particles/nm²]/nm) are multiplied by the volume of the particles ($4\pi r^3/3$) so the vertical axis have no dimensions.

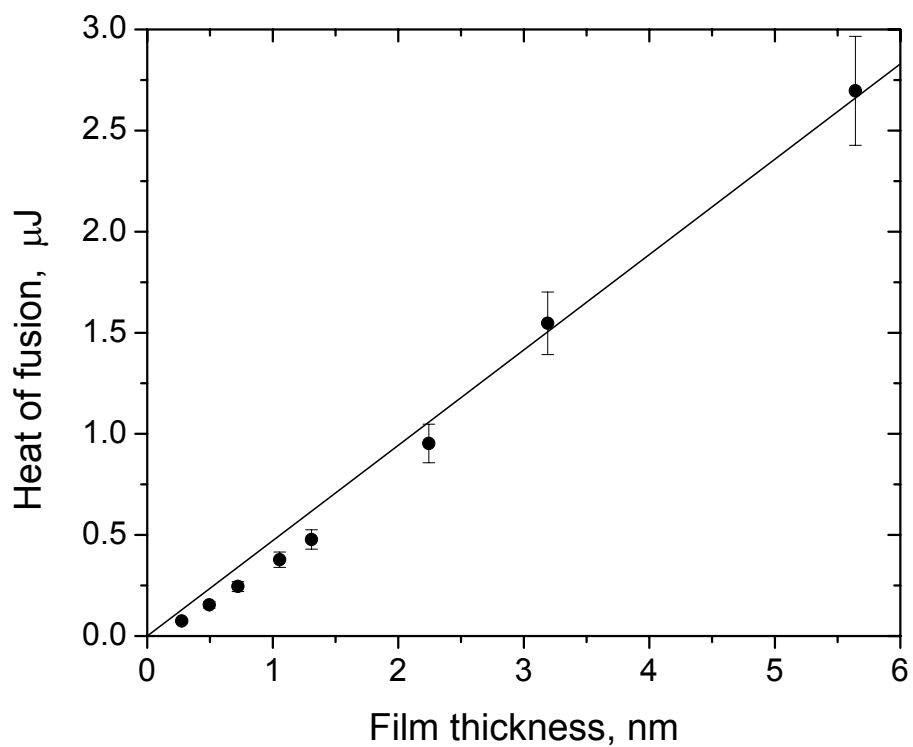


Figure 3-4. Raw data of the heat of fusion (integral of the melting peak) as a function of the deposited thickness for all the experiments. The solid line represents the expected value if all the deposited indium was melting with the bulk heat of fusion.

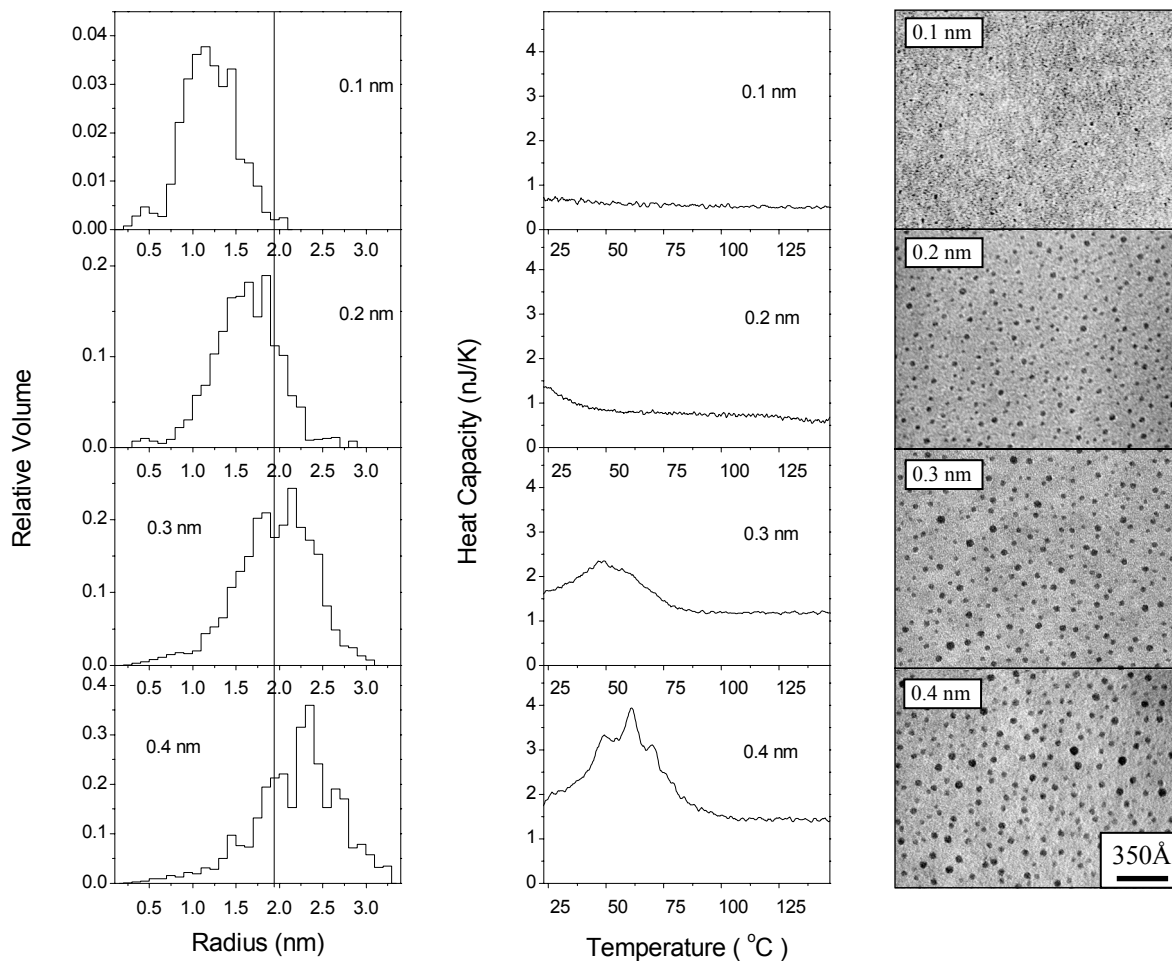


Figure 3-5. TEM images, particle size distribution and associated calorimetric data for the 0.1 nm, 0.2 nm, 0.3 nm, 0.4 nm indium depositions. The radius R_L corresponding to the lower limit temperature T_L is indicated.

$$H_m^{TEM} = \frac{\int [C_p(T) - C_p^0] dT}{S \int \frac{4}{3} \pi r^3 \rho_s h(r) dr}$$

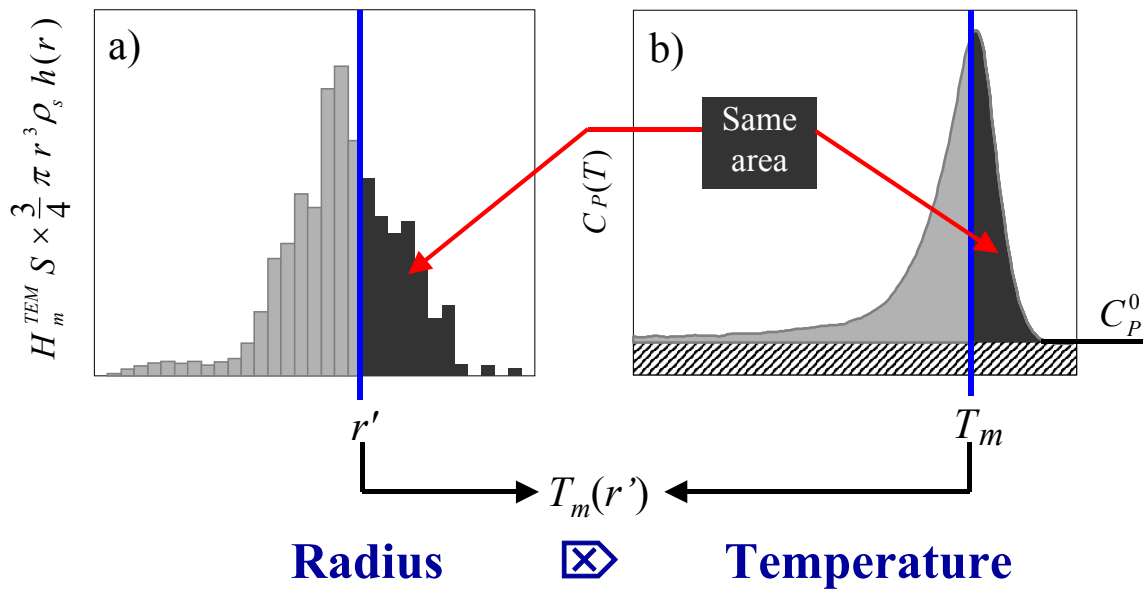


Figure 3-6. Schematic representation of the procedure used to determine the relationship between the melting temperature T_m and the particles radius r . (a) the normalized particle size distribution, which has the same area under the curve than the melting peak in (b) which is the corresponding calorimetric curve. The temperature T_m at which the particles with a radius r melt is such that the area under the right part of both curves is equal.

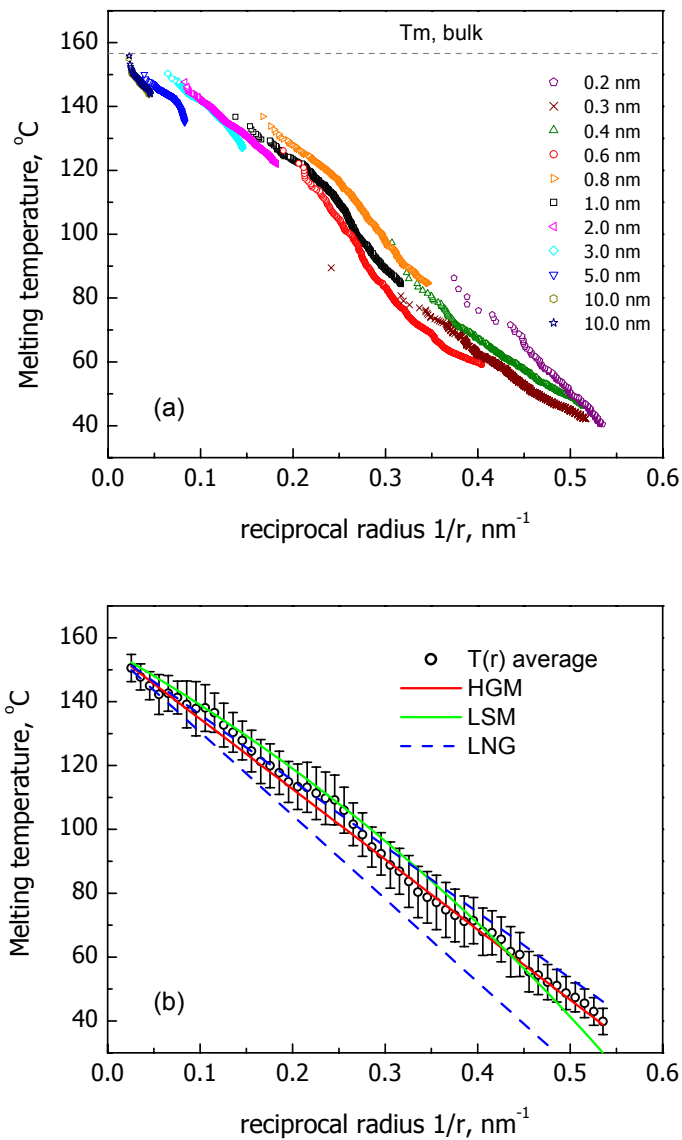


Figure 3-7. Result of the calculation schematically described in Figure 3-6 as a function the reciprocal radius. (a) Result for each experiment. (b) Average of the results in (a) (symbol o). This average result is compared with different melting models (lines).

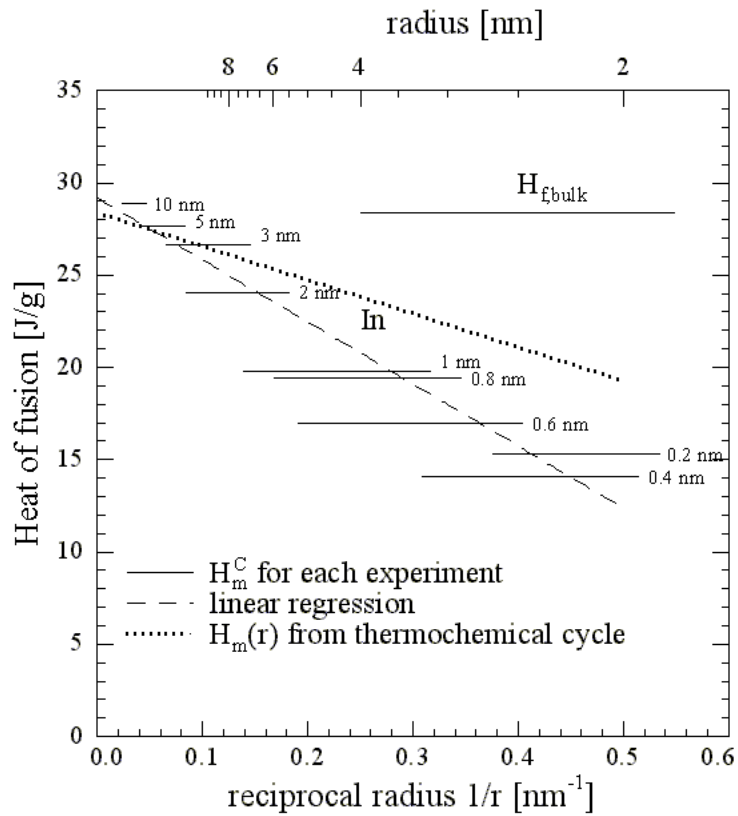


Figure 3-8. Heat of fusion as a function of the reciprocal radius deduced from the melting peak and the estimated melting mass of each experiment (see Section 3.4.2.2) for the details of the calculation). The horizontal solid lines indicate the radius range to which the calculation applies in each case. The dashed line is a linear regression through the data. The dotted line represents the theoretical size-dependence deduced from the thermal chemical cycle of Figure 3-9.

Example:

$r = 2\text{nm}$

$\Delta T = -220/r \text{ (nm K)}$

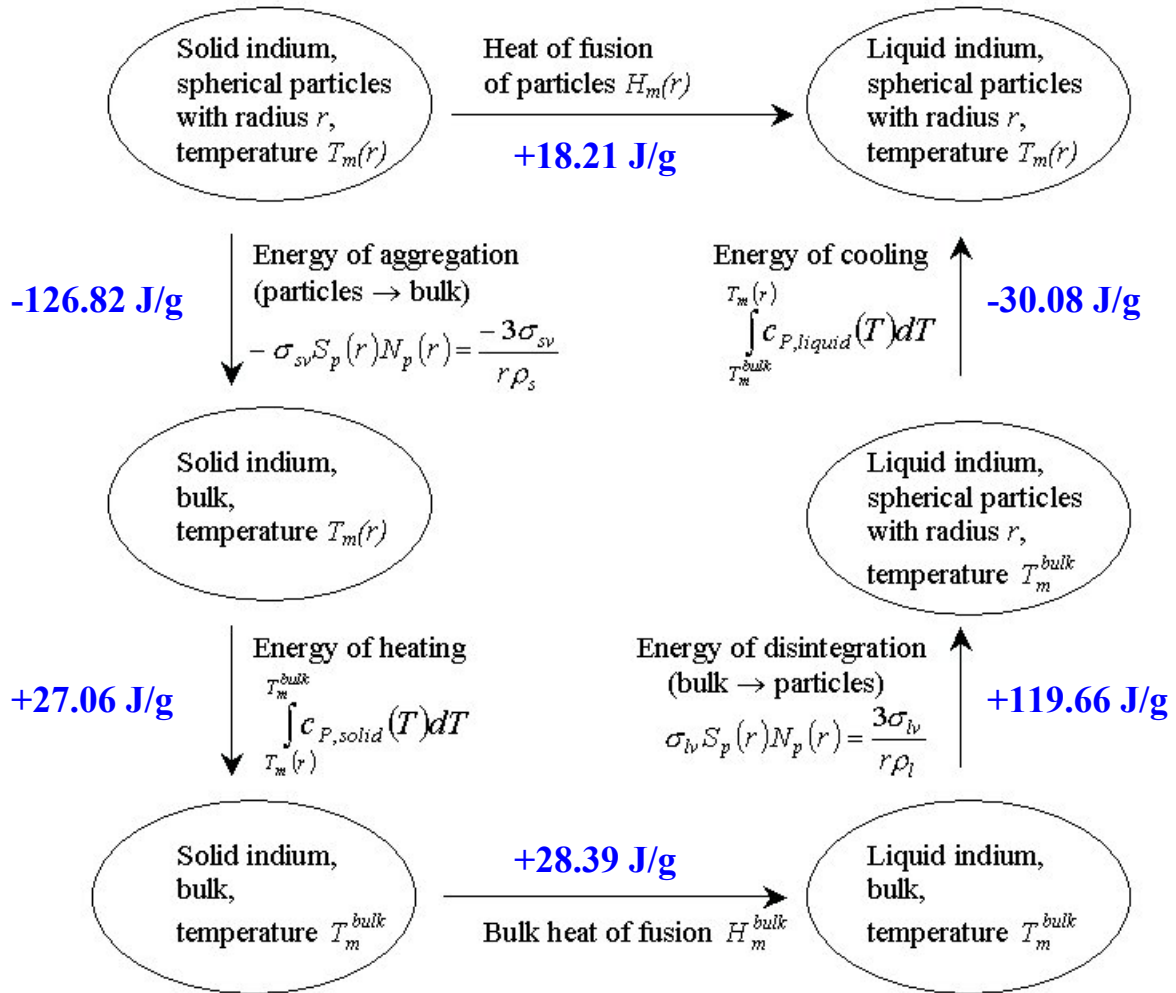


Figure 3-9. The thermochemical cycle, used to estimate of size dependence of the latent heat of fusion $H_m(r)$ using the Hess' Law. $S_p(r)$ and $N_p(r)$ denote the area of particles and the number of particles that can be made from 1 g of indium, respectively; see text for other definitions.

CHAPTER 4

DISCRETE MELTING OF NANO-STRUCTURE ENSEMBLES

We report a study of the thermodynamic properties of indium cluster formation on a SiN_x surface during the early stages of thin film growth using a sensitive nanocalorimetry technique. The calorimetric measurements reveal the presence of abnormal discontinuities in the heat of melting below 100°C . These discontinuities, for which temperature separation corresponds to a spatial periodicity equal to the thickness of an indium monolayer, are found to be related to the atomic "magic numbers", i.e.; the number of atoms necessary to form a complete shell of atoms at particle surface.

4.1 Introduction

The next millennium will be marked by major advances in materials and biology, spearheaded in part by the gains made in manipulating and characterizing materials on the nanometer scale. Materials of nanometer dimensions have unusual thermodynamic properties, that are of great appeal for both scientific and technology communities [1-5]. Two phenomena which are currently of intense interest include (a) discrete nature of nanostructures and clusters which show periodic variations in properties corresponding to some select number of atoms ("magic" numbers) and (b) size-dependent melting point depression of small particles. This area of research is of particular interest in microelectronics for studying the initial stages of thin film growth.

The discrete nature of nanostructures has been observed with clusters deposited on surfaces as well as cluster in beams. It is known that two-dimensional iridium clusters of specific

integral sizes (e.g. Ir₁₉, Ir₃₇, ...) on a surface are considerably more stable than clusters with fewer or greater numbers of atoms [6]. In the cluster beams certain cluster sizes also show enhanced stability, which have been experimentally observed for clusters with a few atoms per cluster up to 22,000 atoms [7].

Size-dependent melting point depression is an important phenomenon for particles of size less than 10 nm. This is due to the increased influence of the surface atoms, which becomes dominant as the ratio of surface/bulk atoms increases. As the particle size decreases, the value of the melting point decreases from the bulk. Size-dependent melting point depression has been confirmed experimentally over a broad range of particle sizes by using a variety of methods [Transmission Electronic Microscopy (TEM) [8], X-ray diffraction (XRD) [9] and differential scanning calorimetry [10]] for particles in cluster beams [11-14] as well as those on surfaces [8, 15]. TEM and XRD measure the melting temperature by monitoring the loss of crystalline structure of the particles with increasing temperature. On the other hand, calorimetry techniques measure the heat involved in the melting process as a function of the temperature.

Recent improvements in nanocalorimetry, which was developed in our laboratory, allow us to measure the phenomenon of melting point depression for particles on surfaces having only 1,000 atoms. At this level of size, small changes in the particle size correspond to large changes in melting point which are easily measured with our nanocalorimeter. Thus we can investigate from the energetic point of view the discrete nature of nanostructures with sizes in the range of 1,000 to 10,000 atoms by measuring the heat capacity of the particles.

In this chapter, we report observations of multiple periodic maxima (melting peaks) in heat capacity measurement of particles in the range of 2-4 nm. These oscillating maxima correspond to particle sizes, which differ incrementally in radius by one atomic monolayer (2.4

Å). These results clearly show the enhanced stability of particles of certain radii as their melting temperature decreases with their size.

4.2 Experimental procedures

The nanostructures studied in this work were formed by thermal evaporation of indium onto the SiN_x membrane surface of the nanocalorimeter (see Figure 4-1). For the very small amounts of indium which were deposited for this study, the films were discontinuous [16], consisting of self-assembled nanostructure with radii of a few nm. The deposition pressure was 1×10^{-8} Torr and no evidence of oxidation of the nanoparticles was observed.

The nanocalorimetry technique used for this study is based on devices that have been developed during the last several years [15, 17-19]. The device shown in Figure 4-1 consists of a thin 30 nm SiN_x membrane typically several millimeter wide. Two metallic strips (Ni, Au, or Pt) with a width of 500 μm and 50nm thick are deposited onto one side of the membrane, and serve both as heaters and as thermometers [20]. By using a thin SiN_x membrane as the support system [21] the sensor has exceptionally low mass addenda. The resistivity of the heater is carefully calibrated against temperature prior to the experiments. Very fast heating (up to 10^6 K/s) rates have been achieved by this method, making the radiative and conductive losses negligible. The calorimetric cell (which includes the metal strip, indium film, and the part of the SiN_x membrane between them) is thus operated under nearly adiabatic conditions. Calorimetry measurements are performed in differential mode where one of the metal strips serves as the reference sensor. The indium is deposited directly on the SiN_x, aligned with one of the metal strips, which serves as the sample heater. Calorimetry measurements are performed in-situ, and proceed by applying a current pulse to both sample and reference metal strips simultaneously. The voltage and current

across the heaters are measured and used for power, temperature and heat capacity calculations. The device also serves as the TEM sample since SiN_x membrane is nearly transparent.

After indium deposition, the calorimeters are scanned to 300°C in order to anneal the particles and make them stable. Then, the calorimetry measurements are performed. Calorimetric data are presented as a relation between the heat capacity of sample C_p and the sample temperature. Each $C_p(T)$ curve presented here is an average of 100 scans, in order to increase the sensitivity. Nevertheless, the features discussed are observable in each single scan.

4.3 Result and discussion

Typically the $C_p(T)$ relation for melting of small particles deposited on a free surface has a single broad endothermic “melting” peak [18]. The area under this peak is equal to the total latent heat of fusion of the particles. The wide size distribution of the deposited particles causes broadening of the melting peak because each particle of a different size melts at a different temperature — a consequence of size-dependent melting point depression.

However, for the smaller indium clusters (2-4 nm), a remarkable effect is observed. The calorimetric curve shows a series of peaks in the low temperature tail, starting at 100°C down to 50°C . $C_p(T)$ data for the 0.4, 0.6 and 0.8 nm indium films are presented in Figure 4-2(d). Only three peaks are present for the 0.4 nm deposition, but after an additional 0.2 nm indium is deposited (increasing the average size of particles in the distribution), we find an additional five peaks generated in the $C_p(T)$ data. It is seen that the position of the peaks with respect to temperature is fixed from one deposition step to the other. Furthermore the peaks persist independently of the heating rate ($3 \times 10^4 \sim 2 \times 10^5$ K/s) and the type of calorimeter (nickel or platinum metallization, and nanocalorimeters with various dimensions).

To quantitatively relate the temperature of the peaks to a specific size of nanostructures we utilize the relationship between size and melting point as derived from our previous work [22]. As is the case of many materials systems documented in the literature, indium nanoparticles show a linear relation between their melting point depression ΔT_m and their curvature (i.e. reciprocal radius r^{-1}) over a broad range of size (down to 2 nm of radius):

$$\Delta T_m = T_m^{bulk} - T_m = \frac{\alpha}{r} \quad (4-1)$$

where T_m is the melting temperature of an indium particle with radius r and T_m^{bulk} is the melting temperature of bulk indium (429.75 K). The slope $\alpha=220\pm 10$ nm K has been determined experimentally [22]. Equation (4-1) corresponds to the widely used homogeneous melting model [23], which is based on Laplace and Gibbs-Duhem equations. According to Eq. (4-1), a melting temperature between 40°C and 100°C corresponds to particles with radii between 2 and 4 nm.

Key information regarding these oscillations is extracted by analyzing the temperature spacing of the peaks, which increases with decreasing temperature. We evaluate these oscillations by relating their temperature to their radius through Eq. (4-1). The radius difference $\delta r_i = r_{i+1} - r_i$ which corresponds to the separation between a maximum T_i and the next T_{i+1} is given by

$$\delta r_i = \frac{\alpha(T_m^{i+1} - T_m^i)}{(T_m^{bulk} - T_m^i)(T_m^{bulk} - T_m^{i+1})}. \quad (4-2)$$

The result of this calculation, using the values found for the different maxima T_m^i , is plotted in Figure 4-2(e). We find that the value of δr_i is constant within experimental uncertainty and corresponds very well with the thickness of an indium monolayer (i.e., between $a/\sqrt{2} = 2.30$ Å and $c/2 = 2.47$ Å, where a and c are lattice parameters of tetragonal indium [24]). As a result, it is clear that the periodicity of the oscillations corresponds to the thickness of an atomic layer.

It should be noted that radii of particles are calculated from the planar view TEM micrographs which contain no information about curvature of particles in cross section. Nevertheless, it has been found by comparison of planar views with mass of film that particles can be represented as truncated spheres with a height-to-radius ratio $q=1.35\pm 0.15$ [22]. Thus the shape of the particles is invariant over the investigated range of size. The particles grow equally in both lateral and tangential direction and the formation of one additional monolayer on the side of the particle corresponds to the formation of one monolayer on the top of the particle.

The above analysis suggests that within the distribution of particles on the SiN_x surface there is a specific set of particle sizes which are more stable than other particles. The peak-to-peak variation of caloric response of our measurement can be discussed in terms of cluster stability. We suggest two factors that contribute to the increased heat of melting for stable clusters. (a) stable particles require more heat during melting than clusters of slightly larger or smaller size, and (b) the number of stable clusters on the surface is larger than those of slightly larger or smaller size.

The first factor that contributes to the increase heat of melting for stable clusters is that the stable particles need more heat in order to melt. Such fluctuations have been widely invoked to explain magic numbers in cluster beams [25, 26]. Two kinds of magic numbers are commonly considered for metallic clusters. The *electronic* magic numbers, resulting of the interference of the free electron waves in a spherical harmonic potential, are given by $N_e \approx i(i+1)(i+2)/3$. The second kind of magic numbers is the *atomic* or *ionic* magic numbers, corresponding to the number of atoms needed to achieve a complete layer of atoms (closed shell) at cluster surface, assuming an icosahedral symmetry. After MacKay [27], they correspond to $N_a = (10 i^3 - 15 i^2 + 11 i - 3)/3$, where i is the shell number.

In order to compare our data with these two models, the volume of the particles corresponding to each maximum T_m^i has been calculated using bulk density of indium and radii according to Eq. (4-1). A spherical shape of particles is assumed in this case (instead of truncated spheres) in order to compare them with magic numbers, calculated for the non-truncated icosahedral clusters. Results are plotted in Figure 4-3, together with the number of atoms corresponding to each magic number model. It is seen that the spacing between our data is very close to the spacing between the atomic magic numbers. However, this result does not imply that the particles actually have an icosahedral symmetry. In general, for any crystal shape which can be approximated as a sphere, adding one monolayer of atoms to the surface increases the radius by an average thickness of a monolayer.

Figure 4-3 also shows the irregularity observed by Schmidt *et al.* in calorimetry measurements of the latent heat of melting for sodium clusters by photo-absorption [13], which could be an extension to even smaller particles of the effect reported here.

The second factor which could effect the amplitude of variations in $C_p(T)$ data is the presence of a non-uniform particle size distribution. For the same energetic reasons mentioned previously, the formation of particles with specific sizes may be favored compared to others, resulting in peaks in the $C_p(T)$ curve.

Measurement of the non-uniform size distribution is the means by which stable clusters (magic numbers) are identified in most cluster beam studies [25]. Clusters in our experiment are formed during evaporation and the subsequent annealing through the processes of surface diffusion, Ostwald ripening and coalescence. No oscillation is observed before annealing while oscillations are observed after annealing. Therefore, there is a reasonable possibility for the

formation of a nonuniform size distribution through the process of long range mass transport on the surface.

The most direct way to evaluate the uniformity of particle distribution is by analyzing the distribution data from TEM measurements. However, insufficient the resolution of our TEM measurements is only about 2~3 Å and the variation in the background of the image due to the SiNx prevent us from extracting the size of the particles with the required precision.

Finally we estimate the absolute energy associated with the oscillations. Assuming a uniform particle distribution within $\delta r/2$, the heat of melting fluctuates by ~50 eV/particle for particles with T_m from 60 °C (peak) to 65 °C (valley). However, the theoretical estimations of this value were made for only small particles (for atomic shells up to 4th) due to computational difficulties [28, 29].

4.4 Conclusion

In summary, we have used a sensitive nanocalorimetry technique to investigate the thermodynamic properties of indium cluster formation during the early stages of thin film growth. For the first time, we observe multiple periodic melting peaks in the heat capacity data, which we analyze via the size-dependent melting point depression properties of the indium system. We conclude that there is a certain set of clusters with specific sizes, which are more stable than other sizes. The incremental difference between the sizes of these stable particles corresponds to one atomic layer in radial thickness.

4.5 References

1. Tu, K.-N., Mayer, J. W., Feldman, L. C., *Electronic Thin Film Science for Electrical Engineers and Materials Scientists*. 1992, New York: Macmillian Publishing Co. 428.

2. Thompson, C.V., *Coarsening of particles on a planar substrate: interface energy anisotropy and application to grain growth in thin films*. Acta Metallurgica, 1988. **36**(11): p. 2929-34.
3. Harper, J.M.E., Colgan, E. G., Hu, C. K., Hummel, J.P., Buchwalter, L. P., Uzoh, C. E., *Materials issues in copper interconnections*. MRS Bulletin, 1994. **19**(8): p. 23.
4. Singhal, A., Gibson, J. M., Treacy, M. M. J., Lane, P. D., Shapley, J. R., *Stability of supported organometallic clusters probed by a mass-sensitive TEM technique*. Journal of Physical Chemistry, 1996. **100**(16): p. 6385-8.
5. Tung, R.T., *Surface nucleation of Ti silicides at elevated temperatures*. Applied Physics Letters, 1996. **68**(14): p. 1933-5.
6. Wang, S.C., Ehrlich, G., *Equilibrium shapes and energetics of iridium clusters on Ir(111)*. Surface Science, 1997. **391**(1-3): p. 89-100.
7. Martin, T.P., Bergmann, T., Gohlich, H., Lange, T., *Observation of electronic shells and shells of atoms in large Na clusters*. Chemical Physics Letters, 1990. **172**(3-4): p. 209-13.
8. Allen, G.L., Bayles, R. A., Gile, W. W., Jesser, W. A., *Small particle melting of pure metals*. Thin Solid Films, 1986. **144**(2): p. 297-308.
9. Peters, K.F., Cohen, J. B., Chung, Yip-Wah, *Melting of Pb nanocrystals*. Physical Review B, 1998. **57**(21): p. 13430-8.
10. Unruh, K.M., Huber, T. E., Huber, C. A., *Melting and freezing behavior of indium metal in porous glasses*. Physical Review B, 1993. **48**(12): p. 9021-7.
11. Bertsch, G., *Melting in Clusters*. Science, 1997. **277**: p. 1619.
12. Berry, R.S., *When the melting and freezing points are not the same*. Scientific American, 1990. **263**(2): p. 68-72, 74.
13. Schmidt, M., Kusche, R., von Issendorff, B., Haberland, H., *Irregular variations in the melting point of size-selected atomic clusters*. Nature, 1998. **393**(6682): p. 238-40.
14. Schmidt, M., Kusche, R., Kronmuller, W., von Issendorff, B., Haberland, H., *Experimental determination of the melting point and heat capacity for a free cluster of 139 sodium atoms*. Physical Review Letters, 1997. **79**(1): p. 99-102.
15. Lai, S.L., Guo, J. Y., Petrova, V., Ramanath, G., Allen, L. H., *Size-dependent melting properties of small tin particles: nanocalorimetric measurements*. Physical Review Letters, 1996. **77**(1): p. 99-102.
16. Knall, J.S., J. E., Hansson, G. V., Greene, J. E., *Indium overlayers on clean Si(100)2*1: surface structure, nucleation, and growth*. Surface Science, 1986. **166**(2-3): p. 512-38.

17. Lai, S.L., Ramanath, G., Allen, L. H., Infante, P., Ma, Z., *High-speed (10^4 degrees C/s) scanning microcalorimetry with monolayer sensitivity (J/m^2)*. Applied Physics Letters, 1995. **67**(9): p. 1229-31.
18. Lai, S.L., Ramanath, A. G., Allen, L. H., Infante, P., *Heat capacity measurements of Sn nanostructures using a thin-film differential scanning calorimeter with 0.2 nJ sensitivity*. Applied Physics Letters, 1997. **70**(1): p. 43-5.
19. Lai, S.L., Carlsson, J. R. A., Allen, L. H., *Melting point depression of Al clusters generated during the early stages of film growth: nanocalorimetry measurements*. Applied Physics Letters, 1998. **72**(9): p. 1098-100.
20. Worthing, A.G., *Atomic Heats of Tungsten and of Carbon at Incandescent Temperatures*. Physical Review, 1918. **12**(3): p. 199-225.
21. Denlinger, D.W., Abarra, E. N., Allen, K., Rooney, P. W., Messer, M. T., Watson, S. K., Hellman, F., *Thin film microcalorimeter for heat capacity measurements from 1.5 to 800 K*. Review of Scientific Instruments, 1994. **65**(4): p. 946-59.
22. Zhang, M., Efremov, M. Yu., Schiettekatte, F., Olson, E. A., Kwan, A. T., Lai, S. L., Wisleder, T., Greene, J. E., Allen, L. H., *Size-dependent melting point depression of nanostructures: Nanocalorimetric measurements*. Physical Review B, 2000. **62**(15): p. 10548-10557.
23. Buffat, P., Borel, J. P., *Size effect on the melting temperature of gold particles*. Physical Review A, 1976. **13**(6): p. 2287-98.
24. *CRC Handbook of Chemistry and Physics*. 78 ed. 1997, Boca Raton, N.Y.: CRC Press.
25. Brack, M., *The physics of simple metal clusters: self-consistent jellium model and semiclassical approaches*. Reviews of Modern Physics, 1993. **65**(3): p. 677-732.
26. de Heer, W.A., *The physics of simple metal clusters: experimental aspects and simple models*. Reviews of Modern Physics, 1993. **65**(3): p. 611-75.
27. Mackay, A.L., *A dense non-crystallographic packing of equal spheres*. Acta Crystallographica, 1962. **15**: p. 916-918.
28. Cheng, H.-P., Berry, R. S., *Surface melting of clusters and implications for bulk matter*. Physical Review A, 1992. **45**(11): p. 7969-80.
29. McClurg, R.B., Flagan, R. C., Goddard, W. A., J. Chem. Phys., 1996. **105**: p. 7648.

4.6 Figures

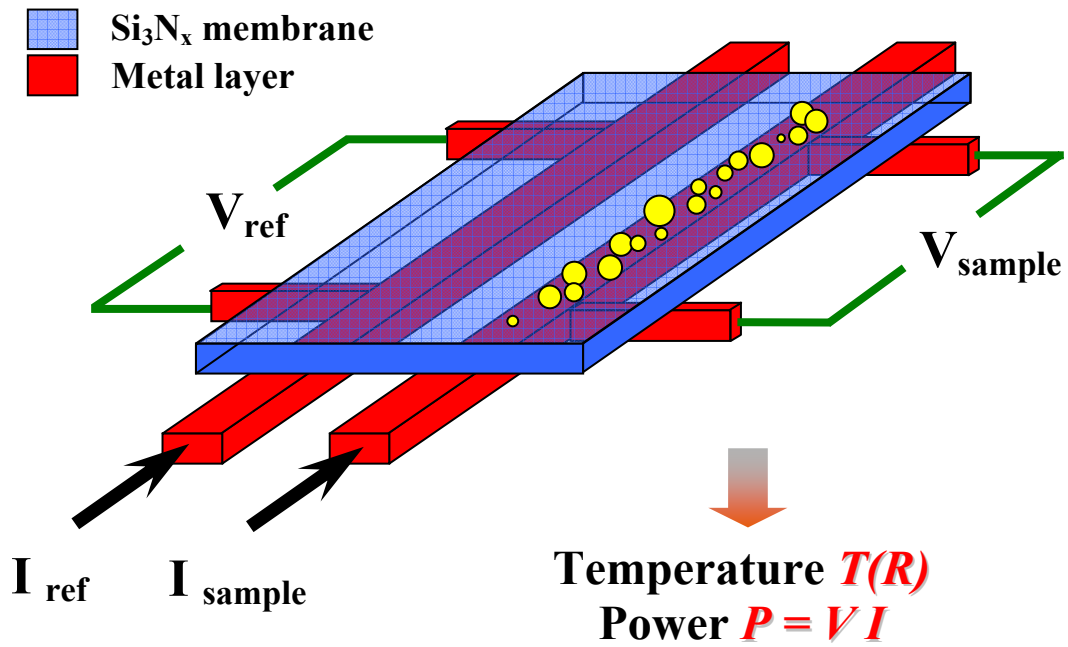


Figure 4-1. The schematic diagram of the nanocalorimeter showing two metallic strips, which serve as both heaters (sample and reference) and thermometers. These strips are supported by a thin SiN_x membrane. Indium is deposited on the membrane side of the nanocalorimeter directly above the sample heater.

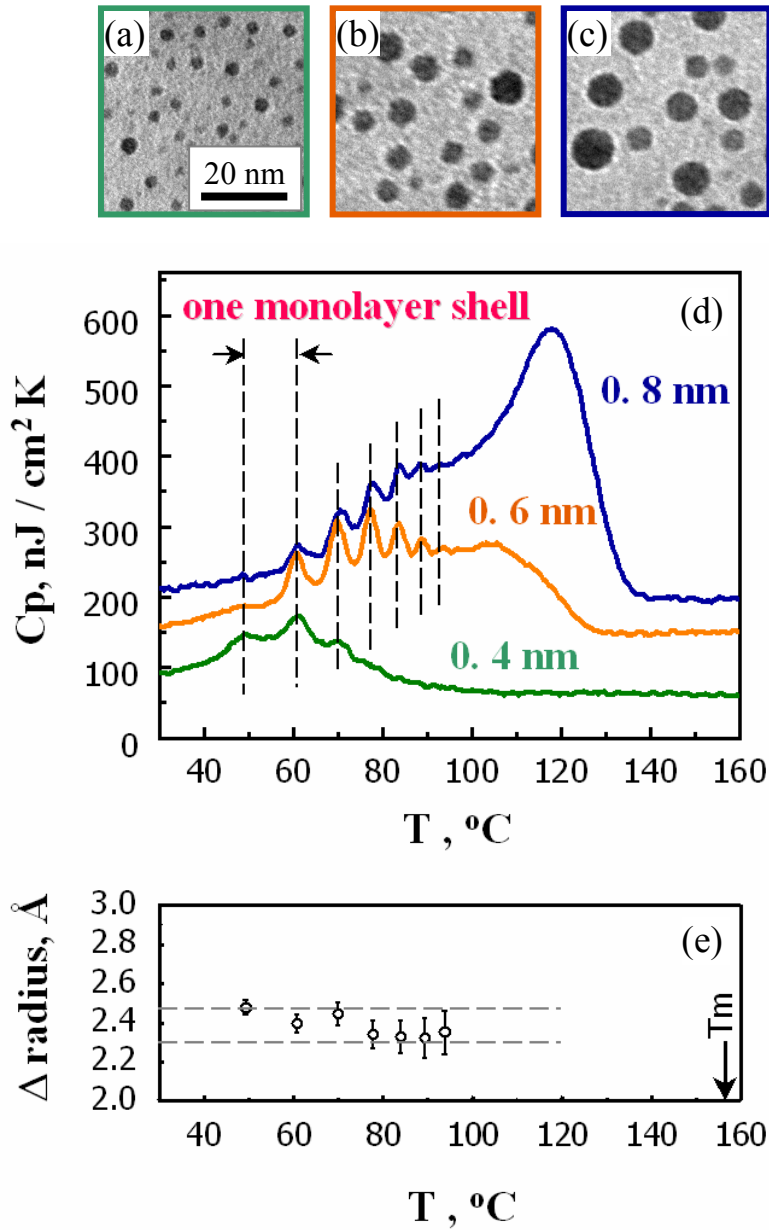


Figure 4-2. Ex situ TEM micrographs of the nanoparticles generated in the deposition experiments of the (a) 0.4 nm, (b) 0.6 nm, and (c) 0.8 nm indium films. Corresponding calorimetric curves (d) with vertical dashed lines indicating the position in temperature of each maximum. (e) Radius difference corresponding to the separation between adjacent maxima, as calculated using Equation (4-2). The horizontal dashed lines represent to the thickness of a monolayer for the two bulk lattice parameters of indium.

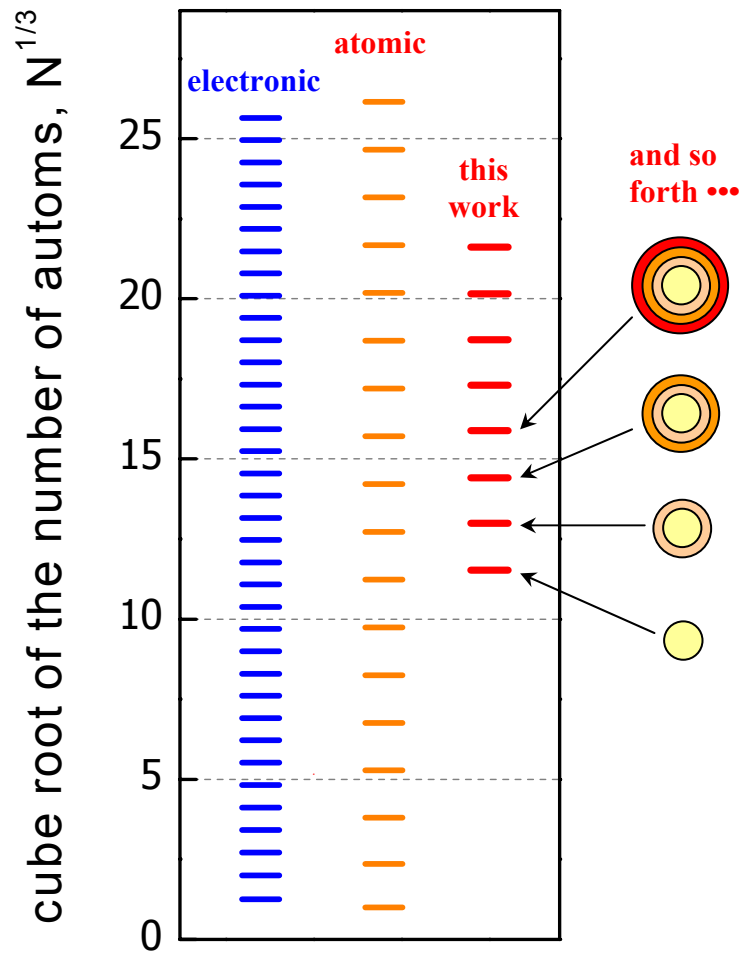


Figure 4-3. Number of the atoms corresponding to the size of the particles associated with each melting point maxima T_m^i in comparison to the atomic and the electronic magic numbers.

CHAPTER 5

REAL-TIME NANOCALORIMETRY

The scanning nanocalorimetry technique is utilized to characterize thin film growth in real-time. The technique generates 3-dimensional heat capacity data as a function of temperature and thickness that show the continuous change of indium film during deposition. The measurement interval is $\sim 4 \times 10^{-3}$ nm in thickness. Indium thin films form nanoparticles on silicon nitride surfaces that show the phenomena of melting point depression and the formation of magic number size particles. The measured increment of the heat capacity ΔC_p is ~ 30 pJ/K and the temperature resolution is better than 0.5K.

5.1 Introduction

In-situ and real-time measurement techniques are of great importance in thin film studies for microelectronics [1-3]. In-situ experiments such as x-ray diffraction [4-6] and ellipsometry [7, 8] provide contamination-free measurements which can be critical for thin film and surface investigations. Real-time measurements allow the experimenter to study the evolution of a thin film on an incremental level less than one monolayer. They are suitable to track key aspects of the growth process. The techniques reduce systematic errors that are inherent in “one-at-a-time” type experiments. They can lead to the discovery of small effects, which are otherwise submerged by the experimental uncertainties. The fine-scale sampling property also allows one to track processes and effects observable only in narrow thickness ranges.

Heat capacity measurements are useful in characterizing materials. The measurements can be used to study phase transitions such as melting, glass transitions, etc., and to track exothermic or endothermic chemical reactions. Nanocalorimetry [9] technique is especially suitable for measuring the heat capacity of small materials. It is sensitive to measure thin films from sub-monolayer thick to hundreds of nanometers. Besides the high sensitivity, scanning nanocalorimetry also features adjustable heating rates up to 10^6 K/sec. Ultra-fast heating allows individual caloric measurement to be performed sequentially within one second intervals, thus enabling the characterization of thin film growth in real-time.

Real-time nanocalorimetry measurement depends on two key factors: sensitive electronics and fast data processing. In recent years, high speed digitizing technique has been renovated in terms of sensitivity, resolution and sampling rate. For example, NI5911 card can have 19 bit resolution working at 100 kHz which is over ten times better than older type of 16 bit devices like HP3458A. Equivalent random noise from analog to digital conversion is ten times smaller. Therefore repeatedly scans in previous experiments are not strictly required.

The methods on how to calculate heat capacity from a nanocalorimetry experiment have been summarized into our recent publication [10]. The central idea of the data processing is to suppress noise and to correct the differences of the measurement in both time and temperature domain. The established accurate method takes long time and multiple steps, while the simple method is too noisy and has not enough corrections. Both methods assume that ambient temperature is constant and sensors are stable during the experiment. However, such conditions are not true especially in a real-time

experiment — radiation from an evaporation source will affect the sensor when sensor exposes to it. To achieve real-time measurements, a fast heat capacity analysis with reasonable accuracy is of necessary.

5.2 Fast heat capacity calculation

A nanocalorimetry experiment usually has three sets of measurement. (1) The drift measurement, which practices the sensor and monitors its stability characteristics; (2) The base line measurement, which measures the heat capacity of nanocalorimeter sensor addenda only; (3) The calorimetry measurement, which measures heat capacity of the sensor addenda plus the sample. The first two measurements serve as preparation for the third measurement to obtain sample information.

The heat capacity can be calculated in time domain as:

$$C_p(t) = \frac{dQ(t)}{dT(t)} = \frac{P(t)}{dT(t)/dt} \quad (5.1a)$$

$$P(t) = V(t) \times I(t) \quad (5.1b)$$

$$T(t) = \alpha_0 + \alpha_1 R(t) + \alpha_2 R(t)^2 + 3\alpha_3 R(t)^3 + 4\alpha_4 R(t)^4 \quad (5.1c)$$

$$R(t) = V(t) / I(t) \quad (5.1d)$$

$$I(t) = V_i(t) / R_0 \quad (5.1e)$$

where R_0 is a standard resistor. Equation (5.1c) is a 4th polynomial fit of sensor calibration curve $T(R)$ before the nanocalorimetry experiment. Temperature Coefficient of Resistance (TCR) is a material property but practically varies among different sensors. From above equations one can see that the heat capacity measurement can be simply achieved by voltage measurements.

Experimentally, $V(t)$ and $V_1(t)$ are too noisy to reflect very small changes. Limitation is from electronics. Smoothing functions or digital filters can be applied to reduce the noise. The efforts, however, are quite limited since small signals can also be attenuated. Noise component in the $P(t)$ is the product of $I(t)$ and $V(t)$. Practically it does not affect to the final result. Heating rate (dT/dt), on the contrary, is a derivative term that dominates the heat capacity signal, which is the key part in data processing (see Equation (5.1)). Therefore, the temperature determination, i.e., the resistance measurement, is important.

In a differential scheme (see Figure 2-2), a higher quality signal, differential voltage, is measured. Simultaneously, voltage and current signals for both sample and reference are also recorded. Thus, one can express $V_s(t)$ as:

$$V_s(t) = V_r(t) + dV(t) \quad (5.2)$$

In such arrangement, $V_r(t)$ is the voltage across reference sensor that hopefully provides a continuously changed signal which is not sensitive to the smoothing, filtering or even fitting by a polynomial function. Thus noise level in $V_s(t)$ can approach that in differential measurement with sample information mostly kept. For further improvement, the S-G method can be applied to smooth $dV(t)$ to get better results.

Ideally, if the current through the sensor is constant, the solution will be very simple. However, this is difficult to achieve because the necessary power, the noise and the feedback circuit are concerned. The electronic system employs low noise component — capacitor as the power source. During each nanocalorimetry measurement, resistance of the sensor increases due to Joule heat. Correspondingly, the voltage across the sensor $V(t)$ also increases and the current through the sensor $I(t)$ decreases. Sensor resistance

has to be smaller than the total other resistance in the circuit, since additional resistors in series have to be used in order to regulate the pulse current (the heating rate in caloric scans). Therefore the current through the sensor decreases, but very small (< 4% for a 10ms 45 mA current pulse for example). This is a situation close to a constant current since majority changes due to the sample are reflected in the voltage signals.

Practically one can fit the $I(t)$ by the polynomial function. This is suitable for very thin samples where small changes are negligible compared to the noise. Large signals will have problems since the polynomial fitting does not work well for a continuously changed curve with terraces in the middle. In this case a low pass Fast Fourier Transform (FFT) filter can be applied to get reasonably good results.

According to Equation (5.1) heat capacity as a function of time can be calculated and then convert to $Cp(T)$. The result is the heat capacity from both the sample and sensor addenda. In the baseline measurement, addenda heat capacity is measured as $Cp_0(T)$. So, sample heat capacity $Cp_{sample}(T)$ can be calculated as:

$$Cp_{sample}(T) = Cp(T) - Cp_0(T) \quad (5.3)$$

Equation (5.3) is quite straightforward, but not that simple in a real operation. The subtraction should be done according to the temperature, while all the raw data are acquired in the time domain. Therefore $Cp_0(T)$ should be calculated either using a fitted function or the interpolated value from $Cp_0(T_0)$, where T_0 is the temperature in baseline measurement.

Note that Equation (5.3) is based on the assumption that heat capacity information is only a function of temperature. So voltage information and calculated heat capacity information are totally separated, as long as the TCR of the sensor does not change. This

is good for a real-time nanocalorimetry experiment that usually takes several thousand scans, where slightly drift of sensor electrical property is unavoidable. In more detailed investigations, heat loss, temperature distribution, and thermal conductivity contribution have to be considered. Those corrections are usually small (usually only a few percent of the total signal). Details can be found in reference [10].

The fast heat capacity calculation takes the advantages of better computers as well as the advance in digitizing technology. The data processing can be performed with the result plotted within one second scan interval based on a LabView program using PC platform. The analyzed results approach to that reported in regular nanocalorimetry work [10].

5.3 Experimental procedure

An indium thin film is deposited onto the nitride side of the sample sensor. The area is about 2 mm² aligned to the heater by a shadow mask. The pressure during the entire experiment is maintained at 1~2×10⁻⁸ torr. The calorimetric measurements are initiated by applying synchronized DC electrical pulses to both sample and reference heaters. High heating rates from 30 to 200 k K/s are used to achieve near-adiabatic conditions. The current and voltage through the sensors are measured during the pulse scans. The recorded data is used to calculate resistance and power in the first step, and the temperature and heat capacity in a second step.

The required stability of electrical characteristics of sensors is achieved by annealing at 450 °C under high vacuum (~10⁻⁸ torr) for two hours and by making several thousands repetitive measurements before the experiment. The “burned-in” sensors are

then electrically stable during the measurement. Indium deposition is accomplished via thermal evaporation. A critical step in this experiment was to replace the inherently noisy silicon control rectifier (SCR) unit by an autotransformer to control the current for evaporation. Small, thin boats are employed to reduce the total power needed for evaporation. This limits the effect of radiation, which ensures that sensor characteristics are stable during the measurement. For the purpose of real-time measurement, a slow, constant evaporation rate ($0.24\text{\AA}/\text{min}$) is first achieved. Nanocalorimetry measurements are then taken at 1s intervals and are averaged every 10 scans. Since radiation from the evaporation source causes a shift when the caloric sensor is first exposed to it, a baseline measurement with the radiation effect is used, and regular caloric measurements before and after the real-time measurement are taken for calibration. A quartz crystal monitor for comparison also monitors the deposited thin film thickness. Note the nature of the measurement unavoidably heats the sample — nanocalorimetry scan heats the indium up to $300\text{ }^{\circ}\text{C}$. The studied thin film is inherently annealed.

5.4 Result and discussion

Figure 5-1 shows a 3D plot of heat capacity vs. temperature vs. thickness that is the result of real-time in-situ nanocalorimetry. The growth of indium on the silicon nitride surface film follows Volmer-Weber growth dynamics [11]. At the early growth stage, the film is discontinuous and consists of nanometer-sized particles. The particles melt at different temperatures. The melting temperature depends on the surface curvature and decreases as size decreases. This is the phenomenon of melting point depression [12].

The peak on each caloric curve represents the endothermic process of melting. The area under the peak is the heat of fusion. One can see in the figure that the melting temperature throughout the deposition is well below the bulk value of indium (156.6 °C). Instead of the sharp melting peak for bulk materials, the caloric curves of thin film indium are extremely broad. As more and more material is deposited onto the surface, the melting peak becomes sharper and shifts towards bulk melting temperature.

We analyze the data by focusing on three main features. (A) the temperature region in which all of the nanoparticles are liquid; (B) the melting peak of the film which illustrates size-dependent melting point depression; and (C) the multiple maxima observed at low temperature (50-90 °C) that are related to the formation of magic number particles.

Heat capacity measurements of liquid indium are shown Figure 5-2(a). Heat capacity is an extensive characteristic of materials. It increases linearly with the mass. One can use the heat capacity to measure the amount of deposited materials. When comparing sequential caloric scans during deposition, the heat capacity of the film systematically increases, as does the mass of the indium. Figure 5-2(b) is the average value of the heat capacity between 170 and 255 °C as a function of integrated indium thickness. The average is taken over a wide temperature range to increase sensitivity. Due to the melting point depression, only liquid state heat capacity data is available for illustration.

The results show the remarkable sensitivity of the measurement and illustrate the capability for characterizing fine details during deposition. Using the technique we can easily resolve film thickness of 0.04 Å and heat capacities of 30 pJ/K.

Caloric data show melting point depression phenomenon (Figure 5-3(a)). This figure illustrates the continuous nature of the melting property change with the amount of material. The width of the melting peak is due to the combination of size distribution and size-dependent melting. For each scan, the smallest particles contribute to the endothermic signal at the beginning (low temperature) of the peak, while the largest ones contribute at the high temperature section of the peak. As deposition proceeds, the overall melting temperature substantially increases as expected since the average size of the clusters also increases. We quantitatively track the overall melting process by obtaining a peak melting temperature of the film, which increases from 100 to 135 °C as the integrated film thickness increases from 0.5 to 1.3 nm shown in Figure 5-3(b).

Figure 5-4 shows the caloric response at low temperature section (region C in Figure 5-1). Note the multiple maxima at the low temperatures. This is unexpected since one assumes the size distribution of nanoparticles at the very early stages of deposition should be smooth, and particles are physically similar to each other, thus the caloric response should also be smooth showing one single melting peak. However, a detailed analysis of the position of the multiple maxima [13] indicate that certain size nanoparticles are favored over other sizes. Similar effect has also been observed in magic numbers in cluster beams [14] and epitaxial surfaces [15]. The maxima temperatures correspond to the particle size by discrete one monolayer difference [13]. Unlike the variation of the main melting peak, which is illustrated in Figure 5-3, the melting point of the selected size nanoparticle is relatively constant.

This degree of constancy of the temperature of one single size nanoparticle is difficult to establish using single-shot experiments when comparing one experiment to

another. This is because errors in temperature can be due to the differences between sensors, differences in ambient temperature, etc. However, the real-time measurement clearly shows that the positions of these local maxima do remain extremely steady during the thin film growth. The graph in Figure 5-4(b) shows that variation in the melting temperature of the example maxima in Figure 5-4(a) (60.6°C) is very small ($\pm 0.2^{\circ}\text{C}$).

5.5 Conclusion

In summary, the nanocalorimetry technique is applied for real-time characterizing the thin film growth. The technique is used in generating 3D heat capacity plots that show the continuous property changes of the thin film during deposition. At the early stage indium growth, nanoparticles are formed and show the phenomena of melting point depression and the formation of magic number sized nanoparticles. The resolution of the measurement achieves ~ 30 pJ/K for heat capacity and 0.04\AA for thickness.

5.6 References

1. Mayer, J.A., Lau, S. S., *Electronic Materials Science: For Integrated Circuits in Si and GaAs*. 1990, New York: Macmillan Publishing Co. 476.
2. Maissel, L.I., Glang, R., *Handbook of thin film technology*. 1970, New York: McGraw-Hill.
3. Lu, C., Czanderna, A. W., *Applications of Piezoelectric Quartz Crystal Microbalances*. 1984, Amsterdam: Elsevier.
4. Zhang, S.L., d'Heurle, F. M., Lavoie, C., Cabral, C. Jr., Harper, J. M. E., *Enhanced thermal stability of C49 TiSi/sub 2/ in the presence of aluminum*. Applied Physics Letters, 1998. **73**(3): p. 312-14.
5. Cabral, C., Jr., Lavoie, C., Harper, J. M. E., Jordan-Sweet, J., *The use of in situ X-ray diffraction, optical scattering and resistance analysis techniques for evaluation of copper diffusion barriers in blanket films and damascene structures*. Thin Solid Films, 2001. **397**(1-2): p. 194-202.

6. Peters, K.F., Cohen, J. B., Chung, Yip-Wah, *Melting of Pb nanocrystals*. Physical Review B, 1998. **57**(21): p. 13430-8.
7. Feng, G.F., Katiyar, M., Maley, N., Abelson, J. R., *Silicon epitaxy at 230 degrees C by reactive DC magnetron sputtering and its in situ ellipsometry monitoring*. Applied Physics Letters, 1991. **59**(3): p. 330-2.
8. Liu, C., Erdmann, J., Macrander, A., *In situ spectroscopic ellipsometry as a surface-sensitive tool to probe thin film growth*. Thin Solid Films, 1999. **355-356**: p. 41-8.
9. Lai, S.L., Ramanath, A. G., Allen, L. H., Infante, P., *Heat capacity measurements of Sn nanostructures using a thin-film differential scanning calorimeter with 0.2 nJ sensitivity*. Applied Physics Letters, 1997. **70**(1): p. 43-5.
10. Efremov, M.Y., Olson, E. A., Zhang, M., Zhang, Lai, S. L., Schiettekatte, F., Z. S., Allen, L. H., *Thin-Film Differential Scanning Nanocalorimetry: Heat Capacity Analysis*. Thermochemica Acta, 2003: p. submitted.
11. Tu, K.-N., Mayer, J. W., Feldman, L. C., *Electronic Thin Film Science for Electrical Engineers and Materials Scientists*. 1992, New York: Macmillian Publishing Co. 428.
12. Zhang, M., Efremov, M. Yu., Schiettekatte, F., Olson, E. A., Kwan, A. T., Lai, S. L., Wisleder, T., Greene, J. E., Allen, L. H., *Size-dependent melting point depression of nanostructures: Nanocalorimetric measurements*. Physical Review B, 2000. **62**(15): p. 10548-10557.
13. Efremov, M.Y., Schiettekatte, F., Zhang, M., Olson, E. A., Kwan, A. T., Berry, R. S., Allen, L. H., *Discrete periodic melting point observations for nanostructure ensembles*. Physical Review Letters, 2000. **85**(17): p. 3560-3563.
14. Schmidt, M., Kusche, R., von Issendorff, B., Haberland, H., *Irregular variations in the melting point of size-selected atomic clusters*. Nature, 1998. **393**(6682): p. 238-40.
15. Wang, S.C., Ehrlich, G., *Equilibrium shapes and energetics of iridium clusters on Ir(111)*. Surface Science, 1997. **391**(1-3): p. 89-100.

5.7 Figures

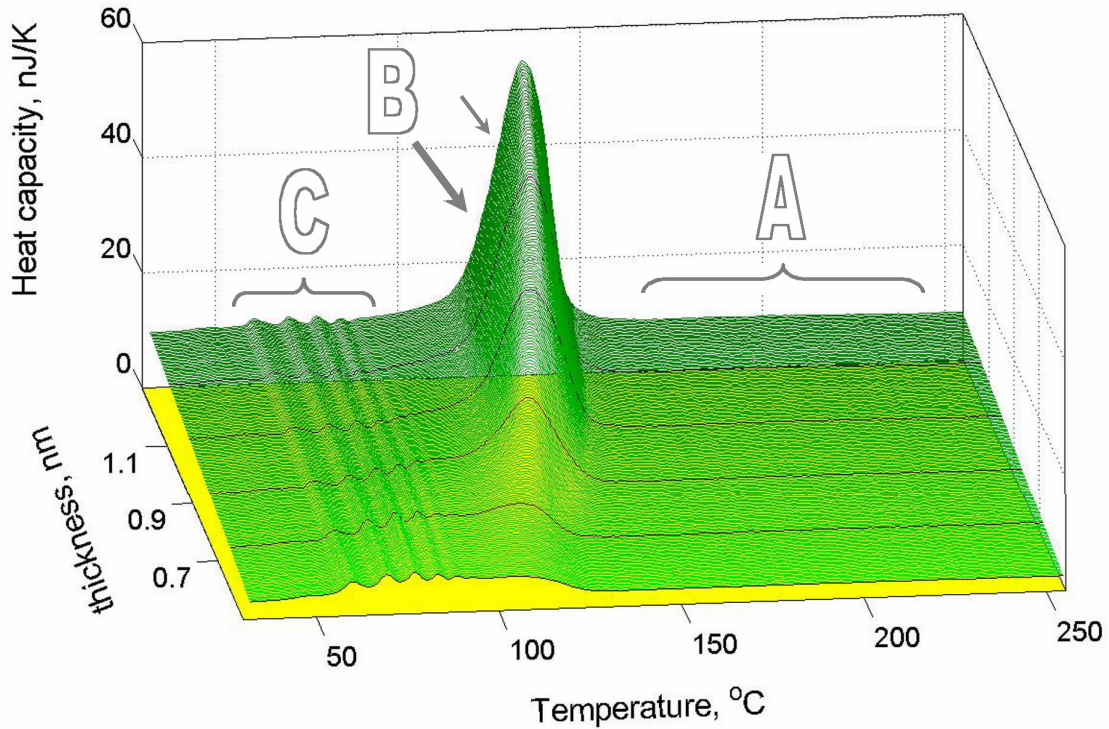


Figure 5-1. 3D plot of heat capacity vs. temperature vs. thickness during the vapor deposition of indium. The plot is generated using sequential individual scans with a heating rate of 30k K/s taken at 1s intervals. The film is discontinuous and consists of nano indium particles. Three distinct features are in the plot. (A) the liquid region which is used to track the growing of thin film on the sub-angstrom scale; (B) the main melting peak of the film which illustrates size-dependent melting; and (C) the multiple maxima, constant in temperature and related to magic number nanoparticles.

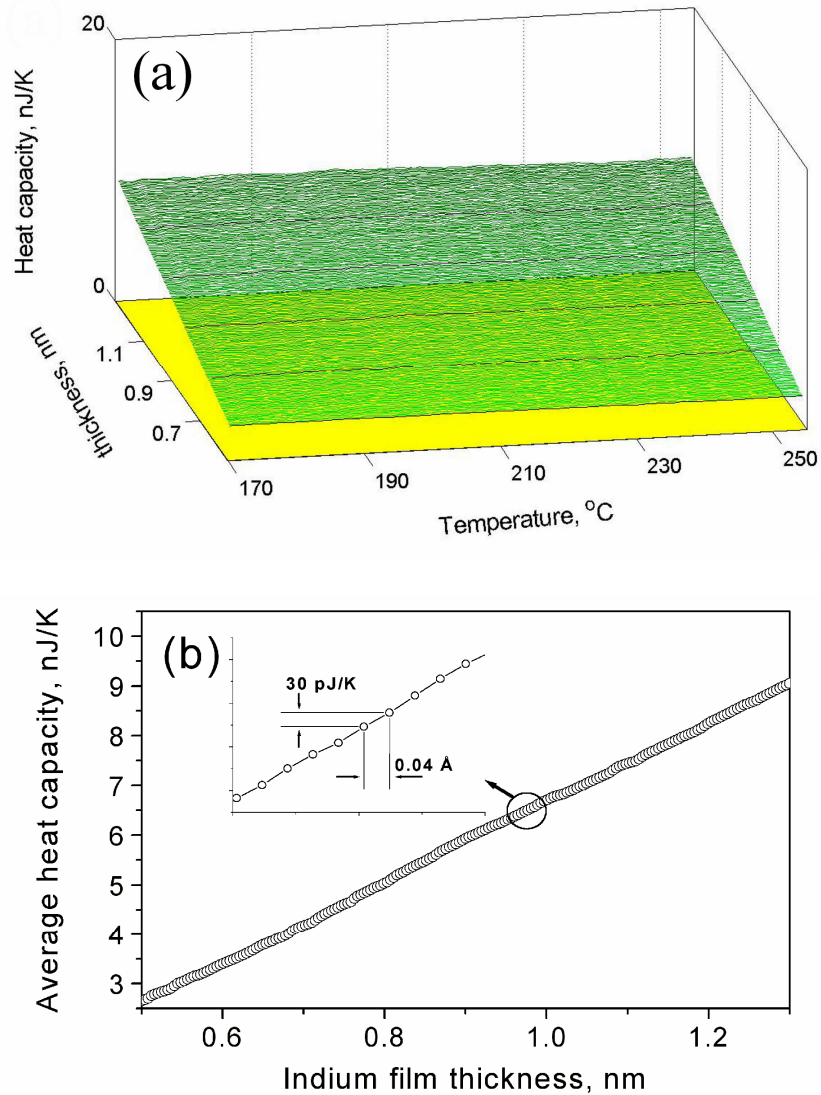


Figure 5-2. (a) Heat capacity of liquid indium (region A in Figure 5-1). For each scan the heat capacity is approximately constant. However, as deposition proceeds the heat capacity of the film increases, as does the mass of the indium; (b) Temperature averaged heat capacity from (a). The inset shows an expanded region of a small section of the main graph. The spacing between adjacent points is 0.04 Å in thickness and 30 pJ/K in heat capacity, illustrating the ultra-fine detail of the technique.

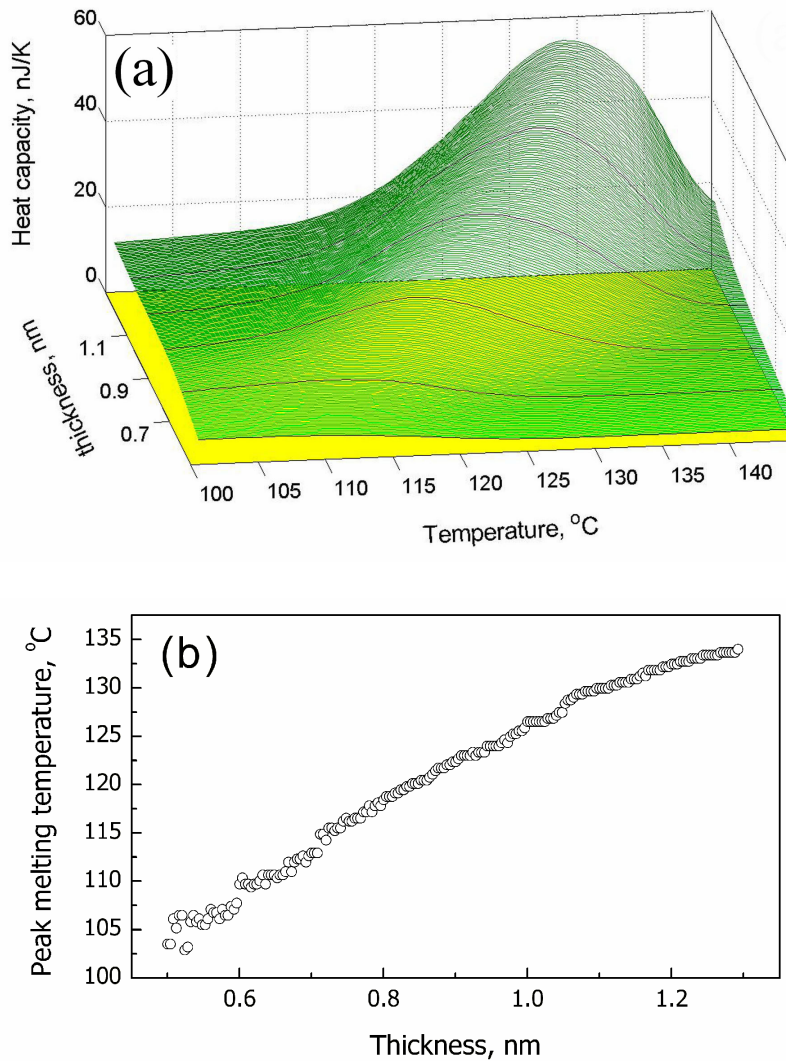


Figure 5-3. (a) The increase of melting temperature during film growth. (b) The main melting peak increases continually from 100 to 135 °C as the integrated film thickness increases from 0.5 to 1.3 nm. This shift is due to the increase of average nanoparticle size. This is an example of melting point depression phenomenon.

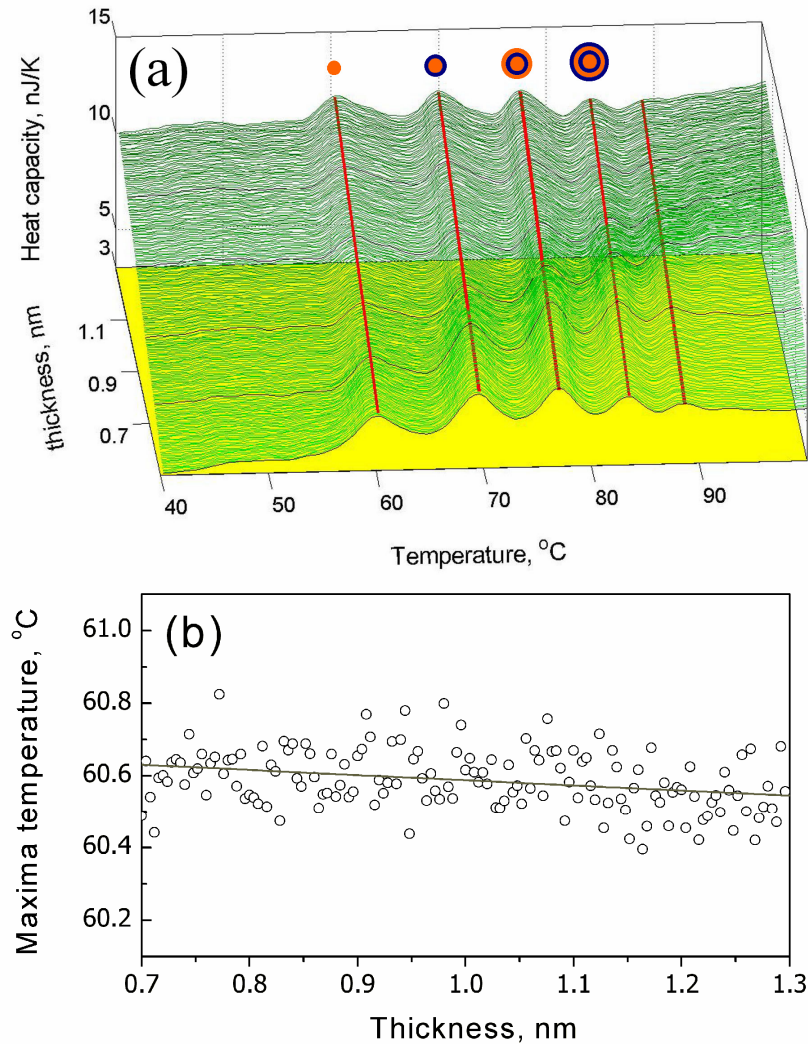


Figure 5-4. At the early stages of deposition, some selected nanoparticles are favored over other sizes due to increased thermodynamic stability. As shown in (a) there are multiple maxima in the caloric curve. The maxima temperature correspond to discrete sizes, which is illustrated as schematic inset of nano particles with incremental atom layers. Unlike the melting peak shift, shown in Figure 5-3, the melting points of selected nano particles are relatively constant. This is seen in (b) where the value of the first maxima in (a) remains at 60.0 ± 0.2 °C. The ability to observe this high degree of stability is due the reduction of systematic errors by the use of real-time measurements.

CHAPTER 6

GOLD SILICIDE FORMATION

This chapter focuses on the study of the phase formation in Au-Si thin films. The structure, thermal and thermodynamic characteristics of the reaction products are determined using nanocalorimetry and ex-situ TEM. In addition, the changes in the thin film during the sequential deposition process are qualitatively tracked in real-time scanning nanocalorimetry. The ultra-fast heating ($\sim 10^4$ °C/s) and cooling ($\sim 10^3$ °C/s) characteristics of the nanocalorimetry device are used to exploit the unusual properties of the Au-Si system — the formation of metastable phases.

The unique finding of this study is the determination of the melting temperature of the metastable phase (~ 300 °C) using calorimetry, which is substantially lower than the equilibrium eutectic melting temperature (363°C) of the Au-Si system. In addition, the heat of fusion (26.4 kJ/mol) of the metastable phase has also been obtained from the caloric measurements. The metastable silicide has been characterized using ex-situ TEM and found to be an orthorhombic phase with $a=0.92$, $b=0.72$, and $c=1.35$ nm, which has been determined by the double tilting experiment using diffraction patterns along major low-index zone axis in stereographic projection. The composition is proposed to be Au_3Si based on EDAX result. The solidification process and supercooling characteristics of the Au-Si sample has also been analyzed using the (rapid) cooling cycle of the nanocalorimetry measurement.

The combination of real-time scanning while depositing the films offers a unique growth process in terms of “deposition temperature”. Clearly, the pulsed-heating/deposition process is

inherent to real-time in-situ nanocalorimetry scanning measurement. It results in a combination of deposition temperatures near ambient temperatures for the majority (~90%) of each 1-sec cycle coupled with temperature excursions above the eutectic melting temperature for brief periods (~1%) of each cycle (See Fig. 6-14). This real-time measurement also allows us to track (in each single scan) the phase formation over a wide range of nominal compositions, extending from gold-rich to silicon-rich.

The real-time experiment shows several interesting phenomena including melting point depression of the eutectic gold-silicon alloy and the competitive growth between the eutectic and the Au₃Si metastable phase. The composition of the film (e.g., “silicon-rich” or “gold-rich”) determines the type of phase that is formed. Rapid cooling experiments reveal that the eutectic is supercooled down to much lower temperature (~135 °C) than that of the Au₃Si phase (~275 °C).

6.1 Introduction

Silicides reactions are of fundamental interest in thin film physics [1]. Issues related to the formation and properties of silicides such as TiSi₂ and CoSi₂ can be critical to device technology [2]. For example the formation of the metastable TiSi₂ C-49 phase was so important to technology that for several years during the mid 1990's there were entire (MRS) national symposia, devoted solely to this topic [3].

Au-Si has been a model silicide system for over 50 years [4]. Metastable gold silicides can be obtained by quenching liquid alloy ($10^3 \sim 10^6$ K/s), ion mixing, vapor deposition or annealing amorphous samples. Major efforts have been taken in interpreting the electron and X-ray diffraction data but still lack consensus on even the basic facts such as the number of possible different silicides. The Au-Si system is apparently susceptible to contamination/growth

problems. Numerous, supposedly different, metastable phases have been reported even under apparently the same experimental condition [4].

Inconsistencies and confusion persists in the literature related to the Au-Si material system in particular in the area of structure analysis. For example, the reference source data bank for standard diffraction analysis (JCPDS) indicates that there are over example “10 different phases” for the metastable gold silicides. However, in 1987 Hultman [5] proposed a single cubic structure (Au_4Si) which can account for most of the reported “different phases” that are listed in the (JCPDS) data bank as separate phases.

The typical difficulties for the experimenters in investigating this material system include the challenges of (1) consistently and controllably growing the metastable phase, (2) identifying the crystal structure from typically complex diffraction patterns, (3) and determining composition of the metastable gold silicide. The challenges are due to nature of the problem, i.e., the complex structure, and limitations of the available experimental techniques. For example, X-ray method is less conclusive in identifying unknown phases when (1) there are multiple complex phases and (2) the quantity of materials is small. Electron beam diffraction is extremely useful in obtaining the symmetry of crystals however, it is less accurate in determining lattice spacing, especially at high-index diffraction planes.

Since Si is extremely susceptible to oxidation, the specific sample preparation process, especially in the thin film type of studies, is critical to the overall control of the experiment. For example, a-Si/Au bilayers easily oxidize, via the process of metal-induced oxidation, at room temperature in just a few days producing thick layers of SiO_2 [6]. Influences from impurity phases in diffraction analyses can be hard to estimate if the sample has not been carefully examined.

Thermal and thermodynamic properties such as the melting temperature and heat of fusion can be in general difficult to measure since the metastable typically decomposes into equilibrium phases before the completion of the measurement and of course this decomposition process is irreversible. Chen and Turnbull attempted to use conventional calorimeter to study the metastable gold silicide melting but their result is preliminary, for example, the reported melting peak is only about 5 °C below the eutectic melting temperature [1].

Nanocalorimeter is a MEMS fabricated thin film device that measures the heat capacity of very small samples at very fast speed [7]. The heating rate can be as high as 10^5 K/s which is useful to avoid the metastable phases decomposition during the DSC scans, thus allowing us to measure the thermal/thermodynamic properties of the sample. Moreover, the nature of a nanocalorimeter can provide a cooling rate at $\sim 10^3$ K/s. Samples can be quenched after melting to form the metastable silicide. The measurement is repeatable.

In the real-time measurement, the nanocalorimetry technique is applied during thin film deposition. The amount of the deposited material increases gradually. The caloric scans are recorded to trace the sample changes.

6.2 Experimental procedure

6.2.1 Evaporation system

The UHV chamber (Perkin-Elmer 430 MBE system) carrying out this experiment has been wet-chemically cleaned and dedicated to gold and silicon deposition. The sample stage assembly has a 12 pin electronic feedthrough with wires and spring-loaded connectors for accessing two nanocalorimeter sensors and one platinum resistor (RTD). The custom-made sample stage (made from aluminum) is loaded on a stainless tube connected to a liquid nitrogen

feedthrough. Cooling water is supplied through the stainless tube to stabilize the sample stage (and the sensor) temperature against radiation heating. The sample stage temperature is monitored by the RTD. On the evaporation source side, the system has been custom engineered with three thermal evaporation sources with water-cooled feedthroughs and screens/chimney. The silicon and gold source are 3 cm apart from each other, and vertically positioned about 30 cm below the sample stage. The designed water-cooled screen/chimney not only prevents cross-contamination between the evaporation sources, but also blocks massive evaporation flux to the chamber, which also decrease excess thermal radiation during the sample growth (see Figure 6-1). The inside chamber has been covered with cryo-shields. They are kept at liquid nitrogen temperature in the experiment to avoid possible contamination.

The thermal evaporation method is employed in order to reduce the noise in the nanocalorimetry measurement. The work heater power supply has a primary transformer that regulates the secondary transformer (2kW 0~20V 0~100A) which supplies the current for the thermal evaporation.

A thick tungsten boat (R. D. Mathis company S3-015W, 0.015 mil thick) is used for silicon evaporation. The width of the boat has been reduced to 0.25 inch by grinding in order to reduce the evaporation power for silicon deposition. In contrast thin tungsten boat (R. D. Mathis company ME5-005W, 0.25 inch wide and 0.005 mil thick; 1.69V 80A 135W at 1800 °C) are used for the thermal evaporation of gold. Small boats are selected to limit the side effect from radiation during the thin film deposition. The pressure is around 3×10^{-10} torr before and after the deposition, better than 2×10^{-9} torr during silicon evaporation, and $< 1 \times 10^{-9}$ torr for depositing gold. The actual deposition rate is 0.4~0.6 Å/s. Using Auger analyses (AES), we didn't detect any contamination from the thick Si samples deposited for calibration purposes.

6.2.2 Nanocalorimetry measurement

The calibrated nanocalorimeter sensors are cleaned by sequentially washing in Acetone, IPA, DI water, and IPA before loading into the chamber. The whole chamber is pumped down and then baked at ~ 170 °C for several days. Before we perform the in-situ nanocalorimetry measurements and deposition, the sensors are pulsed to temperatures exceeding 800 °C several times in order to “flash-clean” the surface. Following the flash process, the sensors are repeatedly heated up to 450 °C several thousand times until the drift characteristics of the sensor is minimized ready for continuous measurements. In the first set of experiments, pure silicon (Alfa Aesar 99.9999%) is first deposited and followed by one set of nanocalorimetry measurement to determine the amount of silicon (or, the thickness). Usually about 4 nm silicon is deposited to cover the surfaces controlled by the shutter with a calibrated crystal monitor nearby. Continuously, pure gold (Alfa Aesar 99.9999%) is deposited while the caloric scans are taken in real-time to record the phase formation. During each caloric scan, the Au-Si sample is heated up to 450 °C within 12 ms, and subsequently quenched down to ~ 10 °C (i.e., the sample stage temperature during the experiment, monitored by the on-stage RTD). The caloric scans are repeated at 1 second interval.

Since the deposited thin film increases the heat capacity of the sample caloric cell, the final highest heating temperature gradually decreases. The real-time nanocalorimetry measurement and the deposition have to be interrupted at several thicknesses in order to compensate for this effect by increasing the heating current for the sample sensor.

6.2.3 TEM analysis

At excess gold regime, there is only one peak in caloric curves which can be attributed to the gold silicide melting. Regular caloric scan with/without cooling measurement is recorded after the deposition. By comparing the caloric data, we find that this gold silicide is stable over weeks inside the vacuum chamber and air exposure over one hour doesn't make noticeable change to the gold silicide sample. With this knowledge, the samples are ex-situ transferred into Philips CM12, JOEL2010LaB6 or JOEL2010F microscopes. Bright field, dark field, selected area diffraction (SAD), STEM and EDAX analyses have been used to study the gold silicide. The diffraction analyses use the standard polycrystalline gold pattern as the calibration. The single tilt experiment is first done right after breaking the vacuum without further preparation. The double tilt experiment is done afterwards by taking off the sample and gluing it onto a regular copper grid (room temperature, air dry). Bright field and diffraction analyses show no observable change of the sample. Finally the EDAX analysis is carried out to determine the gold to silicon atom ratio (stoichiometry). The gold heater and silicon nitride membrane are first removed by a three-minute ion milling process. Although decomposition is observed in some grains due to the ion bombardment, partially supported sub-micron gold silicide crystals with "zero background" (confirmed by the same diffraction patterns before and after the ion milling) have been obtained to do the composition analysis by EDAX.

6.2.4 Sample alignment

Nanocalorimetry desires that the entire sample aligned underneath the heater. An alignment mask can do this. However, strong background from the metal heater is not convenient for TEM analysis. In order to compromise, a notch area is opened on one side of the mask. The

notch is less than 2% of the total sample area (2.565 mm²). In addition, the shadow effect due to the separation of the evaporation sources, the mask and the nanocalorimeter sensor frame thickness (250 μm) (i.e., non-overlapping portion of the deposited silicon and gold) can be limited by properly arranging the geometry between evaporation sources and the orientation of the sensor with the alignment mask (Figure 6-1(b)). The additional error is estimated to be 2~3%.

6.3 Result and discussion

The equilibrium phases of the gold-silicon system are the liquid, the fcc terminal solid solution of Au with limited solubility of less than 2 at.% of Si, and the diamond-type cubic terminal solid solution of Si with negligible solubility of Au ($\sim 2 \times 10^{-4}$ at.%). The phase diagram is of a simple eutectic form (see Figure 6-2). The experimental work starts with either the pure silicon or pure gold, and then deposits the gold or silicon as much as possible in order to cover the whole range of the system. Note that the sample can aggregate after being melted during the deposition so that the actual composition can be different from the nominal composition. Also, extra silicon or gold may present in the sample.

6.3.1 As-deposited sample

Figure 6-3 is a set of TEM micrograph and diffraction patterns of an as-deposited Au/Si sample. The gold layer is first deposited on to an ultra-thin (20 nm) amorphous silicon nitride membrane. The thickness is about 13.7 nm. The deposited gold forms an almost continuous film. Silicon is then deposited afterwards on the top of gold film. The thickness is about 29.1 nm (see the bright field image shown in Figure 6-3(a)). The sample is kept under UHV conditions for

one day and half hour in air transfer before the TEM analyses. From previous experiences based on Auger analysis, an oxidation layer quickly forms on the fresh silicon surfaces once it exposes to the air, the oxidized layer is about 3 nm thick and quite stable afterwards. The SAD pattern (Figure 6-3(b) reveals that the as-deposited film consists poly-crystalline gold (characteristic fcc diffraction patterns with $1/R^2$ ratio of 3:4:8:11:12...) and amorphous silicon (the halo inside the smallest gold ring). Note that the diffused halo is contributed from both amorphous silicon and amorphous silicon nitride. The intensity profile of the diffraction pattern is also shown in Figure 6-3(c). The highest sample temperature (due to the radiation) is about 100 °C for several minutes.

6.3.2 Low temperature annealed Au/Si sample

In the notch area (Figure 6-1(b)) ~20 μm away from heater, one can start to observe continuous gold-silicon film. Figure 6-4 shows the morphology and diffraction analysis on an area that is about 100 μm away from the heater, where the sample was repeatedly annealed by the heating pulses (where the temperature is estimated between 100 and 270 °C). The sample is Si(3.7nm)/Au(15.7 nm). The bright field image shows the poly-crystalline Au-Si sample with the grain size normally about 20 nm (see Figure 6-4(a)). Figure 6-4(b) and 6-4(c) are the SAD analysis of the sample compared with a standard gold crystalline sample as well as a quenched Au-Si sample corresponding to a metastable phase (details are presented later sections). The conditions of the microscope are exactly the same for these three diffraction micrographs (only the sample height is changed to do the focus on the samples).

Hultman et. al. studied the microstructures of gold-silicon samples on a 20~30 nm thick silicon nitride membrane [5]. The as-deposited thin film sample shows that intermixing between the gold and silicon happens at room temperature because the Au (111) diffraction splits into two

lines, Au (200) deflection is not observable, and the Au (220) diffraction line becomes the strongest. They attribute this to the (111)-preferred orientation. However, Figure 6-3 clearly show that our as-deposited film consists polycrystalline gold and amorphous silicon. While the observation in Figure 6-4 is quite similar to Hultman's result, i.e., Au (200) is not observable and Au (220) has the strongest intensity. Comparing Figure 6-4(b) and 6-4(c), one can see that the annealed sample is more likely a "new" phase rather than the textured gold. The sample temperature during the deposition probably is the key factor for such observations.

The importance of the above discussion lies that the same gold silicide phase can also be obtained by annealing thin films (i.e., the solid reaction), which is not limited to the quenched samples studied in the section 6.3.5.

6.3.3 The caloric result on deposited silicon layer

In order to investigate the gold silicide, it is important to know the amount of silicon before the next step gold deposition. The caloric result shows the sample heat capacity as a function of the temperature. When $T \gg \Theta_D$ (Debye temperature), one can calculate the sample mass using the measured heat capacity to divide the specific heat capacity (close to constant) because the heat capacity is an extensive parameter of materials [8]). Θ_D of silicon is about 362 °C. Therefore the specific heat capacity can not be considered as constant in the scanned temperature range. The best method to obtain the mass of the silicon is to correlate the caloric result with the calculation using the literature data. Although it has been reported that specific heat capacity is slightly different between amorphous and crystalline silicon [9], such influence is negligible to the experimental results. Both the caloric curve and the simulated one are shown in Figure 6-5. The best match between the measurement and theory generates the silicon mass of

22.2 ng (0.79 n mol) for this sample which is important for calculating thermodynamic parameters in section 6.3.11.

6.3.4 In-situ real-time observation of phase formation

Figure 6-6 shows the real-time nanocalorimetry results during the gold deposition. The surface has originally been covered with a silicon layer of 3.7 nm thick. The early stage of gold silicide formation during the gold deposition is presented. The deposition is performed in a 160 seconds period. Totally 5.9 nm thick gold is deposited, controlled by the crystal monitor. The sample is fast heated up to ~ 400 °C in 12 ms and then passively quenched to ~ 15 °C at one second interval during the real-time measurement (with the radiation). Without the thermal radiation, the sample temperature is around 10 °C.

At the very beginning stage of deposition, caloric scans show almost flat heat capacity curves up to ~ 1 nm thick of gold. The heat capacity increases and the highest temperature decreases indicating the gold mass increases. Followed, a very broad melting peak starts to show up at ~ 290 °C. It becomes sharper as more and more gold adds to the sample (peak B). Also, the melting peak temperature shift towards the high temperature direction. Later, a second peak appears at lower temperature (~ 270 °C) and gradually grows (peak A). The gradually appeared melting peaks further decreases the final heating temperature because the phase change holds the temperature during the process.

It is hard to analyze the early deposition region where no melting peak is present. In separate experiments, once the shutter is closed to block the deposition flux and radiation, one can observe the gradually appeared melting peak, which can be a complex combination that

possibly involves detailed physics like deposition, radiation, nucleation, supercooling, etc. An amorphous or liquid mixture layer could be proposed for such observation.

The evolution of Peak B is very similar to those in metal nanoparticles melting [7, 10]. The smaller materials melt at lower temperatures than that of the bulk. The depressed melting temperature is proportional to the reciprocal of the size. Thus the smaller the material, the lower temperature it melts. Reciprocal relationship also determines that the melting peak is broad for smaller size samples. Peak B finally approaches to 363 °C, where Au-Si eutectic melts.

Figure 6-7 shows the micrographs of Si(3.7nm)/Au(4.3nm) sample prepared under the similar experimental conditions described in Figure 6-6. Caloric results show that melting peak B dominants. Figure 6-7(a) is a bright field image of the sample. The sample consists of crystalline silicon and crystalline gold, which have been confirmed by the diffraction patterns. Silicon is plate like while gold can be large or small particles in between or attached to the silicon. High-Angle Annual Dark Field (HADF) images (so called ‘z-contrast images’) [11] are collected in this study. The intensity of the scanned micrograph is roughly proportional to the z^2 , where z is the atomic number of the element. The atomic numbers are 14 for the silicon and 79 for the gold. Therefore, such analysis can study how the heavy gold element distributes in the sample in detail (Figure 6-7(b)). The result shows that large silicon plates can have random arranged gold rich regions on surfaces. Figure 6-7(c) presents a high-resolution image of an example of one gold rich region on the silicon plate. Lattice images from Au (111) and Si (111) planes have been resolved with the inter-plane spacing of 0.234 nm and 0.316 nm, respectively. Existence of such small gold on top of silicon corresponds to the initial broad melting peak B (eutectic), which further confirms that it is a size dependent phenomenon. Figure 6-7(d) is a bright filed image taken from a Au(13.7 nm)/Si(29.1 nm) sample that shows mostly the bulk

behaved eutectic (where gold is deposited first, large particles are formed after pulse heating, and silicon is deposited afterwards.). Clustered sub-micron gold and silicon grains have been observed, which corresponds to the melting peak B at bulk melting temperature.

Solely gold continuous deposition experiment does not show any melting peak at the scanned temperature range, although it has been reported that gold nanoparticles have dramatically melting point depression below 100 °C [12]. The possible reasons might be that the deposited gold atoms and clusters are movable on the surface during the pulse heating. Coalescence or ripening happens so that the size that determines the particle melting is not be small enough for the gold [13].

The experimental results reveal that the peak B in the caloric curves is from the gold-silicon eutectic. The eutectic has shown the melting point depression that is size-dependent.

Continuing the experiment initiated in Figure 6-6, one can see the competing growth between the Au-Si eutectic (peak B, equilibrium phase) and a metastable phase (peak A) during the further gold deposition. The caloric results are shown in Figure 6-8. The real-time measurement is recorded from 8.8 to 15.7 nm thick of gold.

One can see clearly that the originally strong melting peak (B) in Figure 6-6 starts to decrease and finally disappears as the gold deposition proceeds. At the same time, the melting peak A continuously increases. After peak B vanishes, only melting peak A exists in the caloric curves. Adding more gold does not basically make any change to peak A.

In equilibrium, gold and silicon forms eutectic alloy (363 °C, 18.6 at. %). The terminal solutions are fcc gold with limited solubility of silicon in gold (less than 2 at. %), and diamond-type cubic silicon with negligible solubility of gold ($\sim 2 \times 10^{-4}$ at. %). Therefore, the observed melting peak A is from one quenched metastable phase (melting peak at 303 °C). From Figure 6-

6 and 6-8, one can also notice that there is also melting point depression for the metastable phase, since the shift in the melting peak temperature is much beyond experimental uncertainty and other possible instrumentation influences.

6.3.5 Identifying the metastable phase

At present time, the experiments unavoidably need to transfer samples in air to do the TEM analyses. The metastable phase is possibly subject to change due to the oxidation, or contamination associated decomposition that has to be examined before the TEM operations. This can be done by verifying the caloric curves taken before and after air exposure for the same sample or comparing the characteristic diffraction patterns. Although no obvious change has been observed in the samples, large grain crystals (sub-micron size) have been analyzed instead of very small features to avoid extraneous effects. The air transfer time is limited with in 10 minutes for the TEM operations

Figure 6-9 shows TEM images of the quenched Si(3.7nm)/Au(15.7nm) sample that corresponds to the metastable phase (melting peak A). Figure 6-9(a) is a low magnification bright field image showing a large area morphology of the sample in the notch area shown in Figure 6-1(b). The edge of gold heater is indicated in the figure. Agglomerated sub-micron particles nearby the gold heater are the interested gold-silicon samples presented in Figure 6-9(b). Figure 6-9(c) is the corresponding diffraction patterns of the sample. Ten diffraction patterns from different sample areas have been added together to generate this picture because of the physical size of the available diffraction aperture in the TEM and limited sample areas (see Figure 6-9(a)). As one can see from Figure 6-9(c), the diffraction pattern is from a complex

crystalline structure. The lattice parameter is larger than that of Au. However, it is hard to extract all the quantity information from this figure because the amount of the sample is not enough.

The standard technique to identify a phase from diffraction techniques is to compare the observed diffraction patterns with the simulated ones and find the best match with the smallest unit cell dimensions [14]. However, the details are quite different depending on the sample and the method. X-ray is accurate for simple single phase bulk sample powder diffraction analyses, but less powerful dealing with multiple unknown phases or complex large unit cell structures, where the low angle diffraction information is not available and the high angle diffraction can have too many diffraction peaks. Unfortunately, most of the quantitative x-ray studies on the gold silicide were done in 70's by the old type of Debye-Scherrer diffractometers using the films. Possible experimental error is not traceable. Similarly, the polycrystalline diffraction analysis using the TEM can also obtain diffraction patterns, but the result is less accurate. Low angle information is preferred in electron diffraction method. A careful study needs either internal or external references. In the later case, the operation should not change the microscope intensity, magnification, and focus condition. Moreover, one has to be aware that electron dynamic distortion can also limit its accuracy especially in high angle regime. Examples of such x-ray and electron diffraction investigations can be found in earlier references [5, 14-16].

The investigated samples in this work are only tens nanometers thick, 0.45 mm wide and 5.9 mm long. Such small amount of material is not suitable for x-ray analyses. Electron diffraction method has the similar problem since the quantity of the sample in this work is quite limited, which has been illustrated in Figure 6-9. Therefore, the better way to study the metastable phase is to do the double tilting experiment.

Double tilting experiment studies the structure of the crystal by recording the relationship between major diffraction zone axes. It can be used to construct the three dimensional crystalline structure, by obtaining diffraction patterns along major low-index zone axis in stereographic projection. Such method prefers large single crystals due to the tilting operation. For smaller grains, the intensity of the Kikuchi patterns is not very strong, therefore it can be hard to find the major zone axes to perform the double tilting experiment. In this work, relative large crystals are investigated. Since the crystals are random oriented, the experiment needs to find those particles whose major diffraction zone axes are close to the electron beam. Only pieces of partial stereographic projection from multiple grains can be recorded using the JOEL 2010 microscope because maximum tilting angle is quite limited ($\pm 30^\circ$). A critical double tilting experiment was done on a Philips CM12 microscope with large tilting angles ($\pm 50^\circ$). The same grain has been tilted from [001] to [011] and from [001] to [101] diffraction zone axes. This direct observation suggests an orthorhombic structure for the sample. All the pieces of partial stereographic projection further collaborated this result. The electron diffraction analyses indicate that all the examined samples are from an orthorhombic phase.

Figure 6-10 is the diffraction results from the orthorhombic phase. The crystalline structure agrees with the b-centered orthorhombic unit cell with $a = 0.92\text{nm}$, $b = 0.72\text{ nm}$, $c = 13.5\text{ nm}$. Diffraction patterns corresponding to zone axes [100], [001], [101], [011], [111], [121] have been presented for illustrations. The b-center can be inferred from Figure 6-10(b). The diffraction pattern has regularly spot at $h+l=2n$ and the spot extinguishes at $h+l=2n+1$ where n in an integer. Notice the different extinguishes between the first and the second Laue zones, showing a b-center in the a-c plane. Similar effect can also be observed in Figure 6-10(e).

One basic problem in gold-silicon binary system studies is whether the prepared sample has only one phase or has multiple phases. This is the origin of the disagreement in early bulk x-ray works represented by Luo (β and γ phase) [17], Predecki (γ -brass structure) [18], Anderson (δ phase) [15], Suryanarayana (A13 or β -Mn type structure) [14]. Except for the eutectic alloy, the investigated samples are all metastable phase. Few other experimental methods [1] can provide assistant information to clarify the situation.

Depositing gold film on top of silicon and followed by annealing samples at elevated temperatures is another type of experiment among gold silicide studies. LEED combined with Auger analyses have been used. Green and Bauer [19] observed three different LEED diffraction patterns, but they can not conclude whether these diffraction patterns belong to the same phase or separate phases. Moreover, unlike common techniques in x-ray and electron diffraction analyses, possible error in LEED experiment is more difficult to estimate.

Experiments involving both silicon and gold deposition need special concern. Generally speaking, the inherent surface conditions may cause differences between a thin film sample and the bulk. However, such type of experiment has to solve the contamination problem mostly from the silicon deposition. This can be seen in sensitive nanocalorimetry measurements. Typical peaks due to contamination happen at ~ 100 , ~ 250 , and ~ 320 °C when the experiment is carried out in an oil system with background pressure of 2×10^{-8} torr and middle 10^{-7} torr during the silicon deposition (5~10 at.% contamination from carbon and oxygen by Auger analysis). The exact role of contamination in the gold silicide is not clearly understood. Structure analyses become extremely challenge if the impurity phases have to be excluded but their information is unknown. Krutenat also mentioned similar problem [16] where small copper contamination was

found in the obtained sample possibly by the sputtering of the water lines nearby the target. The influence seems negligible but detailed discussion is not available.

Technically speaking, bulk silicide studies are cleaner than thin film methods. However, detailed experimental procedures might have introduced contamination but have not been checked in early work, for example, the way of quenching method and how to prepare the x-ray power diffraction sample from the quenched metastable phase. Such information is seldom mentioned in the literature. The difference in the diffraction details can be either from gold silicide, texture, or impurity phases. This can definitely influence the phase identification and cause the disagreement between different research groups. The gold on silicon wafer study is supposed to have less contamination than that in gold silicon thin film studies, since the quality of silicon deposition is critical. However, the structure analyses can be difficult since the sample quantity is quite limited.

From Figure 6-6 and 6-8, one can see that there is one melting peak (A) corresponding to the metastable phase. Melting peak B is from the eutectic alloy. Only melting peak A exists at “gold-rich” regime. Therefore, the stereographic projection method can be used to identify the crystalline structure of this metastable phase. Gaigher and Van de Berg [20] did double tilting experiment on gold silicide. The sample was prepared by e-gun evaporation, dissolving the NaCl substrate in water, and then analyzed by in-situ heating. They found that parts of the results agree with the previous model proposed by Suryanarayana and Anantharaman [14] (x-ray method), and attributed other diffraction patterns to a new phase with orthorhombic unit cell ($a=0.68$, $b=0.75$, and $c=0.96$ nm). However, there still have several diffraction patterns that can not be indexed. The experimental result in this work is from stereographic projection and double tilting experiment. All the diffraction patterns can be attributed to one orthorhombic phase with

as long as caloric results show only melting peak A. The observation also agrees with Green's LEED result within the possible experimental error [19], which proposes that three different LEED patterns in Green's work be due to different orientation rather than different metastable phases.

6.3.6 Stoichiometry

Complexity of the gold silicide metastable phase is also reflected by the disagreement on stoichiometry of the metastable phase. Example of proposed compositions are: $\text{Au}_{2.5}\text{Si}$ (29 at.% Si) [21], Au_3Si (25 at.% Si) [15], $\text{Au}_{3.3}\text{Si}$ (23 at.% Si) [16], Au_4Si (20 at.% Si) [5], Au_5Si (17 at.% Si) [14], Au_7Si (13 at.% Si) [17]. As one can see that the gold silicide exists in 13~29 at.% of Si range. From Au_3Si to Au_5Si , the difference is only within a few percent. Such small difference is usually within the experimental uncertainties.

There are three types of estimations for the gold silicide composition. (1) Direct method, to use the original weight of silicon and gold [14, 22]. (2) In direct method, to deduce the composition from possible structure or super lattice, or to compare with other metal silicides [5, 17, 23]. (3) Direct method, to measure the composition from experiments using wet chemistry [15] or surface analytical technique [19]. This work uses EDAX to determine the stoichiometry of the gold silicide metastable phase in TEM. "Zero background" samples are obtained by short time ion milling to remove the silicon nitride membrane and gold heater. Partially supported submicron crystals have been analyzed. The result suggests the gold to silicon ratio of 3 on 1.

Caloric analyses also support such result. In Figure 6-8, the gold thickness corresponding to where the eutectic melting peak disappears is around 11.5 nm (3.7nm of silicon). In case of Au_3Si , the gold thickness should be 9.4 nm; in case of Au_4Si , the gold thickness should be 12.6

nm. Since the film is discontinuous, excess gold can stay between the silicide islands. Au_3Si is then reasonable.

Various stoichiometry reported in literature can be explained by solid solutions. The solid solution based on the Au_3Si matrix may contain excess of gold since the eutectic composition is about Au_4Si . If the sample has been quenched, it can also have vacancies. This model can explain some disagreements in the literature. In Suryanarayana's experiment, a metastable phase was observed in gold-silicon samples from 15 to 25 at. % of silicon. The authors suggested Au_5Si (16 at.% of Si) phase partially due to crystalline models and partially influenced by other research groups [14, 17, 24]. No excess silicon was mentioned in the 25 at.% Si sample. George et. al. [22] also reported obtaining Au_3Si phase without excess gold or silicon. A solid solution model can explain all these experimental observations. However, there has no quantitative experimental proof to verify or reject this hypothesis.

6.3.7 Epitaxial relation

Epitaxial growth is not surprise in gold silicides. Philofsky et. al. [25] reported the epitaxial growth of eutectic alloy on silicon substrates. Green et. al. [19] also suggested the possibility of epitaxial growth based on the experimental observation that gold silicide layer forms at gold silicon interface as well as on the surface of gold film after annealing.

Over saturating the sample with excess of gold does not basically change the melting behavior of the metastable phase from caloric observations, but does change the morphology of the sample. Figure 6-11 is a STEM (z-contrast) image of the Si(3.5nm)/Au(64nm) sample. Since the gold silicide has light silicon atoms, the HADDF intensity is lower than that of the gold. Combining with electron diffraction and EDAX analyses, one can further confirm that the

islands have gold in the center and gold silicide on the shell or skin (if not fully covered). The gold core does not melt during the heating. Therefore it can serve as nucleation site for the silicide growth. Under such conditions, epitaxial growth can happen. Figure 6-12 shows an example proof of such observations, with Au[111]//Au₃Si[100]. Roughly a 4-time relation has been observed. The lattice parameter $a=0.92$ nm with is quite close to 4 times of $d_{\text{Au}(111)}$ (0.94nm). The mismatch is only about 2%. Seibt et. al. [23] presented a high resolution TEM image showing the epitaxial growth of silicide between the gold grains, but it is difficult to determine the epitaxial relation from their work because the sample is not aligned to the major diffraction zone axis and the size of the silicide grain is too small to do a thorough structure analysis. Both Seibt et. al. [23] and this work observed epitaxial growth of the silicide with the present of gold. In this work, 4 time is the most common epitaxial relation, while 3 and 5 time relations are also observed. Moreover, epitaxial growth is not required for all the silicide observations with excess gold. Note that the silicide is gold rich. The sub-unit cell of the silicide can be close to the gold. This is the physical reason of the epitaxial relation between the silicide and the gold.

6.3.8 Growth model

To sum up above observations and analyses, one can propose the following model for the experiments (shown in Figure 6-13).

- 1) A layer of silicon film is first deposited on the silicon nitride membrane.
- 2) First several monolayer thick gold atoms on top of silicon form a mixed layer. Since no melting peak has been observed at this stage, the mixed layer might be amorphous or liquid during the continuous gold deposition.

- 3) The eutectic and the Au₃Si metastable phase form, showing size-dependent melting (beginning) and competitive growth (later).
- 4) Finally the Au₃Si metastable phase dominates as more and more gold added.
- 5) Further depositing gold changes the morphology of the sample. The liquid alloy expels excess gold to the gold core before solidification. Thus the metastable phase is shell or skin like on the surface. Since the gold core acts as nucleation site, epitaxial growth of the metastable phase can be observed.

Exchange the gold and silicon will get reversed result, i.e., the metastable phase first appear when silicon first deposits on gold layer, but the eutectic finally dominate the growth at silicon rich regime. However, there is still a small metastable phase peak that can not be totally removed by extra silicon deposition.

The experiment reveals that the composition determines metastable phase, eutectic alloy or both of them will exist in the quenched gold-silicon sample.

6.3.9 Cooling experiment

To study the physical reason of the obtained experimental results, one has to investigate the cooling process on the samples.

Figure 6-14 shows the heating and cooling experimental results of the samples with only the metastable phase and the metastable phase plus the eutectic. Cooling curves are obtained by applying very small current (1~5mA) through nanocalorimeter sensor to measure the temperature drop as a function of time. Such small current does not heat the sample too much (tens degree °C estimated) [26]. The measurement is very noisy so that a higher quality signal, differential voltage, is recorded to present the changes due to the sample. The derivative of the differential

signal (raw data) is presented in the plots with no baseline subtracted. The derivative of the differential voltage according to time is proportional to the caloric curve [26]. When this experiment was carried out, only 100 ms maximum scan was available. The second set of plots showing two peaks is from an experiment where the alignment mask is removed. The signals are much wider due to the non-uniformity of the nanocalorimeter sample cell, but much faster cooling rate is achieved to record the lower temperature physical change of the sample.

As one can see that the melting peak at ~ 303 °C and cooling peak at ~ 275 °C are from the metastable phase; the melting peak at ~ 363 °C and cooling peak at ~ 135 °C are from gold-silicon eutectic. It is clear that eutectic has much stronger supercooling (~ 230 °C) than that of the Au_3Si metastable phase (~ 30 °C). This is reasonable since the liquid alloy needs to separate the silicon and gold before the solidification (see Figure 6-7(d)). The eutectic consists of sub-micron size silicon and gold crystals.

Cooling experiments can explain why the system does not undergo a solidification process after the Au_3Si phase melting which is 50 °C below the eutectic melting temperature — the liquid is supercooled. In fact, we would expect an exothermic solidification peak after or accompanying the metastable phase melting (303 °C) and then a much larger endothermic eutectic melting peak at 363 °C in a “slow” calorimetry measurement.

6.3.10 Models on phase formation

Experimental results show that composition of the film, i.e., “gold-rich” or “silicon-rich” determines the quenched sample to form either Au_3Si phase or eutectic (illustrated in Figure 6-15). There can have two models to explain the experimental observations based on the different hypotheses on “gold-rich” or “silicon-rich”.

The first model explains the phase formation in terms of the nucleation and growth. Since the metastable phase is gold-rich (Au_3Si), the excess gold in the sample that doesn't melt can serve as nucleation sites for the Au_3Si phase. Therefore, one can obtain the metastable phase. On the other hand, gold is immiscible to silicon. In the "silicon-rich" samples, the excess solid silicon tends to receive silicon rather than the silicon plus the gold, therefore, one would expect the separation of silicon and gold (see Figure 6-7(d)).

The second model, however, hypothesis that the liquid is slightly different. Castanet and Bergman [27] proposed that there are Au_3Si -type aggregates in the liquid gold-silicon alloy. The aggregates would strongly stabilize the liquid phase. The proposed composition of the liquid aggregates is the same as that in the identified gold-silicon metastable phase. Therefore, the competitive growth between the eutectic alloy and the metastable Au_3Si phase observed in this work can be considered as a direct result of the difference in the liquid alloys. In "gold-rich" region, the aggregates dominate so that it is easy to form the metastable phase. In "silicon-rich" region, aggregates are small in quantity so that the liquid alloy can be further supercooled, to segregate into silicon and gold, and then to solidify. Somewhere in between, the competition growth happens, determined by the composition of the sample.

Both models can explain the experimental observations in this work. Model 1 is straight forward and easy to understand, however, the details on nucleation and growth process has to be further investigated, for example, if the solid gold is of necessary for the Au_3Si phase formation or not; Model 2 is also interesting — it directly relates the liquid and solid phase, in such a deep eutectic system, but the correlated understandings in the literature has not jet been fully established.

6.3.11 Thermodynamic properties

The caloric curves not only indicate the melting temperature, but also provide heat of fusion information (area under the melting peak). At the gold excess regime, there is only one metastable peak in the caloric curve. Therefore, it can be utilized to calculate the heat of fusion, assuming that all the deposited silicon has been consumed to form the metastable phase, and excess gold does not melt. The first assumption is valid when excess gold is used to saturate the sample. The second assumption is properly because gold tends to form large particles that can not be melted in the experimental scanned temperature range, which has been proved in a separate gold deposition experiment.

Figure 6-16 shows three caloric curves from the regular nanocalorimetry measurement. Results from two separate experiments are presented. The silicon is 0.79 and 0.75×10^{-9} mol respectively. In the later experiment, two gold thicknesses (47 and 64 nm) have been examined. The broadening of the melting peak is the result of thicker samples. However, the area under the peak (heat of fusion) is about the same ($20.80 \mu\text{J}$ for 0.79×10^{-9} mol and $20.07 \mu\text{J}$ for 0.75×10^{-9} mol sample). The experimental result gives an averaged heat of fusion of 26.4 kJ/mol for the Au_3Si phase assuming Au_3Si as a molecule. This value is equivalent to 6.6 kJ/mol in terms of 1 mol of total atoms, which is quite close to the previously reported value (6.1 kJ/mol) by Chen and Turnbull [1]. Chen's experiment was done 36 years ago, using an old type of calorimeter Perkin-Elmer DCS-1. The measurement was carried out at 40 K/min , while the most sensitive range was $\sim 10 \text{ K/min}$. Moreover, the metastable sample decomposes during the measurement. Therefore the measurement was indirect. Few experimental data on metastable phases are available in the literature and this is only one of the examples.

The heat of fusion of eutectic has also been estimated. Figure 6-17 is an example caloric curve showing both metastable phase and eutectic melting peaks. If one assumes that silicon is either in the Au_3Si phase or in the eutectic, then the specific heat of fusion of the eutectic can be calculated. The total amount of silicon has been measured (see section 6.3.3). The specific heat of fusion of the Au_3Si phase can be used to determine the silicon is in the Au_3Si phase. By subtracting corresponding amount of silicon in the Au_3Si phase, one can then calculate the specific heat of fusion for the eutectic. The result is about 9.6 kJ/mol of Si, which equals to 1.9 kJ/mol for the eutectic. The value is smaller than the bulk value from Turnbull (9.8 kJ/mol) [1] and Castanet (9.4 kJ/mol) [27], which suggests that some silicon remains in this sample.

Theoretical calculation can also be used to estimate the result. From the Hess cycle, one can calculate the specific heat of fusion of the eutectic alloy. The specific heat of fusion is 50.21 kJ/mol [28] for the silicon and 12.72 kJ/mol for the gold [28]. The liquid heat of mixing at ~20 at.% Si is 7.31 kJ/mol [4]. If the difference in liquid and solid heat capacity is negligible, the specific heat of fusion of the eutectic should be about 12.4 kJ/mol.

6.4 Conclusion

The structure and thermal/thermodynamic properties of the Au_3Si metastable phase and the Au-Si eutectic have been studied. The competitive growth between the Au_3Si phase and the eutectic has been observed and found to be determined by the composition of the sample. The experiment also shows the melting point depression of the Au_3Si phase and the eutectic. Rapid cooling experiments indicate the eutectic is supercooled down to much lower temperature (~125 °C) than the Au_3Si phase (~275 °C). Models on the thin film sample growth as well as phase formation have been discussed.

6.5 References

1. Chen, H.S., Turnbull D., *Thermal Properties of Gold-Silicon Binary Alloy near the Eutectic Composition*. Journal of Applied Physics, 1967. **38**(9): p. 3646.
2. Mayer, J.A., Lau, S. S., *Electronic Materials Science: For Integrated Circuits in Si and GaAs*. 1990, New York: Macmillan Publishing Co. 476.
3. *Materials Research Society Symposium Proceedings Volume 402. Silicide Thin Films -- Fabrication, Properties, and Applications*, ed. R.T. Tung, Maex, K., Pellegrini, P. W., Allen, L. H. 1996, Pittsburgh, PA: Materials Research Society.
4. Okamoto H. and Massalski, T.B., *Phase diagram of Binary Gold Alloys*. 1987: ASM INTERNATIONAL. 266.
5. Hultman, L., Robertsson, A., Hentzell, H. T. G., Engstrom, I., Psaras, P. A., *Crystallization of amorphous silicon during thin-film gold reaction*. Journal of Applied Physics, 1987. **62**(9): p. 3647.
6. Allen, L.H., private communication.
7. Lai, S.L., Guo, J. Y., Petrova, V., Ramanath, G., Allen, L. H., *Size-dependent melting properties of small tin particles: nanocalorimetric measurements*. Physical Review Letters, 1996. **77**(1): p. 99-102.
8. Burns, G., *Solid State Physics*. 1990: Academic Press, Inc.
9. *Properties of Amorphous Silicon and its Alloys*, ed. S. T. 1998: INSPEC, the Institution of Electrical engineers, London, UK.
10. Zhang, M., Efremov, M. Yu., Schiettekatte, F., Olson, E. A., Kwan, A. T., Lai, S. L., Wisleder, T., Greene, J. E., Allen, L. H., *Size-dependent melting point depression of nanostructures: Nanocalorimetric measurements*. Physical Review B, 2000. **62**(15): p. 10548-10557.
11. Browning, N.D., Chisholm, M. F., Pennycook, S. J., *Atomic-resolution chemical analysis using a scanning transmission electron microscope*. Nature, 1993. **366**: p. 143.
12. Buffat, P., Borel, J. P., *Size effect on the melting temperature of gold particles*. Physical Review A, 1976. **13**(6): p. 2287-98.
13. Venables, J.A., Spiller, G. D. T., Hanbucken, M., *Nucleation and growth of thin films*. Reports on Progress in Physics, 1984. **47**: p. 399.
14. Suryanarayana, C., Anantharaman, T. R., *On the crystal structure of a non-equilibrium phase in the gold-silicon system*. Materials Science and Engineering, 1974. **13**: p. 73.

15. Andersen, G.A., Bestel, J. L., Johnson, A. A., Post, B., *Eutectic Decomposition in the Gold-Silicon system*. Materials Science and Engineering, 1971. **7**: p. 83.
16. Krutenat, R.C., Tien, T. K., Fornwalt, D. E., *Sputter deposition of a Metastable Phase in the Au-Si system*. Metallurgical Transactions, 1971. **2**: p. 1479.
17. Luo, H.L., Klement, W. Jr., Anantharaman, T. R., *Effects of Liquid Quenching on the Constitution and Structure of Silver-silicon and Gold-Silicon Alloys*. Transaction of the Indian Institute of Metals, 1965. **18**: p. 214.
18. Predecki, P., Giessen, B. C., Grant, N. J., Trans. Metall. AIME, 1965. **233**: p. 1438.
19. Green, A.K., Bauer, E., *Formation, Structure, and Orientation of Gold Silicide on Gold Surface*. Journal of Applied Physics, 1976. **47**(4): p. 1284.
20. Gaigher, H.L., Van der Berg, N. G., *The Structure of Gold Silicide in Thin Au/Si films*. Thin Solid Films, 1980. **68**: p. 373.
21. Von Allmen, M., Lau, S. S., Maenpaa, M., Tsauro, B. Y., *Phase Transformations in Laser-irradiated Au-Si Thin Films*. Applied Physics Letters, 1980. **36**: p. 205.
22. George, D.K., Johnson A. A., Storey, R. J., *Preparation of the Metastable Compound Au₃Si by Quenching Liquid Droplets of a Au-25 at.% Si Alloy into Water*. Materials Science and Engineering B, 1998. **55**: p. 221.
23. Seibt, M., Buschbaum, S., Gnauert, U., Schroter, W., *Nanoscale Observation of a Grain Boundary Related Growth Mode in Thin Films Reactions*. Physical Review Letters, 1998. **80**(4): p. 774.
24. Dixmer, J., Guinier, A., Mem. Sci. Rev. Met., 1967. **64**: p. 53.
25. Phillofsky, E., Ravi, K. V., Brooks, J., Hall, E., *Phase Transformation in Eutectic Gold-Silicon alloys on Single-Crystal Silicon*. Journal of Electrochemical Society, 1972. **119**(4): p. 527.
26. Efremov, M.Y., Olson, E. A., Zhang, M., Zhang, Lai, S. L., Schiettekatte, F., Z. S., Allen, L. H., *Thin-Film Differential Scanning Nanocalorimetry: Heat Capacity Analysis*. Thermochemica Acta, 2003: p. submitted.
27. Castanet, R., Bergman, C., *Heat Capacity of Au_{0.805}Si_{0.195} Liquid Alloy*. Ann. Chim. Fr., 1979. **4**: p. 419.
28. *CRC Handbook of Chemistry and Physics*. 78 ed. 1997, Boca Raton, N.Y.: CRC Press.

6.6 Figures

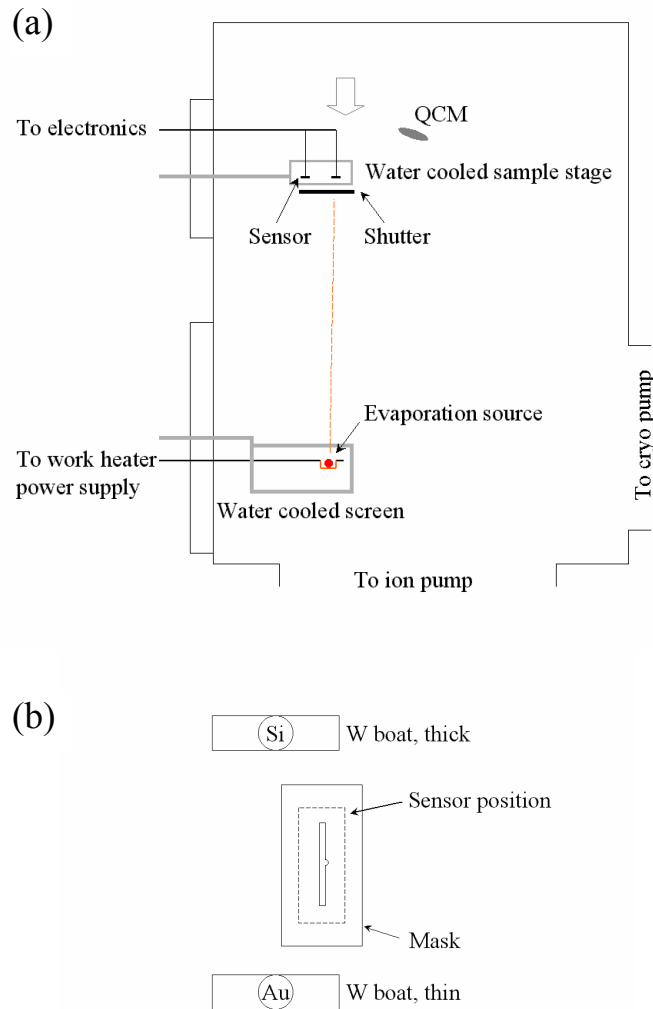
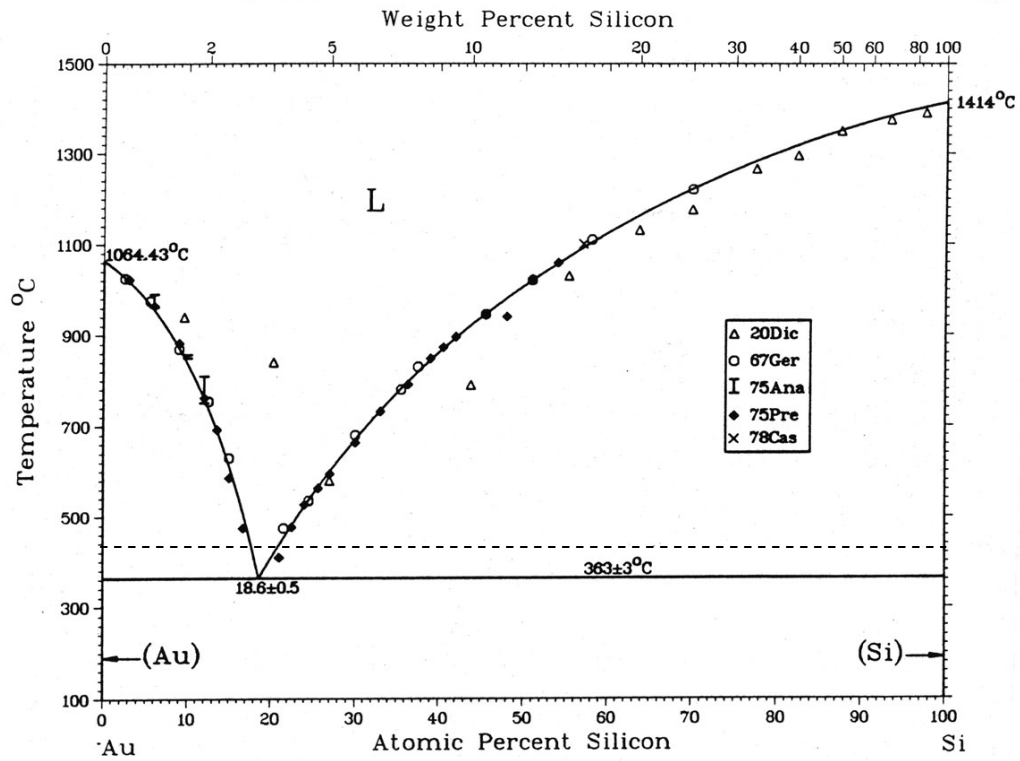
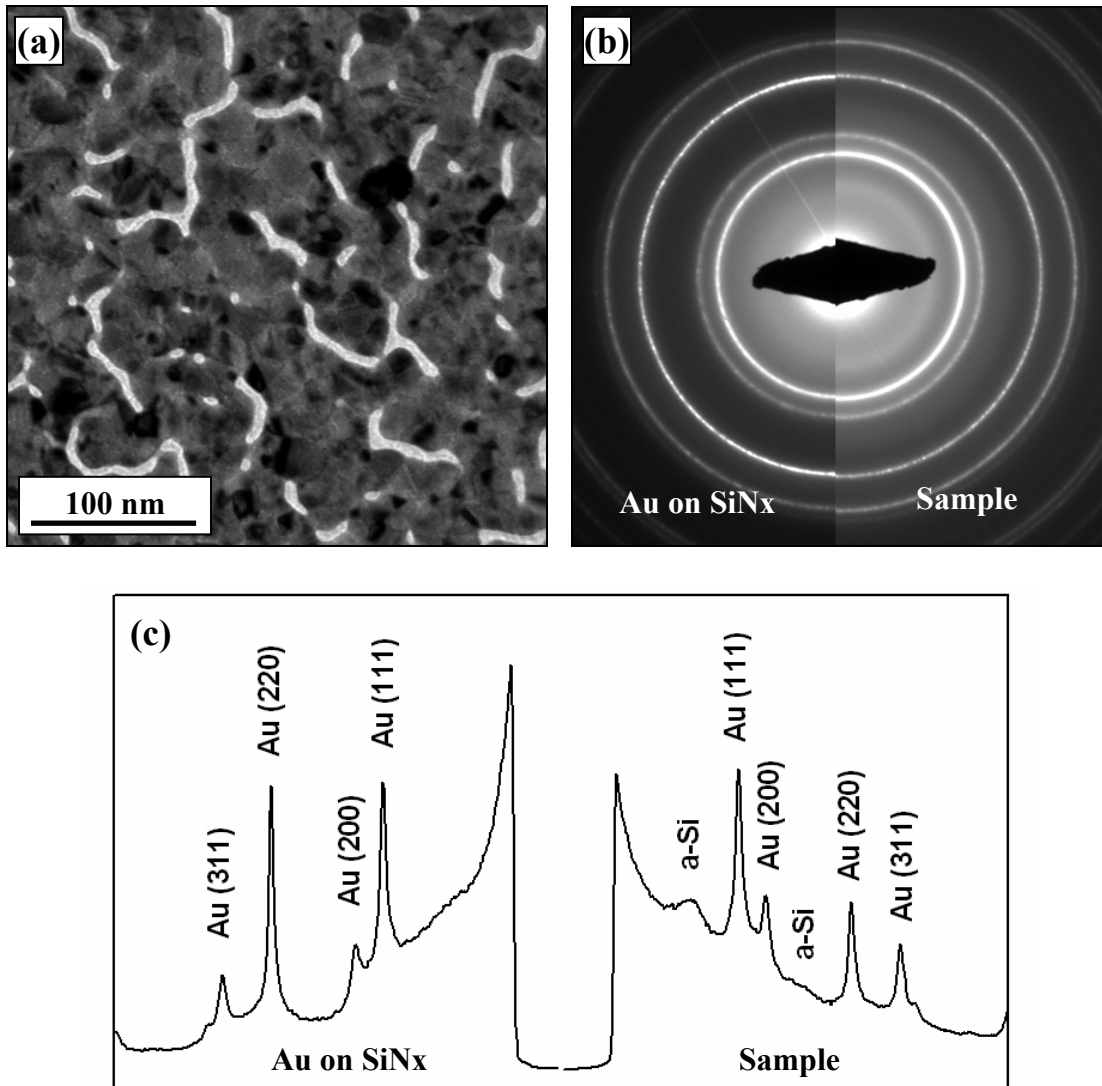


Figure 6-1. The illustration of the custom optimized UHV chamber. (a) The system uses thermal method to evaporate silicon and gold. The vertical distance between the evaporation sources and the sensor stage is ~ 30 cm. The thickness is controlled by the shutter with a calibrated crystal monitor. (b) The top view as indicated from the arrow in (a) shows the arrangement of evaporation sources and the sample sensor. The configuration minimizes the possible non-overlapping problem due to applying a shadow mask.



H. Okamoto and T.B.

Figure 6-2. Au-Si equilibrium phase diagram (after H. Okamoto and T. B. Massalski, 1987). The dashed line indicates the highest temperature in nanocalorimetry scans.



Intensity Profile

Figure 6-3. (a) The TEM bright field image of the as deposited Au(13.7nm)/Si(29.1nm) sample on a 20nm thick silicon nitride membrane. (b) The SAD pattern reveals that the sample consists of poly crystalline gold and amorphous silicon. The intensity profile of the SAD pattern is shown in (c).

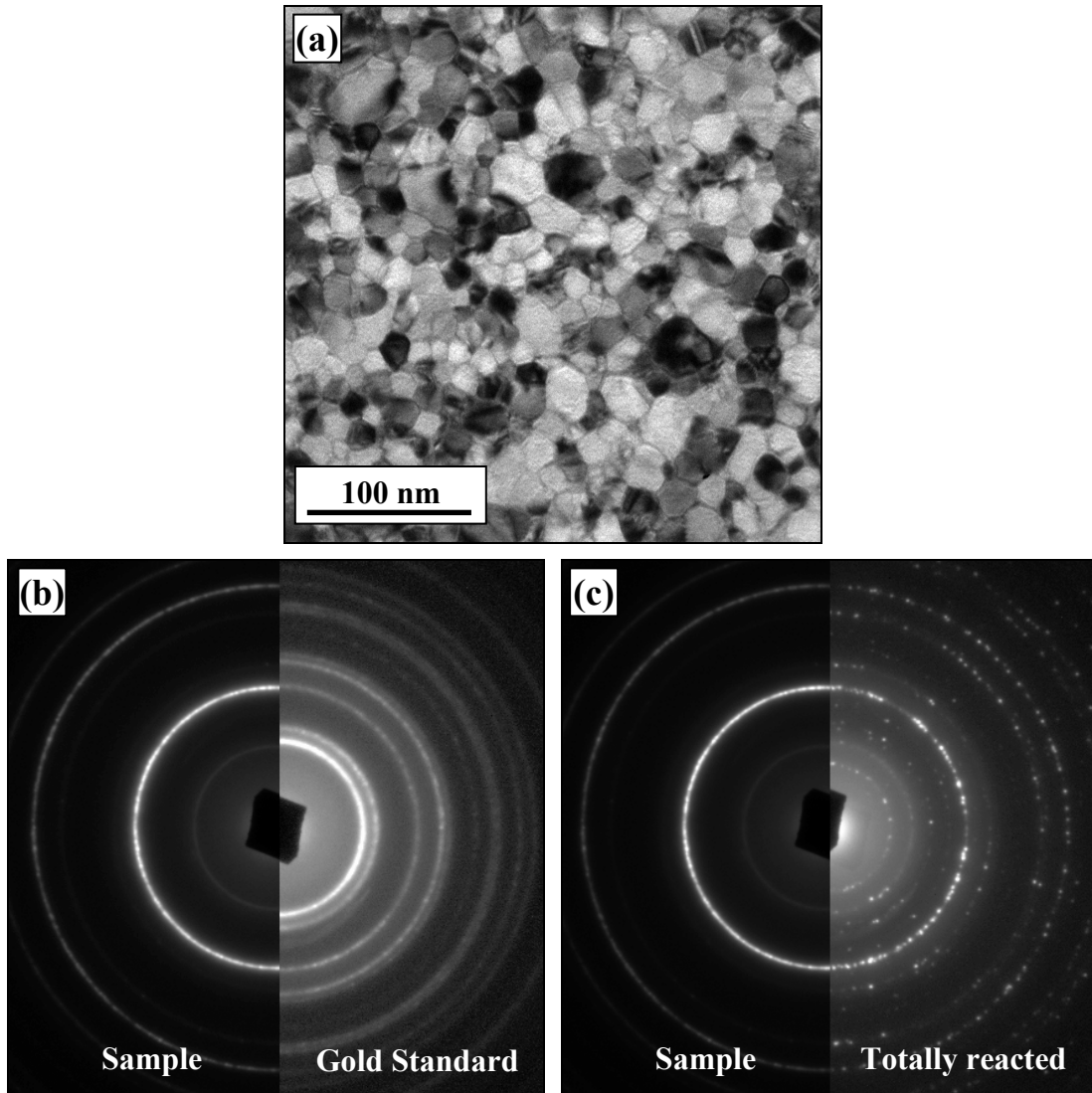


Figure 6-4. The TEM analyses on the Si(3.7nm)/Au(15.7nm) sample influenced by heating. (a) The bright field image of the sample. The SAD pattern of the sample is compared with the patterns from a standard poly crystalline gold sample (b) and a reacted gold-silicon sample (c).

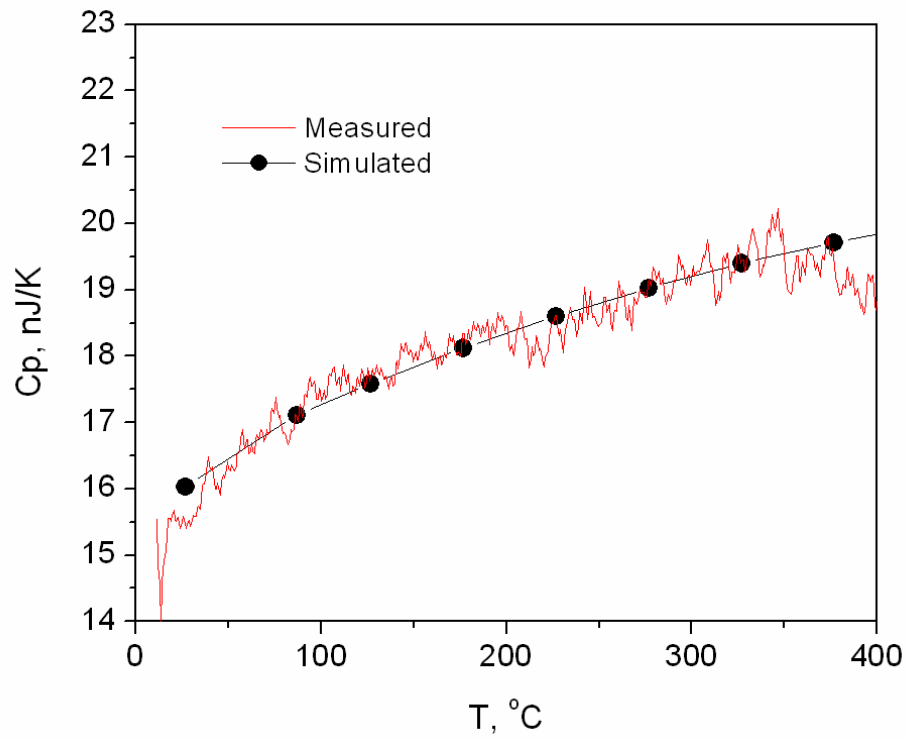


Figure 6-5. Using caloric curve to determine the amount of deposited silicon on the sensor. The silicon mass (or thickness) is obtained by correlating the measured heat capacity curve with a calculated one from the specific heat capacity.

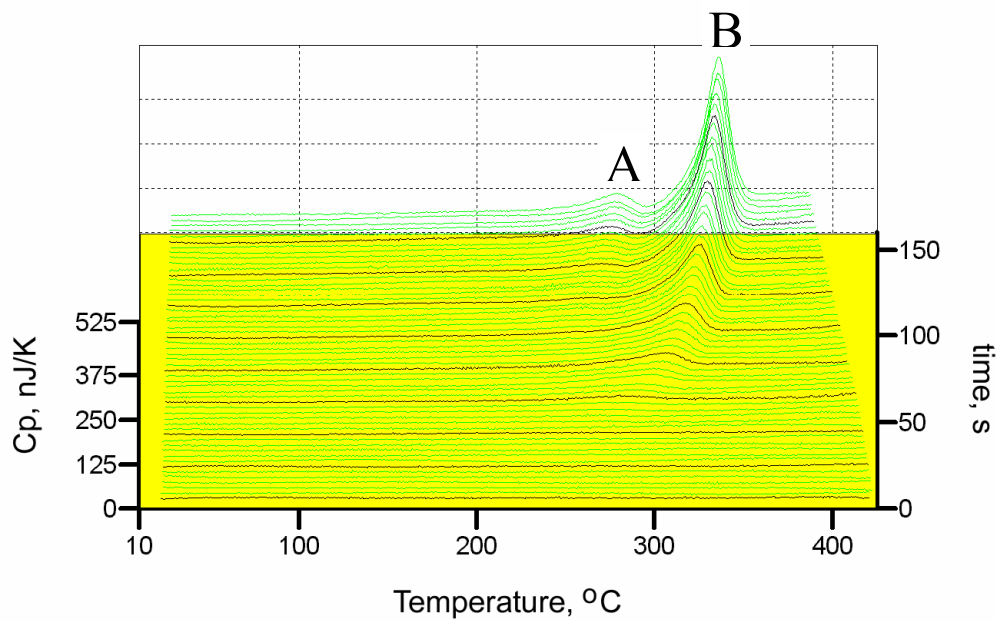


Figure 6-6. The real-time nanocalorimetry results during the gold deposition. The surface has originally been covered with a 3.7 nm thick silicon layer. Totally 5.9 nm gold has been deposited. First ~ 1 nm gold adding to the surface only increases the heat capacity of the sample. Afterwards the evolution of two melting peaks has been observed. The melting peak B is from gold silicon eutectic alloy. The melting peak A is from a metastable phase. Both the eutectic alloy and the metastable phase show melting point depression in the early stage of thin film growth.

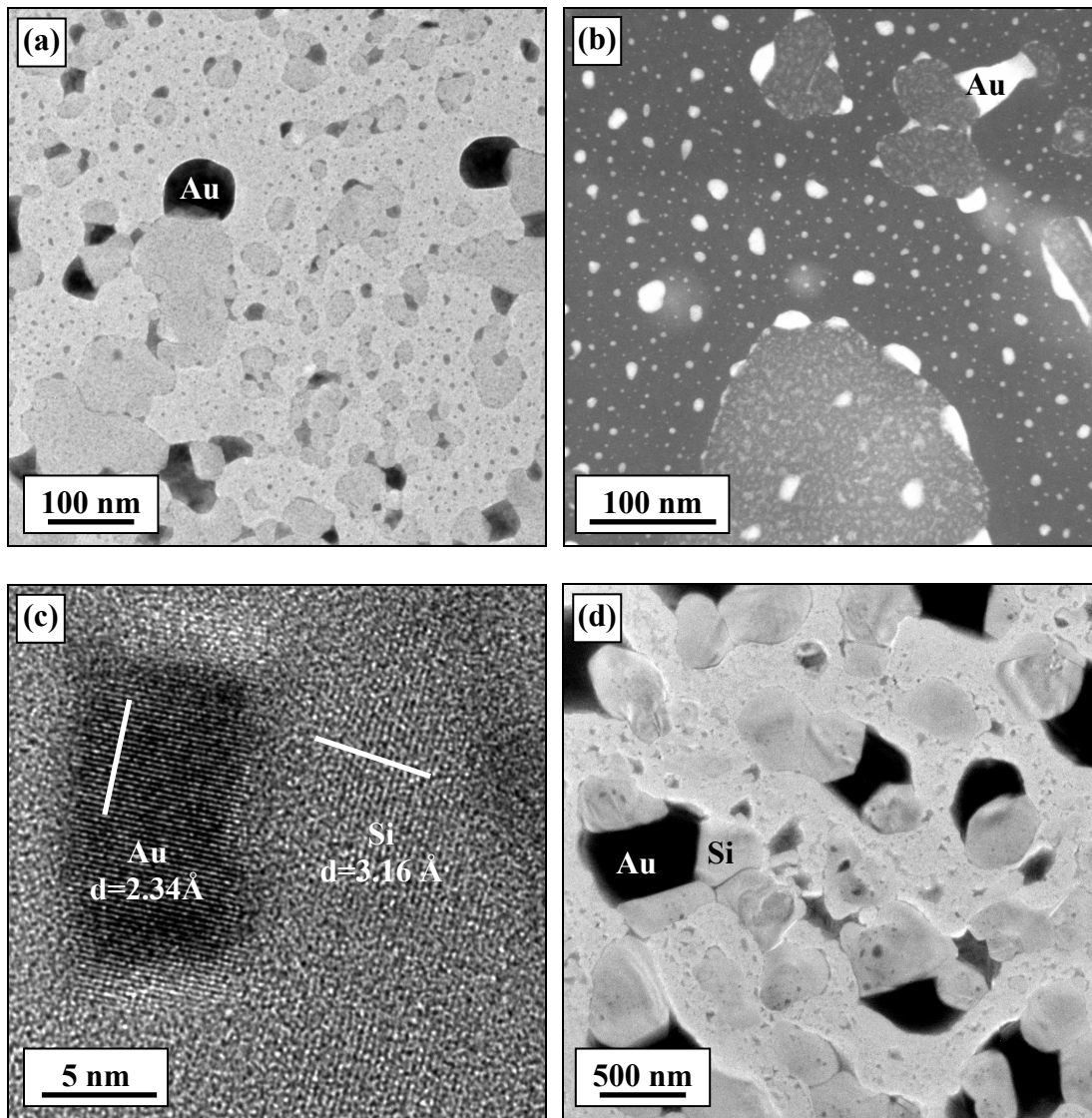


Figure 6-7. TEM Analyses of the Si(3.7nm)/Au(4.3nm) sample prepared under similar experimental conditions described in Figure 6-5 where melting peak B dominates. (a) A bright field image of the sample. Silicon is plate like while gold can be large or small particles in between or attached to the silicon. (b) A STEM (z-contrast) image showing the locations of the gold (bright features). (c) A high-resolution image of one gold rich region on the silicon surface showing the gold and silicon lattice images. (d) A bright field image of bulk behaved gold-silicon eutectic.

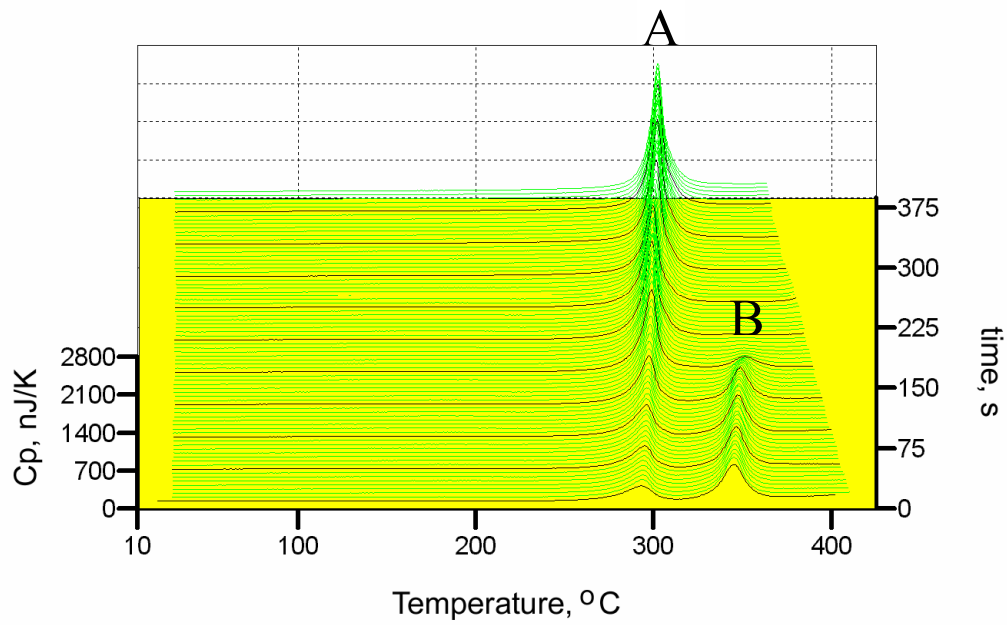


Figure 6-8. Continuing experiment initiated in Figure 6-6. Competitive growth between the gold-silicon eutectic alloy (peak B) and the metastable phase (peak A) has been observed in the real-time gold deposition. As more gold deposited on to the surface, the metastable phase dominates.

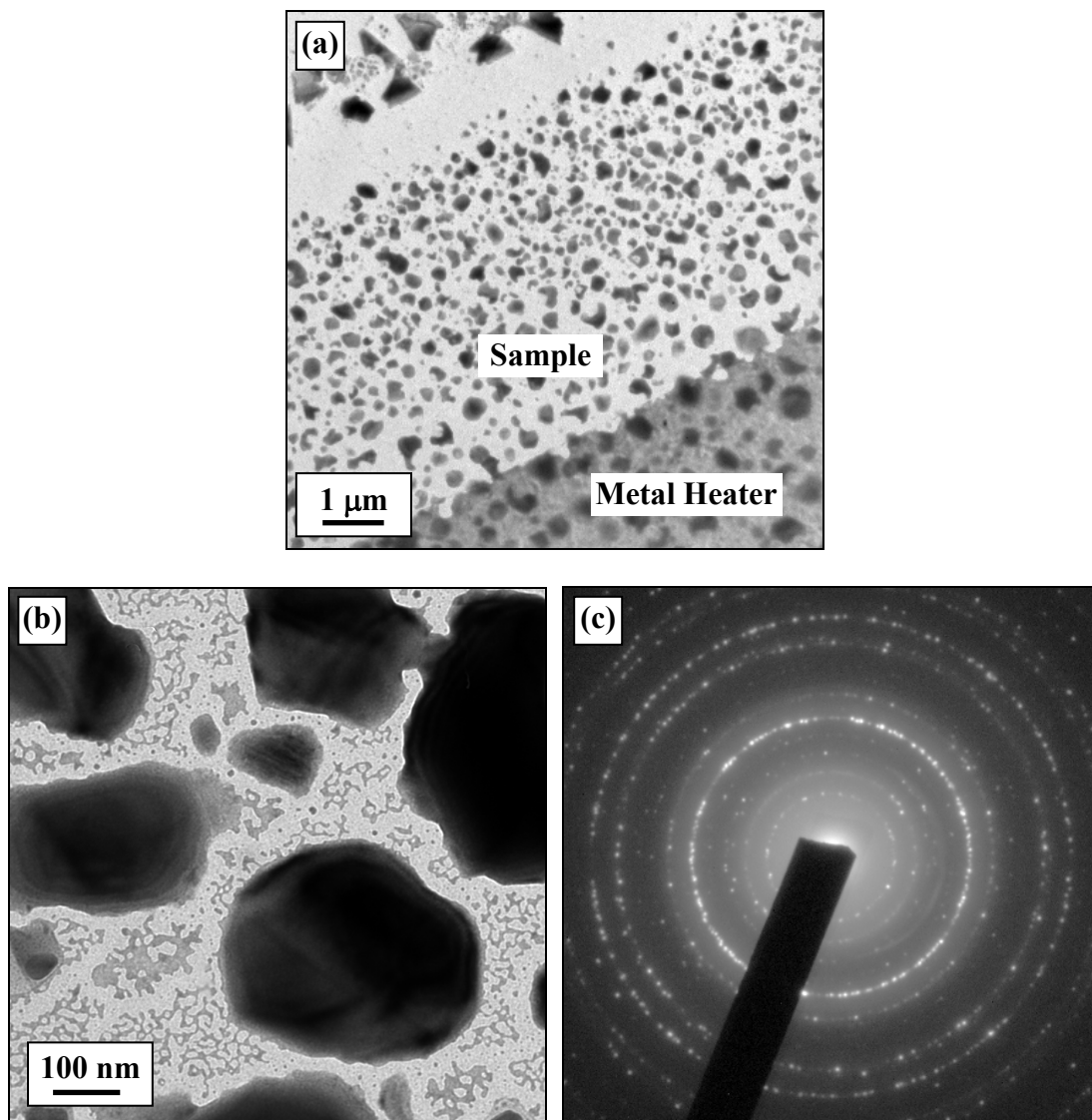


Figure 6-9. The TEM images of the repeatedly quenched Si(3.7nm)/Au(15.7nm) sample that corresponds to the metastable phase (melting peak A in Figure 6-6 and 6-8). (a) The low magnification image shows the large area morphology of the sample. (b) The agglomerated sub-micron particles nearby the metal heater are the interested gold-silicon samples. (c) The SAD pattern of the sample reflects a complex crystalline structure.

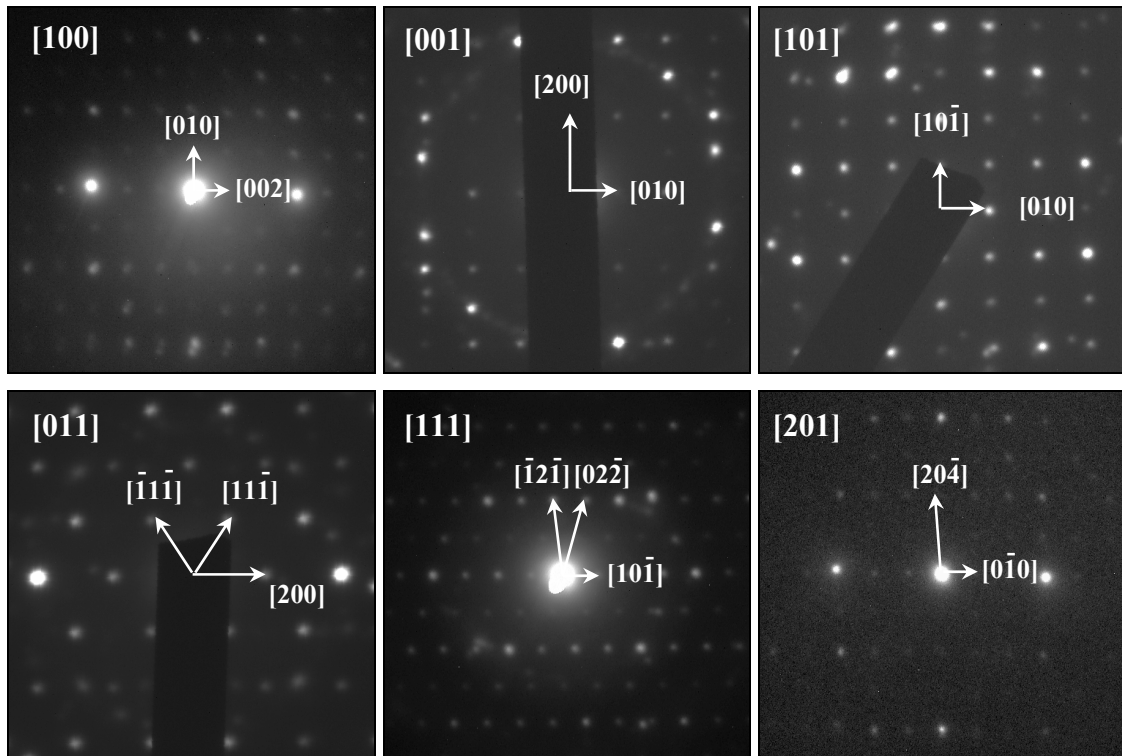


Figure 6-10. The double tilting experimental results on the gold-silicon metastable phase. The diffraction patterns are consistent with a B-centered orthorhombic unit cell with $a=0.92$ nm, $b=0.72$ nm, $c=13.5$ nm. The diffraction patterns corresponding to zone axes $[100]$, $[011]$, $[101]$, $[011]$, $[111]$, $[201]$ have been illustrated.

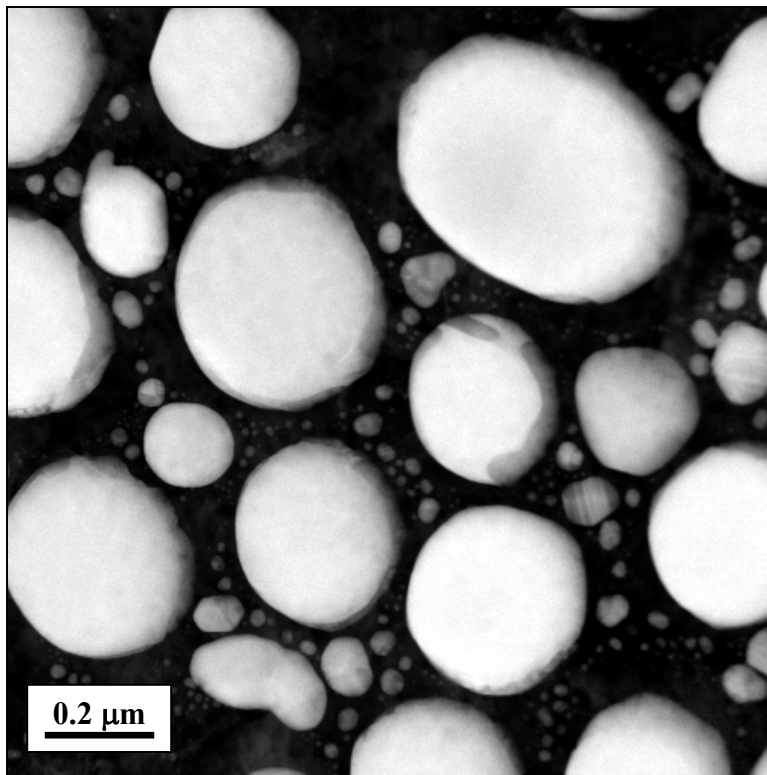


Figure 6-11. A STEM (z-contrast) image of the Si(3.5nm)/Au(64nm) sample. Since the gold-silicide phase has light silicon atoms, the density is lower than that of the gold. One can clearly see that majority of the gold is in the center and silicide is on the shell or skin like.

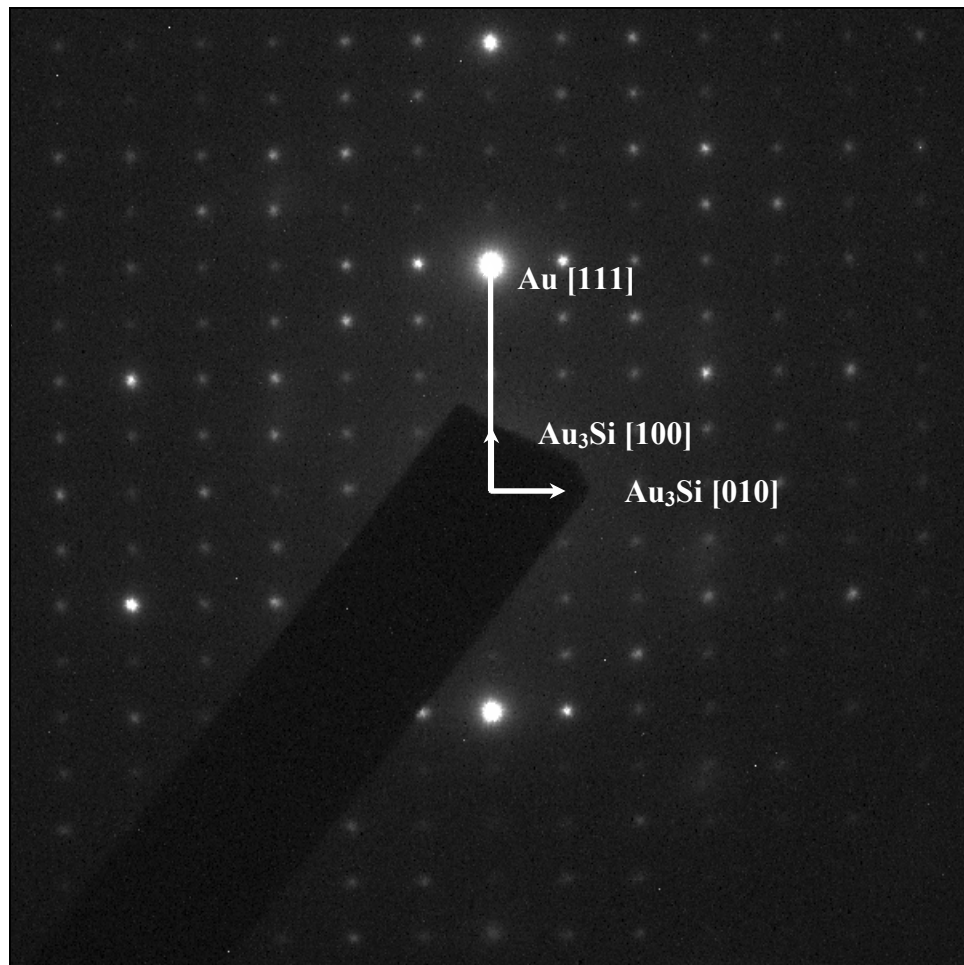


Figure 6-12. The strong epitaxial relation between the gold and the silicide is illustrated. The SAD pattern shows Au[111]/Au₃Si[100]. A roughly 4 time relation has been found.

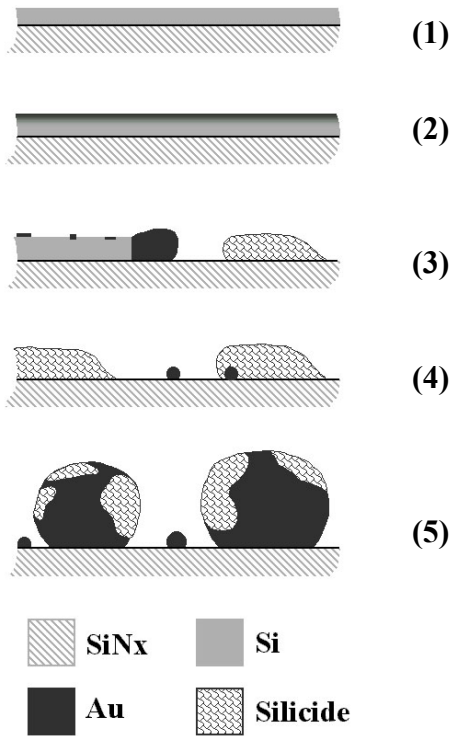


Figure 6-13. The proposed model for real-time deposition experiment described in Figure 6-6 and 6-8. (1) A layer of silicon film (4nm) is first deposited on the silicon nitride membrane. (2) First several monolayers gold on top of silicon forms a mixed layer. No melting peak has been observed at this stage. (3) The eutectic (melting peak B) and metastable phase Au_3Si (melting peak A) form, showing size-dependent melting (beginning) and competitive growth (later). (4) Finally only Au_3Si phase presents at gold-rich region. (5) Further depositing gold changes the morphology of the sample. The liquid expels excess gold to the solid gold core before solidification, thus the Au_3Si phase is skin or shell like. Epitaxial Au_3Si phase on gold can be observed.

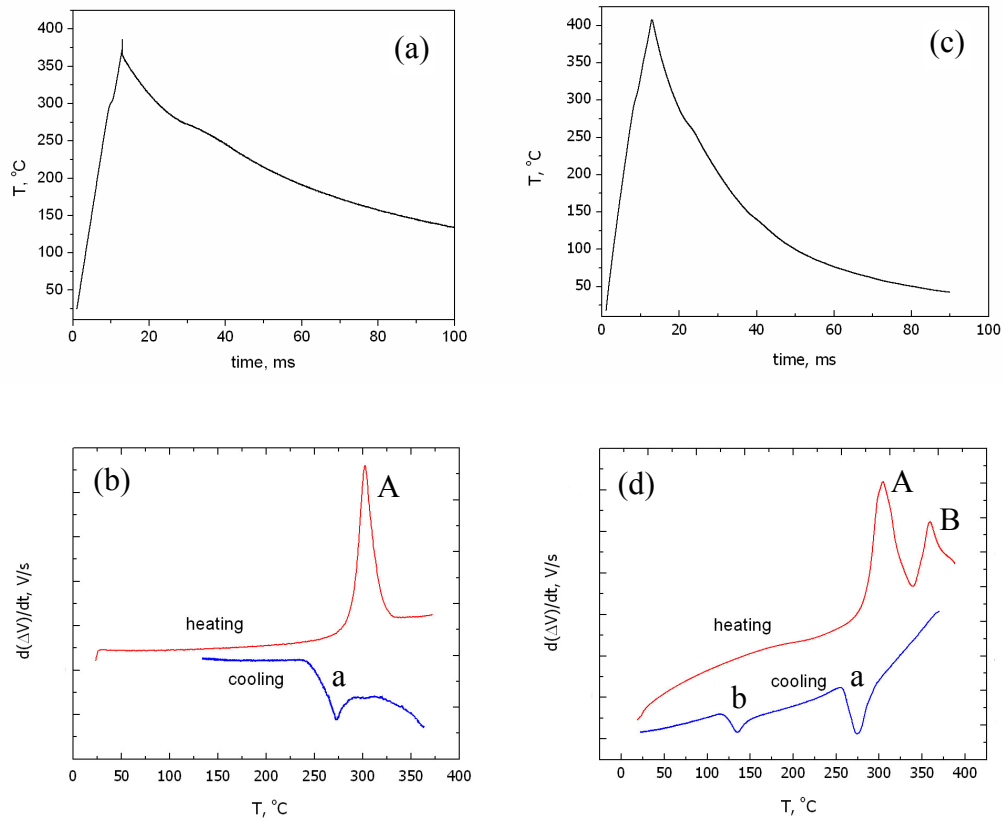


Figure 6-14. Heating and cooling experimental results of the metastable phase (melting peak A) sample and the metastable phase (melting peak A) plus eutectic alloy (melting peak B) sample. As one can see that eutectic alloy has much stronger supercooling than that of metastable phase.

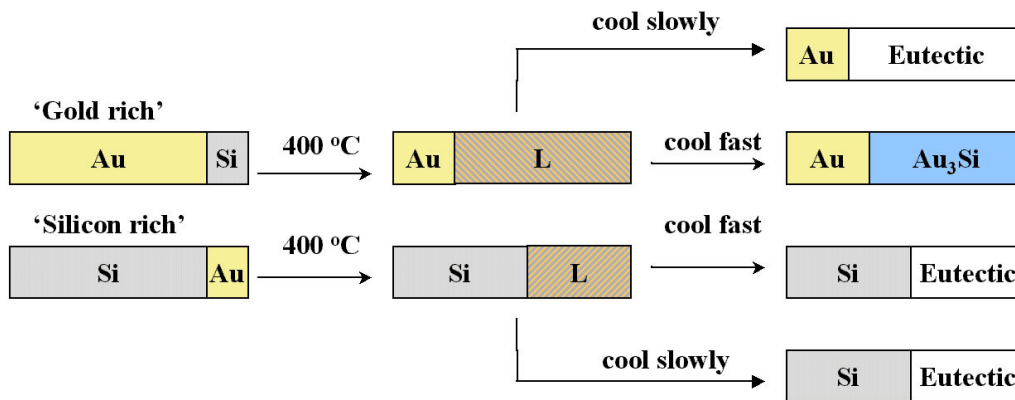


Figure 6-15. Illustrations on the phase formation. Under the experimental conditions (quenching), “gold-rich” samples tend to form Au₃Si phase; “silicon-rich” samples tend to form eutectic. The phenomenon can be explained by the difference in nucleation and growth, or the difference in the liquid. Details can be seen in text.

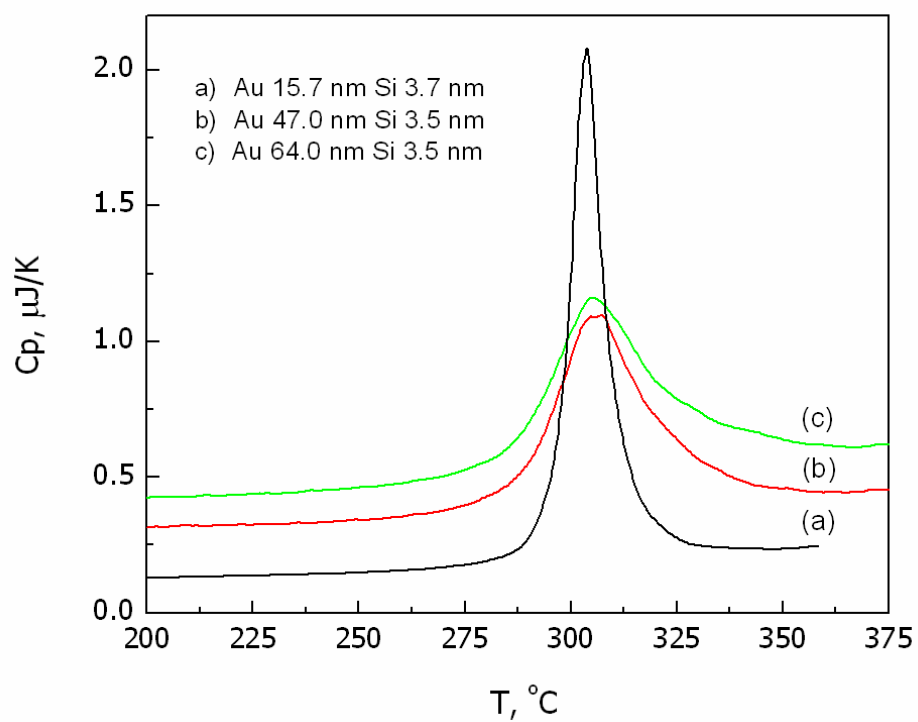


Figure 6-16. The caloric curves with excess gold showing the metastable phase melting peak. The heat of fusion can be calculated by measuring the area under the melting peak. 26.4 kJ/mol (in terms of Au_3Si) is obtained independently.

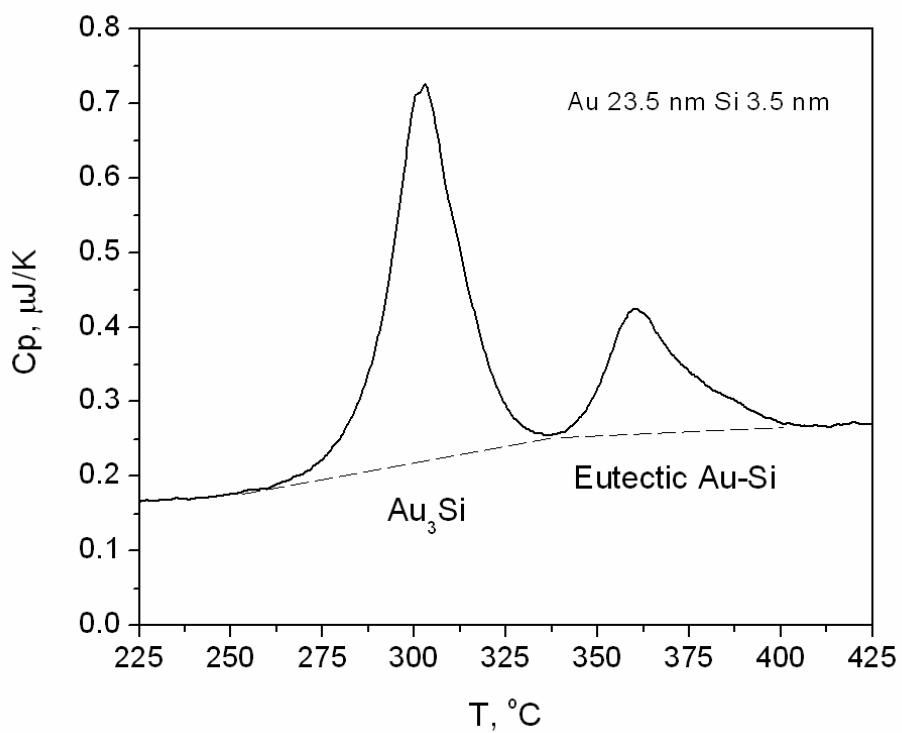


Figure 6-17. The caloric curve showing two melting peaks (metastable phase melting and eutectic alloy melting) can be used to estimate the heat of fusion of the eutectic alloy. The amount of silicon in the metastable phase can be calculated using the result from Figure 6-16.

CHAPTER 7

SUMMARY AND FUTURE WORK

In terms of materials, the work presented in this thesis can be summarized as two parts: thermal behaviors of indium nanoparticles and gold silicide. In terms of the work, it also consists of two parts: to study materials problems (Science) and to develop the nanocalorimetry technique (Engineering).

Engineering solutions are not that straightforward to scientific problems. For example, TEM can obtain lattice images, but it does not mean that accuracy of the nanoparticle size distribution can reach the same level due to the background noise from substrates and characteristics of the sample. Quantitative studies usually involve more experimental details. The experimenters have to understand and to optimize these details in order to obtain clean results.

It is not surprising that researches on nanostructures and thin films can be complex and difficult. My first project at here was to check if we could extract quantitative information from coalescence and ripening (small particles form larger particles releasing surface energy). Finally, I could not separate or eliminate the extraneous signal from molecular desorption ($1\sim 2\times 10^{-8}$ torr, oil system). Therefore, in indium experiment, only the reversible melting transition has been studied where the molecular adsorption/desorption effect is limited by the very short interval between continuous caloric scans (pulse heating). The first several gold silicide experiments were performed in the same system at 10^{-8} torr vacuum level. Up to 7 melting peaks had been

observed, and the results were not very repeatable. The contamination from carbon and oxygen are the sources of the problem. Similarly, the very first experiment in the UHV system was carried out at low 10^{-9} torr range using the Knudsen cell to evaporate silicon but Arsenic impurity was found by Auger analyses which came from the previous user. After the chemical cleaning and redesign the system, simple and reproducible results have been obtained and discussed in Chapter 6.

Nanocalorimetry can be a powerful experimental tool to study very small amount of materials, especially in nanostructures and thin films. However, the designs of the experiment have to consider the nature of the problem. Details of the experimental procedure have to be carefully examined. At this stage, there is no absolute path to follow. The experiments presented in this thesis can be references to the further work.

The resolution and accuracy of the heat capacity have already been good enough for current studies. The future main job is further to improve the data processing method, i.e., to establish the standard criteria for the data analysis, and to introduce robust methods in data processing.

Besides the regular nanocalorimetry, the real-time experiment can be a straightforward method to observe the phase evolution in thin films. The experiment does not need to change the hardware. Therefore it is easily to realize. The application of this method is very promising.

Cooling experiment introduced in this work can be another important application of nanocalorimetry. The measurement only needs small improvement in the electronic hardware, but it allows tracing the quenching process, which could be helpful to explore the physical reasons for the experimental observation.

Annealing experiment and variable rate of cooling can be very useful tools as an extension of the nanocalorimetry measurement. The sample can be annealed and slowly cooled before the nanocalorimetry scans instead of being quenched in each time. Such studies can further combine with in-situ TEM analyses, for example, to study the metastable phase formation and kinetics. However, such type of work probably needs good vacuum and oil free system to avoid residue gas molecule adsorption/desorption.

For experiments that need non-adiabatic conditions, the nanocalorimeter can be further improved to work in different modes. For example, the heat compensated method used in Perkin-Elmer commercial systems. Such experiments can be flexible from atmosphere to vacuum, from slow heating to rapid heating, from slow cooling to fast quenching, etc. It is a connection between the adiabatic nanocalorimetry and traditional measurements. Unfortunately, such experimental setup is still under developing.

Materials studies are such a broad topic that can not be listed in simple sentences. Nanocalorimeter, as an experimental tool, can be powerful in measuring very small energy change in physical or chemical process. However, since it is sensitive, many other effects can also be recorded. Therefore, the experimenters have to be careful. Crosschecks are often of necessary.

VITA

Ming Zhang was born on July 15, 1972 in Beijing, China. He graduated from Tsinghua University, Beijing, China in 1996 with a bachelor degree in Materials Science and Engineering. He received his master degree in 1998 in Material Physics from the same school. In May 1998, Ming Zhang joined University of Illinois at Urbana-Champaign in the Electronic Materials Division of the Department of Materials Science and Engineering. He completed the Ph. D. program in September 2003.

PUBLICATION

1. Zhang, M., Wen, J.G., Efremov, M.Yu., Olson, E.A., Zhang, Z.S., Allen, L. H., *The Properties of the Gold Silicide Metastable Phase by Scanning Nanocalorimetry*. to be submitted, 2003.
2. Zhang, M., Wen, J.G., Efremov, M.Yu., Olson, E.A., Zhang, Z.S., Allen, L. H., *Real-time Observation of the Phase Evolution in Gold Silicon Thin Films*. to be submitted, 2003.
3. Zhang, M., Efremov, M. Y., Olson, E. A., Zhang, S., Allen, L. H., *Real-time heat capacity measurement during thin-film deposition by scanning nanocalorimetry*. Applied Physics Letters, 2002. **81**(20): p. 3801-3803.
4. Zhang, M., Efremov, M. Yu., Schiettekatte, F., Olson, E. A., Kwan, A. T., Lai, S. L., Wisleder, T., Greene, J. E., Allen, L. H., *Size-dependent melting point depression of nanostructures: Nanocalorimetric measurements*. Physical Review B, 2000. **62**(15): p. 10548-10557.
5. Efremov, M.Y., Schiettekatte, F., Zhang, M., Olson, E. A., Kwan, A. T., Berry, R. S., Allen, L. H., *Discrete periodic melting point observations for nanostructure ensembles*. Physical Review Letters, 2000. **85**(17): p. 3560-3563.
6. Efremov, M.Y., Olson, E. A., Zhang, M., Zhang, Lai, S. L., Schiettekatte, F., Z. S., Allen, L. H., *Thin-Film Differential Scanning Nanocalorimetry: Heat Capacity Analysis*. Thermochemica Acta, 2003: p. submitted.

7. Efremov, M.Y., Warren, J. T.,Olson, E. A.,Zhang, M.,Kwan, A. T.,Allen, L. H., *Thin-film differential scanning calorimetry: A new probe for assignment of the glass transition of ultrathin polymer films*. *Macromolecules*, 2002. **35**(5): p. 1481-1483.
8. Efremov, M.Y., Olson, E. A.,Zhang, M.,Allen, L. H., *Glass transition of thin films of poly(2-vinyl pyridine) and poly(methyl methacrylate): nanocalorimetry measurements*. *Thermochimica Acta*, 2003. **403**(1): p. 37-41.
9. Olson, E.A., Efremov, M. Yu., Zhang, M., Zhang, Z. S. Allen, L. H., *The design and operation of a MEMS differential scanning nanocalorimeter for high-speed heat capacity measurements of ultrathin films*. *Journal of Microelectromechanical Systems*, 2003. **12**(3): p. 355-64.
10. Olson, E.A., Efremov, M. Y.,Kwan, A. T.,Lai, S.,Petrova, V.,Schiettekatte, F.,Warren, J. T.,Zhang, M.,Allen, L. H., *Scanning calorimeter for nanoliter-scale liquid samples*. *Applied Physics Letters*, 2000. **77**(17): p. 2671-3.